EUROPEAN ORGANISATION FOR NUCLEAR RESEARCH (CERN)

Submitted to: EPJC

CERN-EP-2017-008
14th March 2017

Measurements of electroweak Wjj production and constraints on anomalous gauge couplings with the ATLAS detector

The ATLAS Collaboration

Measurements of the electroweak production of a W boson in association with two jets at high dijet invariant mass are performed using $\sqrt{s} = 7$ and 8 TeV proton–proton collision data produced by the Large Hadron Collider, corresponding respectively to 4.7 and 20.2 fb^{-1} of integrated luminosity collected by the ATLAS detector. The measurements are sensitive to the production of a W boson via a triple-gauge-boson vertex and include both the fiducial and differential cross sections of the electroweak process.

Contents

1 Introduction

The non-Abelian nature of the Standard Model (SM) electroweak theory predicts the self-interactions of the weak gauge bosons. These triple and quartic gauge-boson couplings provide a unique means to test for new fundamental interactions. The fusion of electroweak (EW) bosons is a particularly important process for measuring particle properties, such as the couplings of the Higgs boson, and for searching for new particles beyond the Standard Model [1–11]. In proton–proton (pp) collisions, a characteristic signature of these processes is the production of two high-momentum jets of hadrons at small angles with respect to the incoming proton beams [12]. Measurements of this vector-boson-fusion (VBF) topology have been performed in W [13], Z [14, 15] and Higgs [16] boson production, though the observation of purely electroweak processes in this topology has only been achieved in individual measurements of Z-boson production. This paper presents a precise measurement of electroweak W-boson production in the VBF topology, with a significance well above the standard for claiming observation, as well as differential cross section measurements and constraints on anomalous triple-gauge-boson couplings (aTGCs).

The production of a W boson in association with two or more jets (Wjj) is dominated by processes involving strong interactions (strong Wjj or QCD Wjj). These processes have been extensively studied by experiments at the Large Hadron Collider (LHC) [17, 18] and the Tevatron collider [19, 20], motivating the development of precise perturbative predictions [21–33]. The large cross section for W-boson production provides greater sensitivity to the VBF topology and to the electroweak production of Wjj (electroweak Wjj or EW Wjj) than corresponding measurements of Z- or Higgs-boson production.

The VBF process is inseparable from other electroweak Wjj processes, so it is not measured directly; sensitivity to the VBF production mechanism is quantified by determining constraints on operator coefficients in an effective Lagrangian approach [34]. The classes of electroweak diagrams constituting the signal are shown in Figure 1 [35] and contain at least three vertices where an electroweak gauge boson connects to a pair of fermions. The background from a W boson associated with strongly produced jets is shown in Figure 2 and has only two electroweak vertices. This background has $O(10)$ times the yield of the signal process, and can interfere with the signal. This interference is suppressed because only a small subset of the background diagrams have the same initial and final state as the signal.

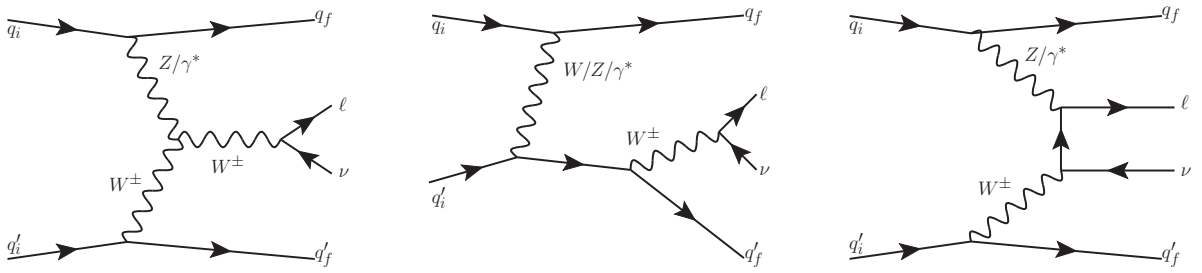

(a) Vector boson fusion (b) W bremsstrahlung (c) Non-resonant

Figure 1: Representative leading-order diagrams for electroweak Wjj production at the LHC. In addition to (a) the vector boson fusion process, there are four (b) W bremsstrahlung diagrams, corresponding to $W^\pm$ boson radiation by any incoming or outgoing quark, and two (c) non-resonant diagrams, corresponding to $W^\pm$ boson radiation by either incoming quark.

The analysis signature consists of a neutrino and either an electron or a muon, two jets with a high dijet invariant mass, and no additional jets at a wide angle from the beam. This signature discriminates signal

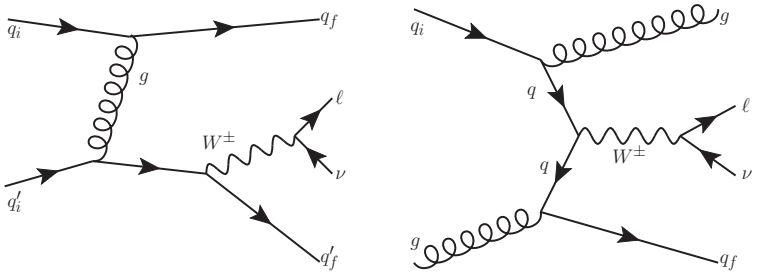

Figure 2: Examples of leading-order diagrams for strong Wjj production at the LHC. The left-hand diagram interferes with the electroweak diagrams of Figure 1 when the final-state quarks have the same colours as the initial-state quarks.

events from the copious background events consisting of strongly produced jets associated with a W (or Z) boson, top-quark production, or multijet production. The purity of electroweak Wjj production increases with increasing dijet invariant mass, increasing the sensitivity to anomalous triple-gauge-boson couplings.

Measurements of the inclusive and fiducial cross sections of electroweak Wjj production in proton–proton collisions at centre-of-mass energies $\sqrt{s} = 7$ and 8 TeV are performed in a fiducial region with a signal-to-background ratio of approximately 1:8. The electroweak signal is extracted with a binned likelihood fit to the dijet invariant mass distribution. The fit determines the ratio μ_{EW} of the measured signal cross section to that of a Standard Model calculation [36]; this ratio is then multiplied by the prediction to provide the measured cross section. To reduce the uncertainties in the modelling of the strong Wjj events, data are used to constrain their dijet mass distribution, resulting in a precise measurement of the electroweak Wjj fiducial cross section. The quantum-mechanical interference between electroweak and strong Wjj processes is not modelled and its impact on the measurement is estimated using a Monte Carlo simulation and taken as an uncertainty.

In order to explore the kinematics of the Wjj topology, and the interplay between strong and electroweak production, the 8 TeV data are unfolded differentially to particle level in many variables and phase-space regions, and compared to theoretical predictions. Electroweak Wjj production is measured in regions where the signal purity is relatively high ($\gtrsim 10\%$); combined strong and electroweak Wjj production is measured in the other regions. These measurements are then integrated to obtain fiducial cross sections in the different phase-space regions, albeit with larger uncertainties than the measurement with the constrained background.

Sensitivity to the VBF diagram is determined by modifying the triple-gauge-boson couplings. Anomalous couplings arising from new processes at a high energy scale would cause increasing deviations from the SM prediction for increasing momentum transfer between the incoming partons. Hence, a region of high momentum transfer is defined, and constraints on anomalous gauge couplings are set in the context of an effective field theory (EFT), including limits on interactions that violate charge-parity (CP) conservation.

The paper is organized as follows. The ATLAS detector and reconstruction of the final-state particles are described in Section 2. The definitions of the measurement phase-space regions and the event selection are given in Section 3. The modelling of signal and background processes is discussed in Section 4. Section 5 is dedicated to the precise extraction of the inclusive and fiducial cross sections, while Section 6 presents differential cross sections unfolded for detector effects. Section 7 describes limits on aTGCs and

parameters of an effective field theory. Section 8 summarizes the results and the Appendix provides a comprehensive set of differential cross-section measurements.

2 ATLAS detector and data reconstruction

The data set corresponds to LHC pp collisions at $\sqrt{s} = 7$ TeV in 2011 and at $\sqrt{s} = 8$ TeV in 2012, with final-state particles measured by the ATLAS detector. This section describes the detector and the reconstruction of the data to produce the final-state physics objects used in the measurements.

2.1 ATLAS detector

ATLAS is a multi-purpose detector used to measure LHC particle collisions. A detailed description of the detector can be found in Ref. [37]. A tracking system comprises the inner detector (ID) surrounding the collision point, with silicon pixel and microstrip detectors most centrally located, followed by a transition radiation tracker at higher radii [38, 39]. These tracking detectors are used to measure the trajectories and momenta of charged particles up to pseudorapidities of $|\eta| = 2.5$.[1] The ID is surrounded by a superconducting solenoid, providing a 2 T magnetic field for the tracking detectors.

A calorimeter system surrounds the solenoid magnet and consists of electromagnetic and hadronic sections. The electromagnetic section is segmented along the z-axis into a barrel region covering $|\eta| < 1.475$, two end-cap components spanning $1.375 < |\eta| < 3.2$, and two forward components ($3.1 < |\eta| < 4.9$). Similarly, the hadronic section comprises a barrel region ($|\eta| < 1.7$), two end-cap regions ($1.5 < |\eta| < 3.2$), and two forward regions ($3.1 < |\eta| < 4.9$). The barrel region of the hadronic section uses scintillator tiles as the active medium, while the remaining regions use liquid argon.

A muon spectrometer surrounds the calorimeter system and contains superconducting coils, drift tubes and cathode strip chambers to provide precise measurements of muon momenta within $|\eta| < 2.7$. The spectrometer also includes resistive-plate and thin-gap chambers to trigger on muons in the region $|\eta| < 2.4$.

The ATLAS trigger system uses three consecutive stages to select events for permanent storage. The first level uses custom electronics and the second level uses fast software algorithms to inspect regions of interest flagged by the first trigger level. At the third level, the full event is reconstructed using software algorithms similar to those used offline.

[1] ATLAS uses a right-handed coordinate system with its origin at the nominal interaction point in the centre of the detector and the z-axis along the beam pipe. The x-axis points from the interaction point to the centre of the LHC ring, and the y-axis points upward. Cylindrical coordinates (r, ϕ) are used in the transverse plane, ϕ being the azimuthal angle around the z-axis. The pseudorapidity is defined in terms of the polar angle θ as $\eta = -\ln\tan(\theta/2)$. The rapidity is defined as $y = 0.5\ln[(E + p_z)/(E - p_z)]$, where E and p_z are the energy and longitudinal momentum, respectively. Momentum in the transverse plane is denoted by p_{T}.

2.2 Object reconstruction

Electrons, muons, and jets of particles resulting from quark or gluon production are reconstructed in the ATLAS detector. Each type of object has a distinctive signature and is identified using the criteria described below. The object identification includes track and vertex positions relative to the primary event vertex, defined as the reconstructed vertex with the highest summed p_{T}^2 of all associated tracks. Each object is calibrated and modelled in Monte Carlo simulation, corrected to match data measurements of the trigger, reconstruction, and identification efficiencies, and of the energy and momentum scales and resolutions [40–44].

Electrons

Electron candidates are reconstructed from energy clusters in the electromagnetic section of the calorimeter which are matched to tracks reconstructed in the ID. Candidates for signal events are required to satisfy 'tight' selection criteria [41, 42], which include requirements on calorimeter shower shape, track hit multiplicity, the ratio of reconstructed energy to track momentum, E/p, and the matching of the energy clusters to the track. In order to build templates to model the multijet background (see Section 4.2), a set of criteria is employed based on 'loose' or 'medium' selection, which drops the E/p requirement and uses less restrictive selection criteria for the other discriminating variables.

Electron candidates are required to be isolated to reject possible misidentified jets or heavy-flavour hadron decays. Isolation is calculated as the ratio of energy in an isolation cone around the primary track or calorimeter deposit to the energy of the candidate. Different isolation requirements are made in the 7 TeV and 8 TeV data sets, due to the different LHC and detector operating conditions. For 7 TeV data taking, the requirements on track and calorimeter isolation variables associated with the electron candidate achieve a constant identification efficiency as a function of the candidate transverse energy (E_{T}) and pseudorapidity. The 8 TeV trigger includes a requirement on track isolation, so the selection is more restrictive and requires the summed p_{T} of surrounding tracks to be $< 5\%$ of the electron candidate E_{T}, excluding the electron track and using a cone of size $R \equiv \sqrt{(\Delta\phi)^2 + (\Delta\eta)^2} = 0.2$ around the shower centroid.

Muons

Muon candidates are identified as reconstructed tracks in the muon spectrometer which are matched to and statistically combined with ID tracks to form a 'combined' muon candidate [43]. Quality requirements on the ID track include a minimum number of hits in each subdetector to ensure good track reconstruction. Candidates in 7 TeV data are selected using a track-based fractional isolation requiring the scalar sum of the p_{T} values of tracks within a cone of size $R = 0.2$ of the muon track to be less than 10% of the candidate p_{T}. For 8 TeV data taking, requirements are applied to track and calorimeter fractional isolation using a cone of size $R = 0.3$. The upper bound on each type of isolation increases with increasing muon p_{T}, and is 15% for $p_{\mathrm{T}} > 30$ GeV.

Additional transverse (d_0) and longitudinal (z_0) impact parameter requirements of $|d_0/\sigma_{d_0}| < 3$ (where σ_{d_0} is the d_0 uncertainty) and $|z_0 \sin\theta| < 0.5$ mm are imposed on all muon and electron candidates to suppress contributions from hadron decays to leptons.

Jets

Jets are reconstructed using the anti-k_t algorithm [45] with a jet-radius parameter of 0.4, from three-dimensional clustered energy deposits in the calorimeters [46]. Jets are required to have $p_{\mathrm{T}} > 30$ GeV and $|\eta| < 4.4$, and must be separated from the lepton in η–ϕ space, $\Delta R(\ell, j) \geq 0.3$. Quality requirements

are imposed to remove events where jets are associated with noisy calorimeter cells. Jet energies are corrected for the presence of low-energy contributions from additional in-time or out-of-time collisions (pile-up), the non-compensating response of the calorimeter, detector material variations, and energy losses in uninstrumented regions. This calibration is performed in bins of p_{T} and η, using correction factors determined using a combination of Monte Carlo simulations and in-situ calibrations with data [44, 47]. The systematic uncertainties in these correction factors are determined from the same control samples in data. A significant source of uncertainty in this analysis arises from the modelling of the η dependence of the jet energy response.

To suppress the contribution of jets from additional coincident pp collisions, the jet vertex fraction (JVF) [48] is used to reject central jets ($|\eta| < 2.4$) that are not compatible with originating from the primary vertex. The JVF is defined as the scalar sum of the p_{T} values of tracks associated with both the primary vertex and the jet, divided by the summed p_{T} of all tracks associated with the jet. For the 7 TeV data taking, the requirement is $|\mathrm{JVF}| \geq 0.75$; this requirement is loosened in 8 TeV data taking to $|\mathrm{JVF}| \geq 0.5$ if the jet has $p_{\mathrm{T}} < 50$ GeV. The relaxed requirement in 8 TeV data is due to the larger pile-up rate causing signal events to be rejected when using the 7 TeV selection, and the requirement of $|\eta| < 2.4$ is to ensure the jets are within the ID tracking acceptance.

Jets that are consistent with originating from heavy-flavour quarks are identified using a neural network algorithm trained on input variables related to the impact parameter significance of tracks in the jet and the secondary vertices reconstructed from these tracks [49]. Jets are identified as b-jets with a selection on the output of the neural network corresponding to an identification efficiency of 80%.

Missing transverse momentum

In events with a leptonically decaying W boson, one expects large missing momentum in the transverse plane due to the escaping neutrino. The magnitude of this missing transverse momentum ($E_{\mathrm{T}}^{\mathrm{miss}}$) is constructed from the vector sum of muon momenta and three-dimensional energy clusters in the calorimeter [50, 51]. The clusters are corrected to account for the different response to hadrons compared to electrons or photons, as well as dead material and out-of-cluster energy losses. Additional tracking information is used to extrapolate low-momentum particles to the primary vertex to reduce the contribution from pile-up.

3 Event selection

The proton–proton collision data samples correspond to a total integrated luminosity of 4.7 fb^{-1} for the 7 TeV data and 20.2 fb^{-1} for the 8 TeV data with uncertainties of 1.8% [52] and 1.9% [53], respectively.

The measurements use data collected with single-electron and single-muon triggers. The triggers identify candidate muons by combining an ID track with a muon-spectrometer track, and candidate electrons by matching an inner detector track to an energy cluster in the calorimeter consistent with an electromagnetic shower. The triggers in the 7 TeV data require $p_{\mathrm{T}} > 18$ GeV for muons and either $E_{\mathrm{T}} > 20$ GeV or $E_{\mathrm{T}} > 22$ GeV for electrons, depending on the data-taking period. The 8 TeV data events are selected by two triggers in each channel. The electron-channel triggers have E_{T} thresholds of 24 GeV and 60 GeV, where the lower-threshold trigger includes a calorimeter isolation criterion: the measured E_{T} within a cone of radius $R = 0.2$ around the electron candidate, excluding the electron candidate's E_{T}, must be less than 10% of the E_{T} of the electron. The muon-channel triggers have p_{T} thresholds of 24 GeV and 36 GeV. The lower-threshold trigger has a track-isolation requirement, where the scalar summed p_{T} of

Table 1: Phase-space definitions at the generated particle level. Each phase-space region includes the preselection and the additional requirements listed for that region. The variables are defined in Sections 3.1 and 3.2.

Region name	Requirements
Preselection	Lepton $p_{\mathrm{T}} > 25$ GeV Lepton $\lvert\eta\rvert < 2.5$ $E_{\mathrm{T}}^{\mathrm{miss}} > 20$ GeV $m_{\mathrm{T}} > 40$ GeV $p_{\mathrm{T}}^{j_1} > 80$ GeV $p_{\mathrm{T}}^{j_2} > 60$ GeV Jet $\lvert y\rvert < 4.4$ $M_{jj} > 500$ GeV $\Delta y(j_1, j_2) > 2$ $\Delta R(j, \ell) > 0.3$
Fiducial and differential measurements	
Signal region	$N_{\mathrm{lepton}}^{\mathrm{cen}} = 1, N_{\mathrm{jets}}^{\mathrm{cen}} = 0$
Forward-lepton control region	$N_{\mathrm{lepton}}^{\mathrm{cen}} = 0, N_{\mathrm{jets}}^{\mathrm{cen}} = 0$
Central-jet validation region	$N_{\mathrm{lepton}}^{\mathrm{cen}} = 1, N_{\mathrm{jets}}^{\mathrm{cen}} \geq 1$
Differential measurements only	
Inclusive regions	$M_{jj} > 0.5$ TeV, 1 TeV, 1.5 TeV, or 2 TeV
Forward-lepton/central-jet region	$N_{\mathrm{lepton}}^{\mathrm{cen}} = 0, N_{\mathrm{jets}}^{\mathrm{cen}} \geq 1$
High-mass signal region	$M_{jj} > 1$ TeV, $N_{\mathrm{lepton}}^{\mathrm{cen}} = 1, N_{\mathrm{jets}}^{\mathrm{cen}} = 0$
Anomalous coupling measurements only	
High-q^2 region	$M_{jj} > 1$ TeV, $N_{\mathrm{lepton}}^{\mathrm{cen}} = 1, N_{\mathrm{jets}}^{\mathrm{cen}} = 0$, $p_{\mathrm{T}}^{j_1} > 600$ GeV

tracks within a cone of radius $R = 0.2$ around the muon is required to be less than 12% of the p_{T} of the muon.

The analysis defines many measurement regions varying in electroweak Wjj purity. Table 1 shows the regions at the generated particle level based on the variables defined below. Particle-level objects are reconstructed as follows: jets are reconstructed using the anti-k_t algorithm with a radius parameter of 0.4 using final-state particles with a proper lifetime longer than 10 ps; and leptons are reconstructed by combining the final-state lepton with photons within a cone of $R = 0.1$ around the lepton. The requirements in Table 1 are also used to select data events, except for the following differences: (1) electrons must have $\lvert\eta\rvert < 2.47$ cannot be in the crack region of the calorimeter ($1.37 < \lvert\eta\rvert < 1.52$); (2) muons must have $\lvert\eta\rvert < 2.4$; and (3) jets are selected using pseudorapidity ($\lvert\eta\rvert < 4.4$) rather than rapidity. Also, a b-jet veto is applied to the validation region in data when performing the measurement of the fiducial electroweak Wjj cross section described in Section 5.

3.1 Event preselection

Signal candidate events are initially defined by the presence of missing transverse momentum ($E_{\mathrm{T}}^{\mathrm{miss}} >$ 20 GeV), exactly one charged lepton (electron or muon) candidate with $p_{\mathrm{T}} > 25$ GeV, and at least two

jets. The highest-p_{T} jet is required to have $p_{\mathrm{T}}^{j_1} > 80$ GeV and the second jet must have $p_{\mathrm{T}}^{j_2} > 60$ GeV. To isolate events with a W boson, a veto is imposed on events with a second same-flavour lepton with $p_{\mathrm{T}} > 20$ GeV; these leptons are identified in data using relaxed isolation and impact parameter criteria. A minimum cut on the transverse mass, $m_{\mathrm{T}} > 40$ GeV, of the W-boson candidate is additionally imposed, where m_{T} is defined by:

$$m_{\mathrm{T}} = \sqrt{2p_{\mathrm{T}} \cdot E_{\mathrm{T}}^{\mathrm{miss}} \left[1 - \cos \Delta\phi(\ell, E_{\mathrm{T}}^{\mathrm{miss}})\right]}.$$

Jets are selected in data if they have $|\eta| < 4.4$ and $\Delta R(j, \ell) > 0.3$. A VBF topology is selected by requiring the invariant mass of the dijet system defined by the two highest-p_{T} jets to satisfy $M_{jj} > 500$ GeV, and the absolute value of the rapidity separation of the jets to satisfy $\Delta y(j_1, j_2) > 2$.

3.2 Definitions of the measurement regions

The above preselection defines an *inclusive* fiducial region, which is then split into four orthogonal fiducial regions defined by the presence or absence of the lepton or an additional jet in a "central" rapidity range between the two highest-p_{T} jets. The signal EW Wjj process is characterized by a lepton and no jets in the central rapidity range. This range is determined by the centrality variable C_ℓ or C_j for the lepton or jets respectively:

$$C_{\ell\ (j)} \equiv \left| \frac{y_{\ell\ (j)} - \frac{y_1 + y_2}{2}}{y_1 - y_2} \right|, \tag{1}$$

where $y_{\ell\ (j)}$ is the rapidity of the candidate lepton (jet), and y_1 and y_2 are the rapidities of the highest-p_{T} (leading) and next-highest-p_{T} (subleading) jets. Requiring the centrality to be below a value C_{max} defines the selection of a rapidity range centred on the mean rapidity of the leading jets, i.e.,

$$\left[\frac{y_1 + y_2}{2} - C_{\mathrm{max}} \times (y_1 - y_2), \quad \frac{y_1 + y_2}{2} + C_{\mathrm{max}} \times (y_1 - y_2) \right], \tag{2}$$

as illustrated in Figure 3. For $C_{\mathrm{max}} = 0.5$, the interval spans the entire rapidity region between the two jets; the number of jets within this interval is denoted $N_{\mathrm{jets}}^{\mathrm{gap}}$. In defining the electroweak Wjj signal region, $C_{\mathrm{max}} = 0.4$ is used to count the number of leptons ($N_{\mathrm{lepton}}^{\mathrm{cen}}$) or jets ($N_{\mathrm{jets}}^{\mathrm{cen}}$) within the range. A value of $C_{\mathrm{max}} = 0.4$ permits an event with the emission of an additional jet close to one of the two highest-p_{T} jets to be retained as a candidate signal event.

The fiducial regions are illustrated in Figure 4. The signal process is characterized by a W boson in the rapidity range spanned by the two jets (Figure 1), with no jets in this range due to the absence of colour flow between the interacting partons. An event is therefore defined as being in the electroweak-enhanced *signal* region if the identified lepton is reconstructed in the rapidity region defined by Eq. (2) and no additional jets are reconstructed in this interval. A QCD-enhanced *forward-lepton control* fiducial region is defined by the requirement that neither the identified lepton nor any additional jets be present in the central rapidity interval. A second QCD-enhanced *central-jet validation* region is defined by events having both the identified lepton and at least one additional jet reconstructed in the central rapidity interval. These three orthogonal fiducial regions are used in Section 5 to constrain the modelling of QCD Wjj production from data, extract the EW Wjj production cross section, and validate the QCD Wjj modelling, respectively.

For the determination of unfolded differential cross sections presented in Section 6, four additional fiducial regions are studied: the inclusive region for the progressively more restrictive dijet invariant mass

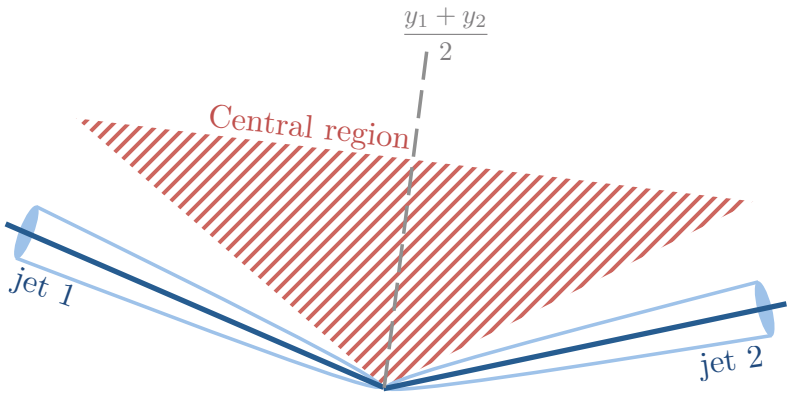

Figure 3: Illustration of the central region used to count leptons and jets in the definition of the signal, control, and validation regions. The rapidity range of the region corresponds to $C_{\text{max}} = 0.4$ in Eq. (2). An object in the direction of the dashed line has $C = 0$.

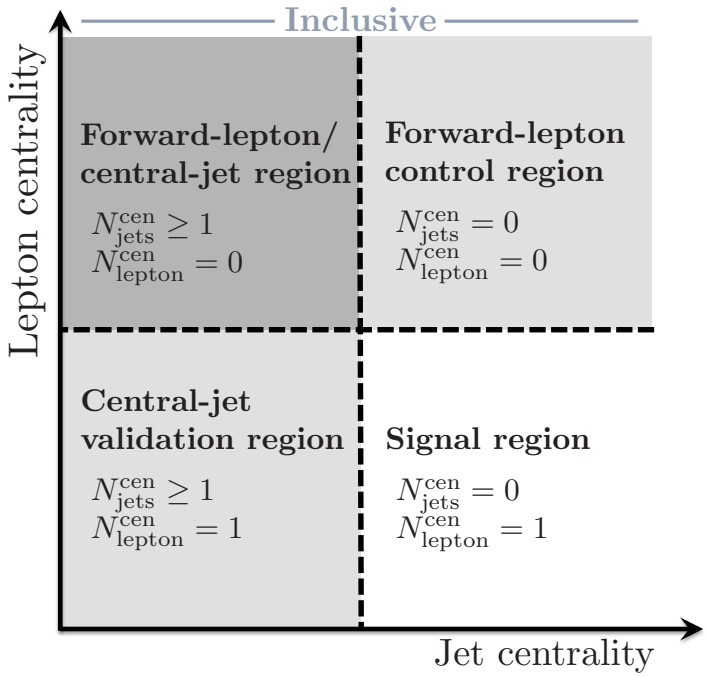

Figure 4: Illustration of the relationship between the signal, control, and validation fiducial regions. The signal region is defined by both a veto on additional jets (beyond the two highest-p_{T} jets) and the presence of a lepton in the rapidity region defined in Eq. (2). The signal region is studied with either $M_{jj} > 0.5$ TeV or 1 TeV. A forward-lepton/central-jet fiducial region is also defined, for which the centrality requirements on the jets and the lepton are inverted with respect to the signal region. The inclusive region corresponds to the union of all four regions, and is studied with $M_{jj} > 0.5,\ 1.0,\ 1.5$, or 2.0 TeV. The quantities $N^{\text{cen}}_{\text{jets}}$ and $N^{\text{cen}}_{\text{lepton}}$ refer to the number of reconstructed leptons and additional jets reconstructed in the rapidity interval defined by Eq. (2) and illustrated in Figure 3, with $C_{\text{max}} = 0.4$.

thresholds of 1.0 TeV, 1.5 TeV, and 2.0 TeV, and an orthogonal *forward-lepton/central-jet* region defined by events with the lepton outside the central region, but at least one additional jet reconstructed in the interval. For the study of EW Wjj differential cross sections (Section 6.4), the signal fiducial region with an increased dijet invariant mass requirement of $M_{jj} > 1$ TeV (*high-mass signal region*) is also analyzed; a further requirement that the leading-jet p_{T} be greater than 600 GeV defines a t-channel *high-q^2* region used for constraints on aTGCs (discussed in Section 7).

4 Modelling of signal and background processes

Simulated Monte Carlo (MC) samples are used to model Wjj production, with small data-derived corrections applied to reduce systematic uncertainties. Other processes producing a prompt charged lepton are also modelled with MC samples. The multijet background, where a photon or hadronic jet is misreconstructed as a prompt lepton, or where a lepton is produced in a hadron decay, is modelled using data.

4.1 Monte Carlo simulation

The measurements described in this paper focus on the electroweak production of Wjj. This process is distinguishable from strong Wjj production, but there can be interference between the processes. The other significant background processes are top-quark, Z-boson, and diboson production, which are modelled with MC simulation. All MC samples used to model the data are passed through a detector simulation [54] based on GEANT4 [55]. Pile-up interactions are modelled with PYTHIA8 (v. 8.165) [56]. Table 2 lists the MC samples and the cross sections used in the MC normalization.

Wjj

The primary model of the signal and background Wjj processes in the analysis is the next-to-leading-order (NLO) POWHEG Monte Carlo generator [29, 36, 57, 58], interfaced with PYTHIA8 using the AU2 parameter values [59] for the simulation of parton showering, underlying event, and hadronization. Two final-state partons with $p_{\mathrm{T}} > 20$ GeV are required for the signal. A generator-level suppression is applied in the background generation to enhance events with one parton with $p_{\mathrm{T}} > 80$ GeV and a second parton with $p_{\mathrm{T}} > 60$ GeV, and the mass of the pair larger than 500 GeV. Parton momentum distributions are modelled using the CT10 [60] set of parton distribution functions (PDFs). The QCD factorization and renormalization scales are set to the W-boson mass for the sample with jets produced via the electroweak interaction. For the sample with strongly produced jets, the hard-process scale is also the W-boson mass while the QCD emission scales are set with the multiscale-improved NLO (MiNLO) procedure [61] to improve the modelling and reduce the scale dependence. Uncertainties due to missing higher-order contributions are estimated by doubling and halving the factorization and renormalization scales independently, but keeping their ratio within the range 0.5–2.0. Uncertainties due to parton distribution functions are estimated using CT10 eigenvector variations rescaled to 68% confidence level, and an uncertainty due to the parton shower and hadronization model is taken from the difference between predictions using the PYTHIA8 and HERWIG++ [62, 63] generators.

Measured particle-level differential distributions are also compared to the SHERPA (v. 1.4) [64] generation of QCD+EW Wjj production at leading-order accuracy, including interference. An uncertainty due to the neglect of interference in the EW Wjj measurement is estimated using this sample and individual SHERPA

Table 2: Monte Carlo samples used to model the signal and background processes. The cross sections times branching fractions, $\sigma \cdot \mathcal{B}$, are quoted for $\sqrt{s}$ = 7 and 8 TeV. The branching fraction corresponds to the decay to a single lepton flavour, and here ℓ refers to e, μ, or τ. The neutral current Z/γ^* process is denoted by Z. To remove overlap between $W(\to \tau\nu)$ + 2 jets and WW/WZ in 7 TeV samples, events with a generated τ lepton are removed from the 7 TeV WW/WZ samples. Jets refer to a quark or gluon in the final state of the matrix-element calculation.

Process	MC generator	$\sigma \cdot \mathcal{B}$ [pb]	
		7 TeV	8 TeV
$W(\to e\nu, \mu\nu)$ + 2 jets			
2 EW vertices	Powheg + Pythia8	4670	5340
4 EW vertices (no dibosons)	Powheg + Pythia8	2.7	3.4
$W(\to \tau\nu)$ inclusive			
2 EW vertices	Sherpa	10100	11900
$W(\to \tau\nu)$ + 2 jets			
4 EW vertices (with dibosons)	Sherpa	8.4	
4 EW vertices (no dibosons)	Sherpa		4.2
Top quarks			
$t\bar{t}(\to \ell\nu b\bar{q}q\bar{b}, \ell\nu b\ell\nu\bar{b})$	mc@nlo + Herwig	90.0	
	Powheg + Pythia6		114
tW	AcerMC + Pythia6	15.3	
	mc@nlo + Herwig		20.7
$t\bar{b}q \to \ell\nu b\bar{b}q$	AcerMC + Pythia6	23.5	25.8
$t\bar{b} \to \ell\nu b\bar{b}$	AcerMC + Pythia6	1.0	
	mc@nlo + Herwig		1.7
$Z(\to \ell\ell)$ inclusive, $m_{\ell\ell} > 40$ GeV			
2 EW vertices	Sherpa	3140	3620
$Z(\to ee, \mu\mu)$ + 2 jets, $m_{ee,\mu\mu} > 40$ GeV			
4 EW vertices (no dibosons)	Sherpa	0.7	0.9
Dibosons			
WW	Herwig++	45.9	56.8
WZ	Herwig++	18.4	22.5
ZZ	Herwig++	6.0	7.2

QCD and EW Wjj samples. The individual samples are also used to model the small contribution from $W \to \tau\nu$ decays. Measured distributions of QCD+EW Wjj production are compared to the combined QCD+EW and to the QCD Wjj samples, the latter to demonstrate the effect of the EW Wjj process. The QCD Wjj sample is a W + (n)-parton prediction with $n \leq 4$ partons with $p_{\mathrm{T}} > 15$ GeV produced via QCD interactions. The EW Wjj sample has two partons produced via electroweak vertices, and up

to one additional parton produced by QCD interactions. The CKKW matching scheme [65] is used to remove the overlap between different parton multiplicities at the matrix-element level. The predictions use the CT10 PDFs and the default parameter values for simulating the underlying event. Renormalization and factorization scales are set using the standard dynamical scale scheme in SHERPA. The interference uncertainty is cross-checked with the MADGRAPH [28] generator interfaced to PYTHIA8.

For unfolded distributions with a low purity of electroweak Wjj production, an additional comparison is made to the all-order resummation calculation of HEJ (High Energy Jets) [33] for strong Wjj production. The calculation improves the accuracy of predictions in wide-angle or high-invariant-mass dijet configurations, where logarithmic corrections are significant. To allow a comparison to unfolded data and to other generators, the small electroweak Wjj contribution is added using POWHEG interfaced to PYTHIA8 and the sum is labelled HEJ (QCD) + POW+PY (EW).

Both the POWHEG and SHERPA predictions for electroweak Wjj production omit the small contribution from diboson production processes, assuming negligible interference with these processes. Higher-order electroweak corrections to the background Wjj process are studied with OpenLoops [66, 67] and found to affect the measured fiducial cross section by $< 1\%$.

Other processes

Background contributions from top-quark, Z + 2 jets, and diboson processes are estimated using MC simulation.

The top-quark background consists of pair-production and single-production processes, with the latter including s-channel production and production in association with a b quark or W boson. Top-quark pair production is normalized using the cross section calculated at next-to-next-to-leading order (NNLO) in α_S, with resummation to next-to-next-to-leading logarithm (NNLL) using TOP++2.0 [68]. Kinematic distributions are modelled at NLO using the MC@NLO [69] generator and the HERWIG [63, 70] parton shower model for 7 TeV data, and with POWHEG and PYTHIA6 (v. 6.427) [71] for 8 TeV data; both use the CT10 PDF set. An uncertainty due to the parton shower model, and its interface to the matrix-element generator, is estimated by comparing the POWHEG sample to an MC@NLO sample interfaced to HERWIG. Single-top-quark production in the t-channel, $t\bar{b}q \to \ell\nu b\bar{b}q$, is modelled using the leading-order generator ACERMC (v. 3.8) [72] interfaced with PYTHIA6 and the CTEQ6L1 [73] PDF set, and the sample is normalized using the cross sections calculated by the generator. Modelling of the s-channel production of a single top quark, $t\bar{b} \to \ell\nu b\bar{b}$, and of the associated production of a top quark and a W boson are performed using ACERMC with PYTHIA6 in 7 TeV data and MC@NLO with HERWIG in 8 TeV data. These samples are also normalized using the generator cross-section values.

Background from the Z + 2 jets (Zjj) process, which contributes when one of the leptons is not reconstructed and the $E_{\mathrm{T}}^{\mathrm{miss}}$ is large, is modelled using SHERPA and the CT10 PDF set. For the background with jets from QCD radiation, an inclusive Drell–Yan sample is produced at NLO [74] and merged with the leading-order (LO) production of additional partons (up to five). The background with jets produced purely through the electroweak interaction is modelled at leading order. This combination of samples is also used to model the $W(\to \tau\nu)$ + 2 jets background; the 7 TeV sample includes WW and WZ production. The interference between the electroweak and QCD production of jets for these small backgrounds has a negligible impact on the measurements and is not modelled.

The diboson background processes $WW/WZ \to \ell\nu q\bar{q}^{(\prime)}$ and $ZZ \to \ell\ell q\bar{q}$ provide only a small contribution at high dijet mass since the distribution peaks at the mass of the W or Z boson. The interference between the single and pair production of electroweak bosons is negligible for the mass range selected by the

analysis. The diboson processes are modelled at leading order with Herwig++ and normalized to the NLO cross section [75]. The generation uses the CTEQ6L1 PDF set. In 7 TeV samples, $W \to \tau\nu$ decays are removed since they are included in the Wjj samples.

4.2 Multijet background

Multijet production constitutes a background to the Wjj process when one of the jets is misidentified as a lepton and significant $E_{\mathrm{T}}^{\mathrm{miss}}$ arises from either a momentum mismeasurement or the loss of particles outside the detector acceptance. Due to the very small fraction of multijet events with both of these properties, and their relatively poor modelling in simulation, a purely data-driven method is used to estimate this background. The method inverts certain lepton identification criteria (described below) to obtain a multijet-dominated sample for modelling kinematic distributions. The $E_{\mathrm{T}}^{\mathrm{miss}}$ distribution is then fit to obtain a multijet normalization factor; this fit is performed separately in the signal, control, and validation regions. Systematic uncertainties are estimated by modifying the fit distribution and the identification criteria, and by propagating detector and theoretical uncertainties.

Modifications to the lepton identification criteria which enhance the multijet contribution are based on isolation and either the impact parameter with respect to the primary vertex (for muons) or the shower and track properties (for electrons). For the 7 TeV analysis, the impact parameter significance requirement is inverted in the muon channel ($|d_0|/\sigma_{d_0} > 3$). This preferentially selects muons from heavy-flavour hadron decays, a dominant source of muons in multijet events. For the 8 TeV analysis, no requirement on impact parameter significance is made and instead a track isolation requirement is applied orthogonal to the requirement for selected muons ($0.15 < \sum p_{\mathrm{T}}^{R=0.3}/p_{\mathrm{T}} < 0.35$).

For the electron channel in $\sqrt{s} = 7$ TeV data, triggers requiring a loose electron candidate are used to obtain a multijet modelling sample. The electron candidate must satisfy medium criteria on track hit multiplicity and track–shower matching in η, but must fail to satisfy at least one of the tight shower-based criteria. It also must not be isolated in the calorimeter: $\sum E_{\mathrm{T}}^{R=0.3}/E_{\mathrm{T}} > 0.2$. In $\sqrt{s} = 8$ TeV data, electron candidates must satisfy medium selection criteria consistent with the trigger used in the analysis. As in the muon channel, a track isolation window is applied orthogonal to the requirement for selected electrons ($0.05 < \sum p_{\mathrm{T}}^{R=0.2}/p_{\mathrm{T}} < 0.1$).

To normalize the multijet-dominated samples to the expected contribution with nominal lepton criteria, a template fit to the $E_{\mathrm{T}}^{\mathrm{miss}}$ distribution is performed. The fit simultaneously determines the multijet and strong Wjj normalizations in the region where the nominal lepton criteria are applied. Other contributions are fixed to their SM predictions, and the data are consistent with the post-fit distribution within uncertainties. The strong Wjj normalization is consistent with that found in the fit to the dijet mass distribution described in Section 5.

Systematic uncertainties in the multijet normalization arise from uncertainties in the kinematic modelling and in jet, lepton, and $E_{\mathrm{T}}^{\mathrm{miss}}$ reconstruction. The modelling uncertainties dominate and are estimated using three methods: (1) modifying the lepton candidate selection for the kinematic distributions; (2) using m_{T} as an alternative fit distribution; and (3) varying the kinematic range of the fit. For each method, the largest change in the normalization is taken as a systematic uncertainty and added in quadrature with reconstruction and modelling uncertainties for processes modelled with Monte Carlo simulation. The leading uncertainty arises from the change in multijet normalization when fitting the m_{T} distribution instead of the $E_{\mathrm{T}}^{\mathrm{miss}}$ distribution. The next largest uncertainty results from variations of the isolation and impact parameter requirements in the lepton selection used for the kinematic distributions. The total

Table 3: Observed data and predicted SM event yields in the signal region. The MC predictions are normalized to the theoretical cross sections in Table 2. The relative uncertainty of the total SM prediction is $O(10\%)$.

Process	7 TeV	8 TeV
Wjj (EW)	920	5600
Wjj (QCD)	3020	19600
Multijets	500	2350
$t\bar{t}$	430	1960
Single top	244	1470
Zjj (QCD)	470	1140
Dibosons	126	272
Zjj (EW)	5	79
Total SM	5700	32500
Data	6063	33719

relative systematic uncertainty of the multijet normalization in the muon (electron) channel is 28% (67%) for the $\sqrt{s} = 7$ TeV analysis, and 36% (38%) for the $\sqrt{s} = 8$ TeV analysis. The relatively large uncertainty in the $\sqrt{s} = 7$ TeV electron channel results from a larger dependence on the fit distribution and range than in the other multijet fits.

4.3 Distributions and yields

The distributions of lepton centrality and the minimum centrality of additional jets, which are used to separate signal, control, and validation regions, are shown in Figure 5 for the 7 and 8 TeV data and the corresponding SM predictions after the preselection. The comparisons of the SM predictions to data show general agreement within the estimated uncertainties. The predictions include correction factors for lepton identification and triggering, and the bands correspond to the combination of statistical uncertainties and the experimental uncertainties described in Section 2. The signal-region dijet mass distributions, used to fit for the signal yield in the fiducial and total cross-section measurements, are shown in Figure 6 for both data sets. The figure also shows the dijet rapidity difference, which is correlated with dijet mass and demonstrates an enhancement in signal at high values. Table 3 details the data and SM predictions for the individual processes in the signal region, and Table 4 shows the total predictions and the observed data in each of the fiducial regions defined in Section 3.

5 Fiducial and total electroweak Wjj cross sections

The measurement of the fiducial EW Wjj cross section in the signal region uses a control-region constraint to provide a precise determination of the electroweak production cross section for W bosons produced in association with dijets at high invariant mass. The measurement is performed with an extended

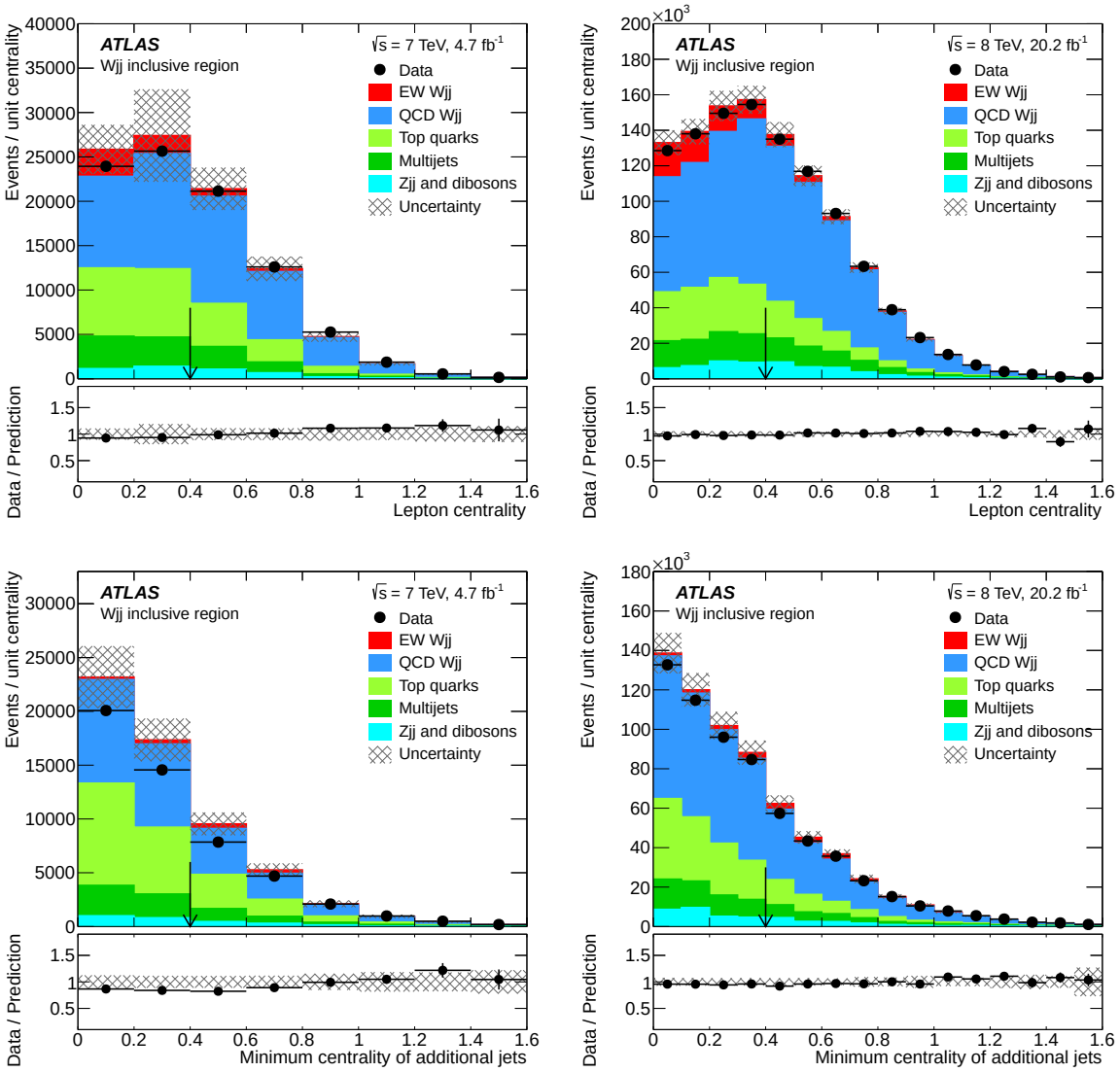

Figure 5: Predicted and observed distributions of the lepton centrality (top) and the minimum centrality of additional jets (bottom) for events in the inclusive fiducial region (i.e. after preselection) in 7 TeV (left) and 8 TeV (right) data. The arrows in the lepton-centrality distributions separate the signal-region selection (to the left) from the control-region selection (to the right). The arrows in the jet-centrality distributions separate the signal-region selection (to the right) from the validation-region selection (to the left). The bottom panel in each distribution shows the ratio of data to the prediction. The shaded band represents the statistical and experimental uncertainties summed in quadrature.

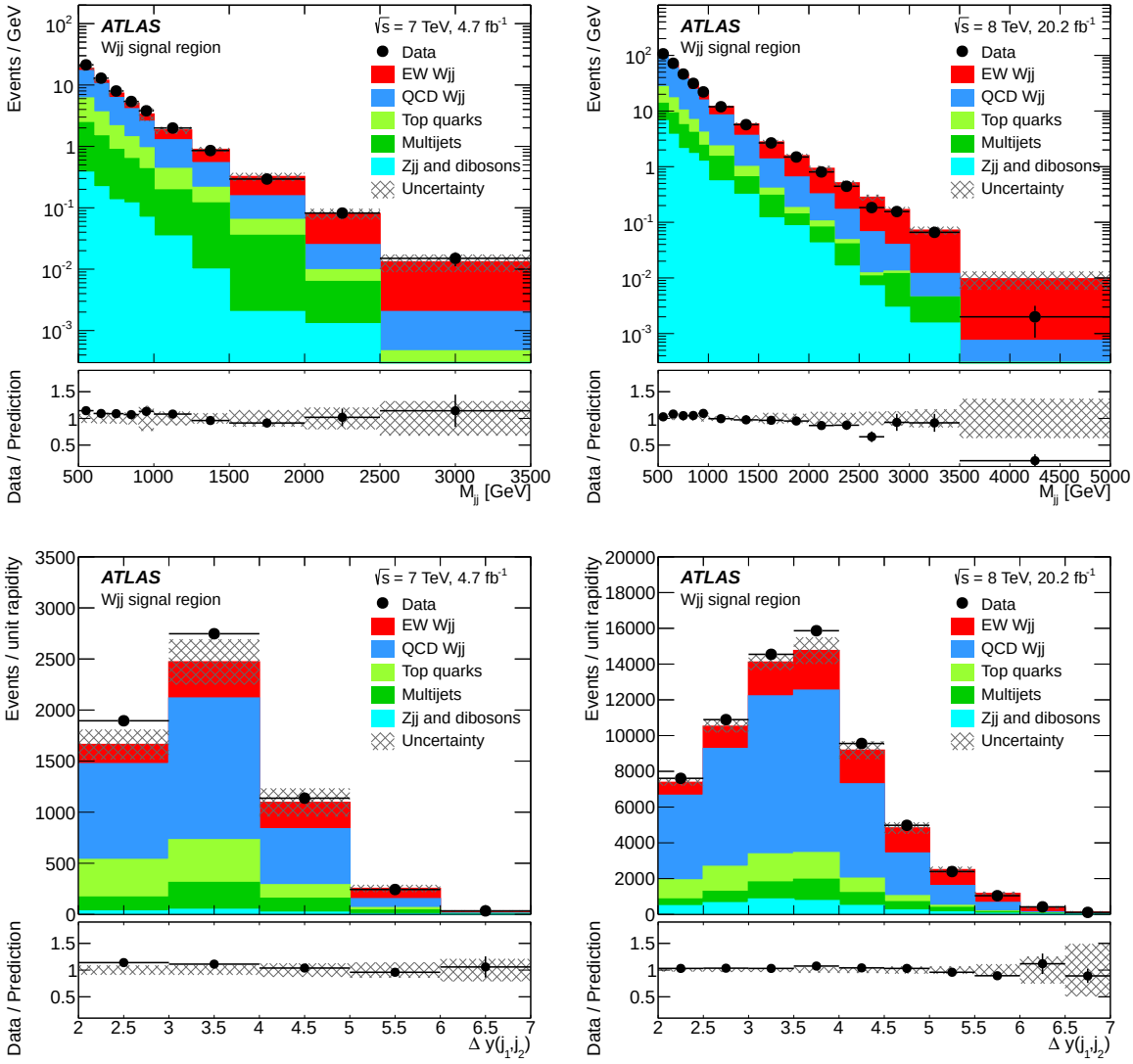

Figure 6: Predicted and observed distributions of the dijet invariant mass (top) and $\Delta y(j_1, j_2)$ (bottom) for events in the signal region in 7 TeV (left) and 8 TeV (right) data. The bottom panel in each distribution shows the ratio of data to the prediction. The shaded band represents the statistical and experimental uncertainties summed in quadrature.

Table 4: Observed data and total predicted SM event yields in each measurement region. The MC predictions are normalized to the theoretical cross sections times branching ratios in Table 2. The relative uncertainty of the total SM prediction is $O(10\%)$.

Region name	7 TeV		8 TeV	
	SM prediction	Data	SM prediction	Data
Fiducial and differential measurements				
Signal region	5700	6063	32500	33719
Forward-lepton control region	5000	5273	29400	30986
Central-jet validation region	2170	2187	12400	12677
Differential measurement only				
Inclusive region, $M_{jj} > 500$ GeV	-	-	106000	107040
Inclusive region, $M_{jj} > 1$ TeV	-	-	17400	16849
Inclusive region, $M_{jj} > 1.5$ TeV	-	-	3900	3611
Inclusive region, $M_{jj} > 2$ TeV	-	-	1040	890
Forward-lepton/central-jet region	-	-	12000	12267
High-mass signal region	-	-	6100	6052
Anomalous coupling measurements only				
High-q^2 region	-	-	39	30

joint binned likelihood fit [76] of the M_{jj} distribution for the normalization factors of the QCD and electroweak Wjj Powheg +Pythia8 predictions, μ_{QCD} and μ_{EW} respectively, defined as follows:

$$\begin{aligned}(\sigma_i \times \mathcal{B}_{W\to\ell\nu} \times \mathcal{A}_i)^{\mathrm{meas}} &= \mu_i \cdot (\sigma_i \times \mathcal{B}_{W\to\ell\nu} \times \mathcal{A}_i)^{\mathrm{theo}} \\ &= \frac{N_i}{C_i \mathcal{L}},\end{aligned}$$

where σ_i is the cross section of process i (QCD or EW Wjj production), $\mathcal{B}_{W\to\ell\nu}$ is the branching fraction of the W boson to electron or muon, $\mathcal{A}_i$ is the acceptance for events to pass the signal selection at the particle level (see Table 1), N_i is the number of measured events, $\mathcal{L}$ is the integrated luminosity, and C_i is the ratio of reconstructed to generated events passing the selection and accounts for experimental efficiencies and resolutions. The fit includes a Gaussian constraint for all non-Wjj backgrounds, and accounts only for statistical uncertainties in the expected yield. The fit result for μ_{EW} is translated into a fiducial cross section by multiplying μ_{EW} by the predicted fiducial cross section from Powheg + Pythia8. In addition, the total cross section for jets with $p_{\mathrm{T}} > 20$ GeV is calculated by dividing the fiducial cross section by $\mathcal{A}$ for the EW Wjj process.

The dijet mass provides the discriminating fit distribution. The region at relatively low invariant mass ($\approx$ 500–1000 GeV) has low signal purity and primarily determines μ_{QCD}, while events with higher invariant mass have higher signal purity and mainly determine μ_{EW}. The interference between the processes is not included in the fit, and is instead taken as an uncertainty based on SM predictions.

The uncertainty in the shape of the QCD Wjj distribution dominates the measurement, but is reduced by using the forward-lepton control region to correct the modelling of the M_{jj} shape. This control region is defined in Table 1 and uses the same selection as the signal region, except for the inversion of the

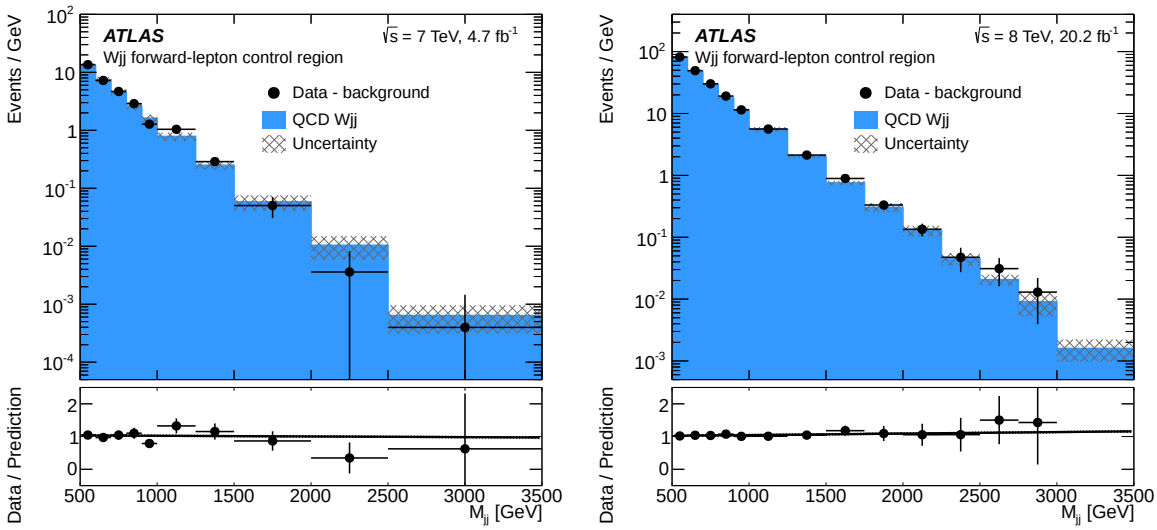

Figure 7: Comparison of the predicted QCD Wjj dijet mass distribution to data with background processes subtracted, for events in the forward-lepton control region in 7 TeV (left) and 8 TeV (right) data. The bottom panel in each distribution shows the ratio of data to the QCD Wjj prediction, and the result of a linear fit to the ratio. The error bars represent statistical and experimental uncertainties summed in quadrature.

central-lepton requirement. This section describes the application of the control-region constraint, the uncertainties in the measurement, and the results of the fit.

5.1 Control-region constraint

The SM prediction of the dijet mass distribution receives significant uncertainties from the experimental jet energy scale and resolution. These uncertainties are constrained with a correction to the predicted distribution derived using data in a control region where the signal contribution is suppressed. This forward-lepton control region is selected using the lepton centrality distribution. Residual uncertainties arise primarily from differences in the dijet mass spectrum between the control region and the signal region.

To derive the M_{jj} correction, all processes other than strong Wjj production are subtracted from the data and the result is compared to the prediction (Figure 7). The correction is then determined with a linear statistical fit to the ratio of the subtracted data to the Wjj prediction. The slopes of the fits in 7 and 8 TeV data are consistent with zero; they are (0.2 ± 1.1)%/ TeV and (0.28 ± 0.43)%/ TeV, respectively, where the uncertainties are statistical only. The effect of a slope correction of 1%/ TeV is approximately 0.1 in the measured μ_{EW}.

Systematic uncertainties in the corrected dijet mass distribution in the signal and validation regions are estimated by varying each source of uncertainty up or down by 1σ and calculating the corresponding slope correction in the control region in the simulation. This correction is applied to the prediction in the signal region and the fit performed on pseudodata derived from the nominal prediction. The resulting change in μ_{EW} is taken as the corresponding systematic uncertainty. The method is illustrated in the central-jet validation region in Figure 8, where the background-subtracted and corrected Wjj dijet mass

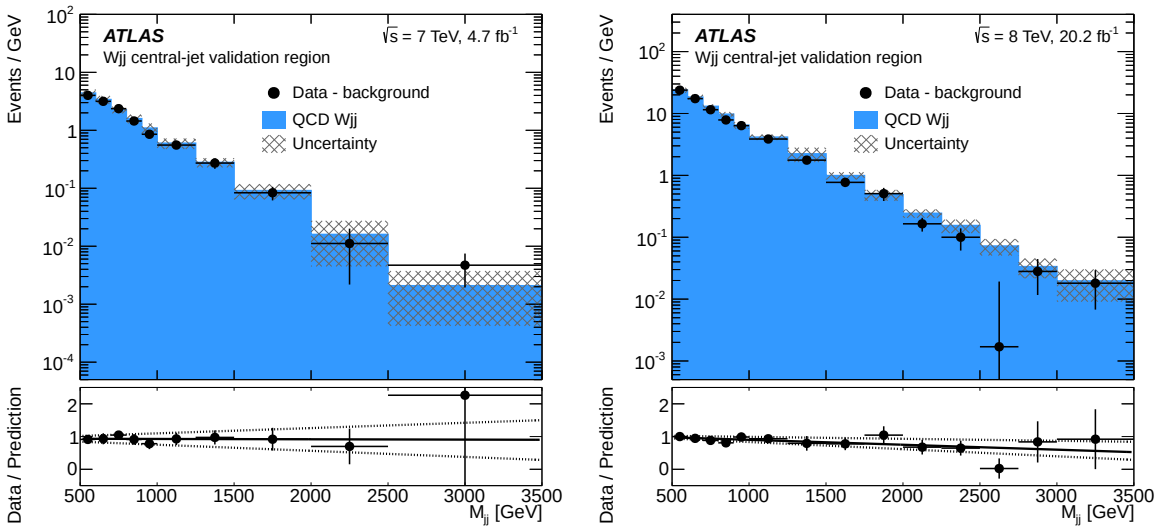

Figure 8: Comparison of the corrected QCD Wjj background dijet mass distribution to data with background processes subtracted, for events in the central-jet validation region in 7 TeV (left) and 8 TeV (right) data. The bottom panel in each subfigure shows the ratio of data to prediction, and the result of a linear fit to the ratio (solid line). The error bars represent statistical and experimental uncertainties summed in quadrature. The dotted lines show the fit with slope adjusted up and down by statistical and experimental uncertainties.

distribution is compared to data. The ratio of subtracted data to the corrected Wjj prediction is consistent with a line of zero slope when considering statistical and experimental uncertainties (the dotted lines in the figure).

5.2 Uncertainties in μ_{EW}

Uncertainties in μ_{EW} consist of: statistical uncertainties in the fit to the normalizations of the signal and background Wjj processes in the signal region; the statistical uncertainty of the correction from the control region; and experimental and theoretical uncertainties affecting the signal and background predictions. Table 5 summarizes the uncertainties in the measurement of μ_{EW}.

The total statistical uncertainty in μ_{EW} of the joint likelihood fit is 0.16 (0.052) in 7 (8) TeV data, where the leading uncertainty is the statistical uncertainty of the data in the control region rather than in the signal region.

Systematic uncertainties affecting the MC prediction are estimated by varying each uncertainty source up and down by 1σ in all MC processes, fitting the ratio of the varied QCD Wjj prediction to the nominal prediction in the control region, and performing the signal region fit using the varied samples as pseudodata and the nominal samples as the templates. The largest change in μ from the up and down variations is taken as a symmetric uncertainty. The dominant experimental uncertainty in μ_{EW} is due to the calibration of the η dependence of the jet energy scale, and is 0.124 (0.053) in 7 (8) TeV data. Other uncertainties in the jet energy scale (JES) and resolution (JER) are of similar size when combined, with the largest contribution coming from the uncertainty in modelling the ratio of responses to quarks

Table 5: The statistical and systematic uncertainty contributions to the measurements of μ_{EW} in 7 and 8 TeV data.

Source	Uncertainty in μ_{EW}	
	7 TeV	8 TeV
Statistical		
Signal region	0.094	0.028
Control region	0.127	0.044
Experimental		
Jet energy scale (η intercalibration)	0.124	0.053
Jet energy scale and resolution (other)	0.096	0.059
Luminosity	0.018	0.019
Lepton and $E_{\mathrm{T}}^{\mathrm{miss}}$ reconstruction	0.021	0.012
Multijet background	0.064	0.019
Theoretical		
MC statistics (signal region)	0.027	0.026
MC statistics (control region)	0.029	0.019
EW Wjj (scale and parton shower)	0.012	0.031
QCD Wjj (scale and parton shower)	0.043	0.018
Interference (EW and QCD Wjj)	0.037	0.032
Parton distribution functions	0.053	0.052
Other background cross sections	0.002	0.002
EW Wjj cross section	0.076	0.061
Total	0.26	0.14

and gluons. Uncertainties due to multijet modelling are estimated by separately varying the normalization and distribution of the multijet background in each phase-space region and combining the effects in quadrature.

Theoretical uncertainties arise from the statistical uncertainty on the MC predictions; the lack of interference between signal and background Wjj processes in the MC modelling; Wjj renormalization and factorization scale variations and parton-shower modelling, which affect the acceptance of the jet centrality requirement; parton distribution functions; and cross-section uncertainties. The uncertainty due to MC statistics is 0.040 (0.032) in 7 (8) TeV data. The interference uncertainty is estimated by including the SHERPA leading-order interference model as part of the background Wjj process and affects the measurement of μ_{EW} by 0.037 (0.032) in 7 (8) TeV data. Uncertainties due to PDFs are 0.053 (0.052) for 7 (8) TeV data. Scale and parton-shower uncertainties are ≈ 0.04 in both the 7 and 8 TeV measurements. The scale uncertainty in EW Wjj production is larger at $\sqrt{s} = 8$ TeV than at 7 TeV because of the increasing uncertainty with dijet mass and the higher mean dijet mass at 8 TeV. The scale uncertainty in QCD Wjj production is larger at $\sqrt{s} = 7$ TeV because the data constraint has less statistical power than at 8 TeV.

Finally, a 0.076 (0.061) uncertainty in the signal cross section at 7 (8) TeV due to higher-order QCD corrections and non-perturbative modelling is estimated using scale and parton-shower variations, affecting the measurement of μ_{EW} but not the extracted cross sections.

5.3 Electroweak Wjj cross-section results

The dijet mass distributions in 7 and 8 TeV data after fitting for μ_{EW} and μ_{QCD} are shown in Figure 9. There is good overall agreement between the normalized distributions and the data. The fit results for μ_{QCD} are 1.16 ± 0.04 (stat) for 7 TeV data, and 1.09 ± 0.02 (stat) for 8 TeV data. The measured values of μ_{EW} are consistent between electron and muon channels, with the following combined results:

$$\begin{aligned} \mu_{\mathrm{EW}}\ (7\ \mathrm{TeV}) &= 1.00 \pm 0.16\ (\mathrm{stat}) \pm 0.17\ (\mathrm{exp}) \pm 0.12\ (\mathrm{th}), \\ \mu_{\mathrm{EW}}\ (8\ \mathrm{TeV}) &= 0.81 \pm 0.05\ (\mathrm{stat}) \pm 0.09\ (\mathrm{exp}) \pm 0.10\ (\mathrm{th}). \end{aligned}$$

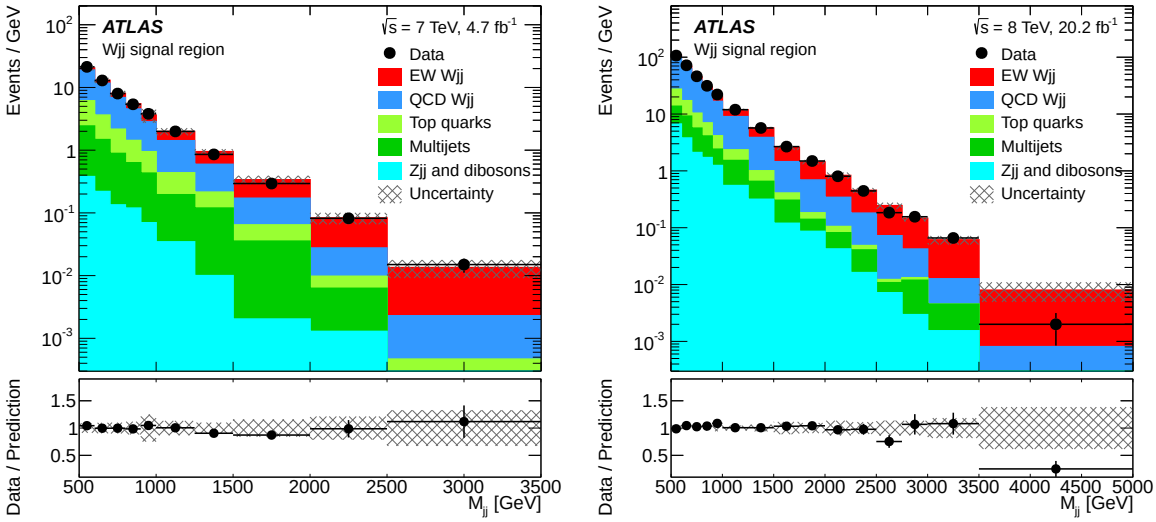

Figure 9: Distributions of the dijet invariant mass for events in the signal region in 7 TeV (left) and 8 TeV (right) data, after fitting for the yields of the individual Wjj processes. The bottom panel in each distribution shows the ratio of data to predicted signal-plus-background yields. The shaded band centred at unity represents the statistical and experimental uncertainties summed in quadrature.

The measured value of μ_{EW} has a total uncertainty of 0.26 (0.14) in 7 (8) TeV data, and differs from the SM prediction of unity by $< 0.1\sigma$ (1.3σ). In the absence of a control region, the uncertainty would increase to 0.37 (0.18) in 7 (8) TeV data.

The fiducial signal region is defined by the selection in Table 1 using particle-level quantities after parton showering. The measured and predicted cross sections times branching ratios in this region are shown in Table 6. The acceptance is calculated using Powheg + Pythia8 with a dominant uncertainty due to the parton-shower modelling which is estimated by taking the difference between Powheg + Pythia8 and Powheg + Herwig++. The uncertainty in the predicted fiducial cross section at $\sqrt{s} = 8$ TeV includes a 4 fb contribution from scale variations and an 11 fb contribution from parton-shower modelling.

A summary of this measurement and other measurements of boson production at high dijet invariant mass is shown in Figure 10, normalized to SM predictions. The measurement with the smallest relative uncertainty is the 8 TeV Wjj measurement presented here.

Table 6: Measured fiducial cross sections of electroweak Wjj production in a single lepton channel, compared to NLO QCD predictions from Powheg + Pythia8. The acceptances and the inclusive measured production cross sections with $p_{\mathrm{T}} > 20$ GeV jets are also shown.

$\sqrt{s}$	$\sigma^{\mathrm{fid}}_{\mathrm{meas}}$ [fb]	$\sigma^{\mathrm{fid}}_{\mathrm{SM}}$ [fb]	Acceptance $\mathcal{A}$	$\sigma^{\mathrm{inc}}_{\mathrm{meas}}$ [fb]
7 TeV	144 ± 23 (stat) ± 23 (exp) ± 13 (th)	144 ± 11	0.053 ± 0.004	2760 ± 670
8 TeV	159 ± 10 (stat) ± 17 (exp) ± 20 (th)	198 ± 12	0.058 ± 0.003	2890 ± 510

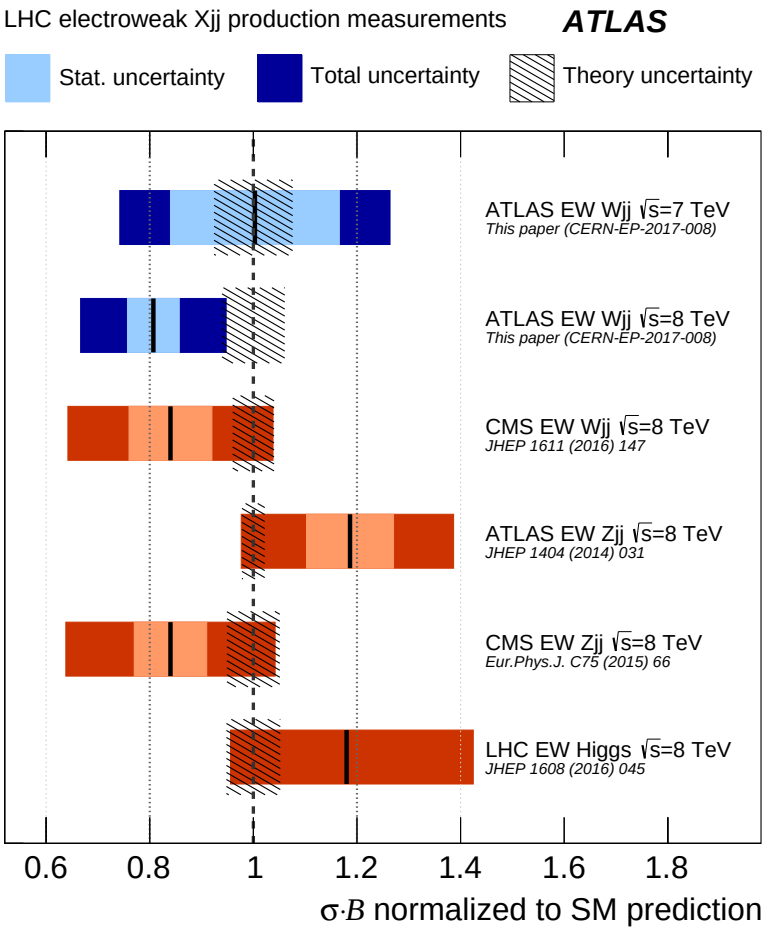

Figure 10: Measurements of the cross section times branching fractions of electroweak production of a single W, Z, or Higgs boson at high dijet invariant mass, divided by the SM predictions (Powheg +Pythia8 for ATLAS, Madgraph +Pythia8 for CMS, and Powheg +Pythia8 for the LHC combination). The lighter shaded band (where shown) represents the statistical uncertainty of the measurement, the outer darker band represents the total measurement uncertainty. Theoretical uncertainties in the SM prediction are represented by the shaded region centred at unity.

6 Differential cross sections

Differential cross sections for Wjj production are measured with the higher integrated luminosity $\sqrt{s} = 8$ TeV data set as a function of a variety of observables (detailed below) and in a number of fiducial phase-space regions. The combined QCD+EW Wjj production is measured in all regions to test the modelling of QCD Wjj production. In regions sensitive to EW Wjj contributions, the prediction for QCD Wjj only is shown along with the combined QCD+EW Wjj prediction in order to indicate the effect of the EW Wjj process. Differential measurements of EW Wjj production are performed in regions with $M_{jj} > 1.0$ TeV.

All differential production cross sections are measured both as absolute cross sections and as distributions normalized by the cross section of the measured fiducial region (σ_W^{fid}). Many sources of uncertainty are reduced for normalized distributions, allowing higher-precision tests of the modelling of the shape of the measured observables in Monte Carlo simulations. The reported cross sections include the branching fraction for the $W \to \ell^{\pm}\nu$ decay of a single flavour and are normalized by the width of the measured bin interval. This section discusses representative differential measurements, with additional distributions provided in Appendix A. The complete set of measurements is available in HEPDATA [77].

The MC simulations are used to correct the cross sections for detector and event selection inefficiencies, and for the effect of detector resolutions. An implementation [78] of a Bayesian iterative unfolding technique [79] is used to perform these corrections. The unfolding is based on a response matrix from the simulated events which encodes bin-to-bin migrations between a particle-level differential distribution and the equivalent reconstruction-level distribution. The matrix gives transition probabilities from particle level to reconstruction level, and Bayes' theorem is employed to calculate the inverse probabilities. These probabilities are used in conjunction with a prior particle-level signal distribution, which is implicitly taken from the POWHEG + PYTHIA8 simulations, to unfold the background-subtracted reconstruction-level data distributions. After this first unfolding iteration the unfolded data distribution is used as the new prior and the process repeated for another iteration. The unfolding procedure is validated by unfolding the SHERPA simulation using the POWHEG + PYTHIA8 response matrix. For all distributions the unfolded and initial particle-level SHERPA predictions agree within the unfolding uncertainty assigned. Bin boundaries in unfolded distributions are chosen to ensure that > 66% of particle-level events remain within the same interval at reconstruction level.

Unfolded differential cross-section measurements are compared to theoretical predictions for QCD+EW Wjj production from the POWHEG + PYTHIA8, SHERPA, and HEJ event generators, which are described in Section 4.1. The normalizations are performed self-consistently, i.e. data measurements are normalized by the total fiducial data cross section and MC predictions are normalized by the corresponding MC cross section.

6.1 Observables and fiducial regions

Differential measurements are performed in distributions that provide discrimination between strong and electroweak Wjj production, and enhanced sensitivity to anomalous gauge couplings. The observables sensitive to electroweak Wjj production are:

- C_ℓ, lepton centrality, the location in rapidity of the lepton relative to the average rapidity of the two highest-p_{T} jets, defined in Eq. (1);

- C_j, jet centrality, the location in rapidity of any additional jet relative to the average rapidity of the two highest-p_{T} jets, defined in Eq. (1);
- M_{jj}, the invariant mass of the two highest-p_{T} jets;
- $\Delta y(j_1, j_2)$, the absolute rapidity separation between the two highest-p_{T} jets;
- $N_{\mathrm{jets}}^{\mathrm{gap}}$, the number of additional jets in the rapidity gap bounded by the two highest-p_{T} jets (i.e., jets with $C_j < 0.5$).

Additional observables sensitive to anomalous couplings are:

- $p_{\mathrm{T}}^{j_1}$, the p_{T} of the highest-p_{T} jet;
- p_{T}^{jj}, the p_{T} of the dijet system (vector sum of the p_{T} of the two highest-p_{T} jets);
- $\Delta\phi(j_1, j_2)$, the magnitude of the azimuthal angle between the two highest-p_{T} jets,

where the last observable is sensitive specifically to CP-violating couplings.

The differential cross sections of the combined Wjj processes are measured in the following nine fiducial regions:

- Four mutually orthogonal fiducial regions defined in Figure 4, three of which are electroweak-suppressed (< 5% contribution) and one electroweak-enhanced (15–20% contribution);
- An additional electroweak-enhanced signal region with $M_{jj} > 1.0$ TeV (35–40% electroweak Wjj contribution);
- Four inclusive fiducial regions defined by the preselection requirements in Table 1 with $M_{jj} >$ 0.5, 1.0, 1.5 and 2.0 TeV.

The inclusive fiducial regions probe the observables used to separate the signal and control or validation regions, namely lepton and jet centrality, as well as the number of jets radiated in the rapidity gap between the two leading jets. The four successively higher invariant mass thresholds increasingly enhance the EW Wjj purity of the differential distributions, without the lepton and jet topology requirements applied to the dedicated signal-enhanced regions.

Figure 11 shows the Powheg + Pythia8 and Sherpa predictions of the fraction of Wjj events produced via electroweak processes, as a function of the number of jets emitted in the dijet rapidity gap for the inclusive fiducial regions with $M_{jj} > 0.5$ TeV and the dijet invariant mass in the signal fiducial region. The EW Wjj signal is enhanced in events with zero jets in the dijet rapidity gap due to the absence of colour connection between the incoming partons.

In addition to the measurements of differential cross sections for combined QCD+EW Wjj production in the nine fiducial regions listed above, EW Wjj differential cross sections are extracted in four fiducial regions that have an expected EW Wjj fraction of > 20%: the three highest invariant-mass inclusive regions ($M_{jj} > 1.0$ TeV, 1.5 TeV, and 2.0 TeV), and the high-mass signal region ($M_{jj} > 1.0$ TeV); the latter has the highest expected total EW Wjj signal purity, about 40%. The QCD Wjj background is subtracted using the multiplicative normalization factor of $\mu_{\mathrm{QCD}} = 1.09 \pm 0.02$ (stat) determined from the fits in Section 5. This substantially reduces the normalization uncertainty, confining theoretical uncertainties to the shapes of the background distributions.

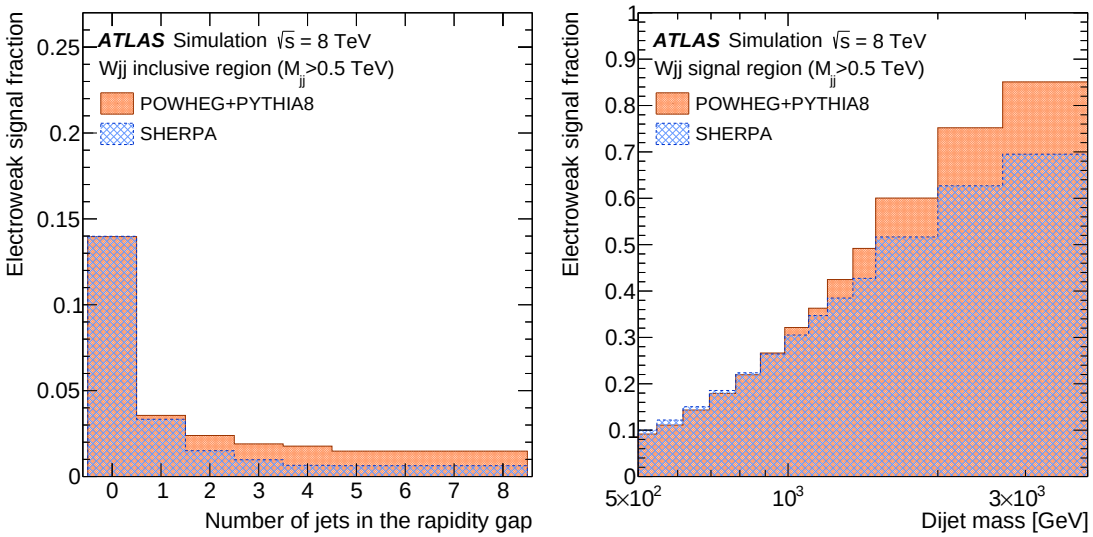

Figure 11: Fraction of EW Wjj signal relative to the combined QCD+EW Wjj production, predicted by Powheg + Pythia8 and Sherpa simulations for observables in the inclusive and signal regions.

Performing a complete unfolding of the EW Wjj signal process leads to better precision on the unfolded data, particularly in the case of normalized distributions, than could be achieved by subtracting the particle-level QCD Wjj production background from unfolded QCD+EW Wjj production data. All EW Wjj differential measurements are nonetheless also performed as combined QCD+EW Wjj production measurements so that such a subtraction could be performed with other QCD Wjj predictions.

6.2 Uncertainties

The sources of uncertainty discussed in Section 5 are assessed for the unfolded differential production cross sections. Figures are shown with statistical uncertainties as inner bars and total uncertainties as the outer bars.

Statistical uncertainties are estimated using pseudoexperiments, with correlations between bins determined using a bootstrap method [80]. The $W \to ev$ and $W \to \mu\nu$ channels are found to be statistically compatible, and are combined. Theoretical uncertainties include the effects of scale and PDF variations on the prior distribution and on the response matrix. For unfolding EW Wjj production, additional theoretical uncertainties arise from modelling the QCD Wjj contribution subtracted from the data, and from the neglect of interference between the strong and electroweak Wjj processes. The interference uncertainty is estimated using the same procedure as for the fiducial measurement (Section 5), i.e. by adding the Sherpa interference model to the background prediction. An uncertainty in the unfolding procedure is estimated by reweighting the simulation such that the distributions match the unfolded data, and then unfolding the data with the reweighted simulation; the change in the unfolded measurement is symmetrized and taken as an uncertainty. Experimental uncertainties are assessed by unfolding the data distributions using a modified response matrix and prior incorporating the change in detector response.

Figure 12 summarizes the statistical uncertainties and the statistical and systematic uncertainties summed in quadrature of the unfolded distributions for a selection of observables for the combined QCD+EW Wjj processes. The jet energy scale and resolution uncertainties dominate the total uncertainty except in

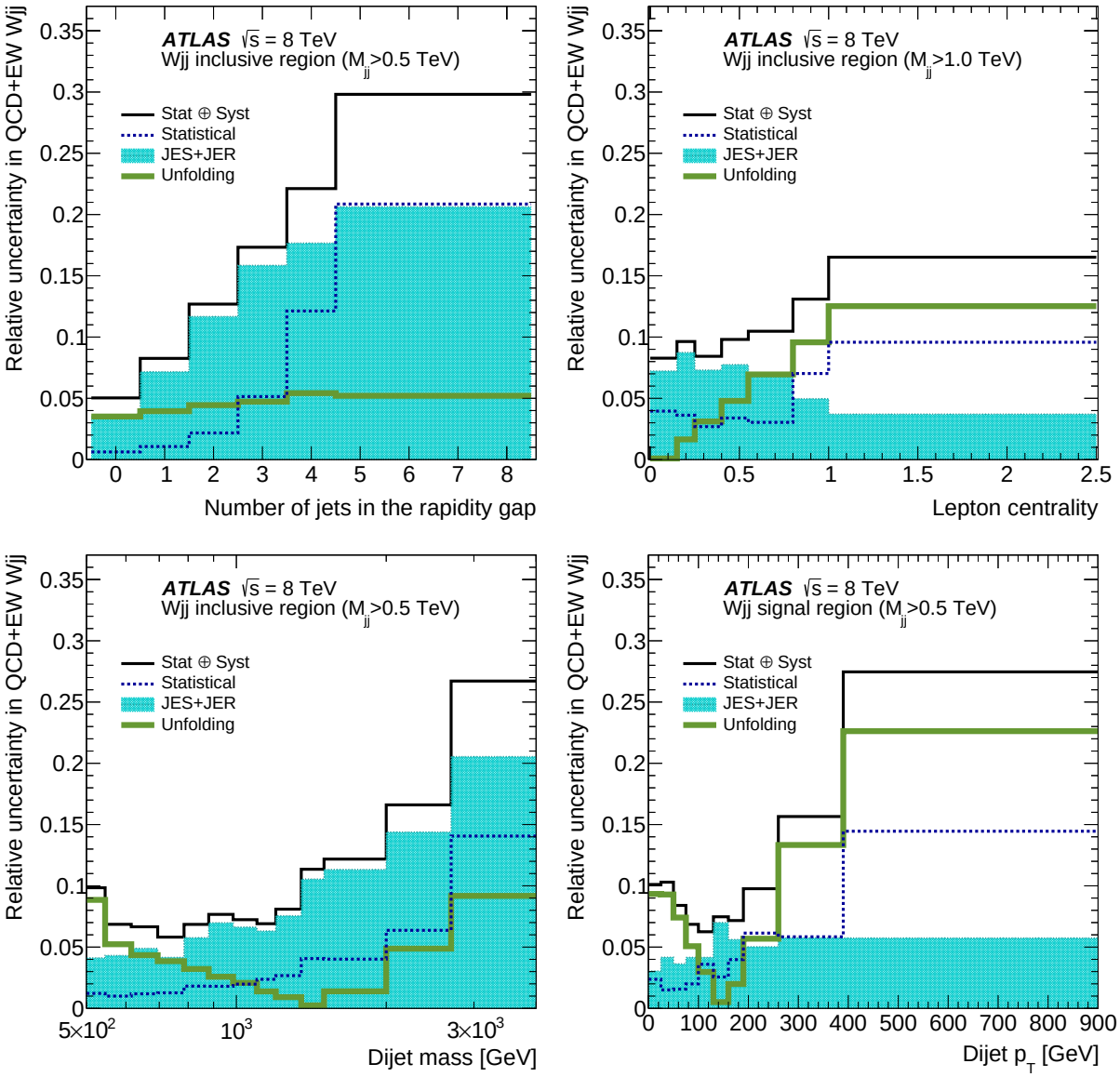

Figure 12: Relative uncertainties in example unfolded differential cross sections for the combined QCC+EW Wjj processes. The examples are: the number of jets in the rapidity gap between the two highest-p_{T} jets in the inclusive region (top left); the lepton centrality distribution in the inclusive $M_{jj} > 1$ TeV region (top right); M_{jj} in the inclusive region (bottom left); and the dijet p_{T} in the signal region (bottom right). Dominant contributions to the total systematic uncertainty are highlighted separately.

regions where statistical uncertainties are significant. The unfolding uncertainty is typically relevant in these regions and in regions dominated by QCD Wjj production where the statistical uncertainties are small.

Figure 13 summarizes the uncertainty contributions to example EW Wjj unfolded data distributions. Uncertainties in the modelling of strong Wjj production are particularly important at low dijet invariant mass, where the EW Wjj signal purity is lowest. Interference uncertainties become dominant at low dijet rapidity separation but are otherwise not the leading contribution to the total uncertainty. A re-

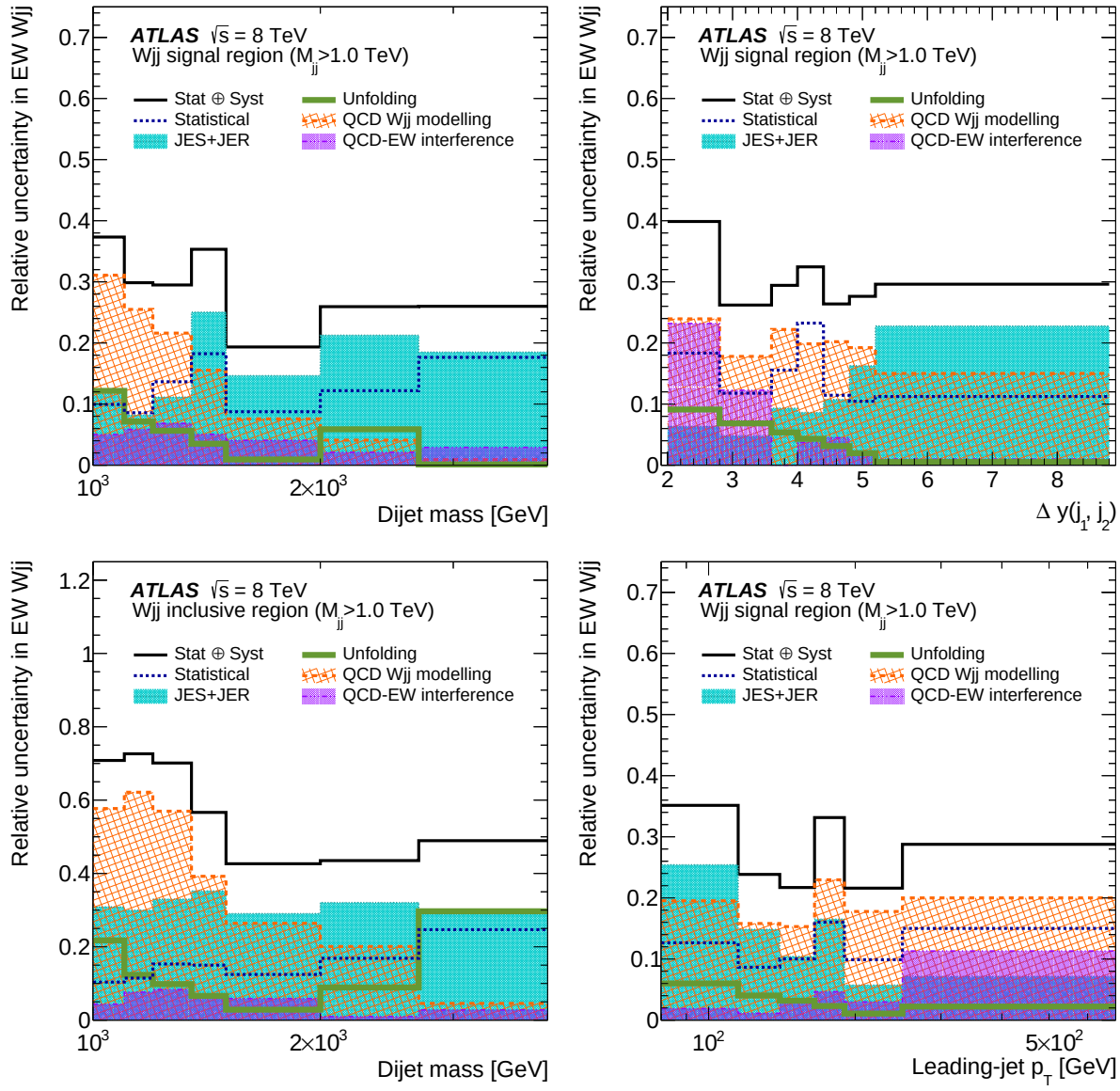

Figure 13: Relative uncertainties in example unfolded differential cross sections for the EW Wjj processes. The examples are M_{jj} (top left) and $\Delta y(j_1, j_2)$ (top right) in the high-mass signal region; M_{jj} in the $M_{jj} > 1$ TeV inclusive region (bottom left); and leading-jet p_{T} in the high-mass signal region (bottom right). Dominant contributions to the total systematic uncertainty are highlighted separately.

cent study [81] of interference in Z+jets vector-boson-fusion topologies, incorporating NLO electroweak corrections, predicted similar behaviour. For the bulk of the EW Wjj distributions, the leading sources of uncertainty are statistical, QCD Wjj modelling, and jet energy scale and resolution, and contribute roughly equally.

6.3 Combined strong and electroweak Wjj measurements

This section reports the combined strong and electroweak Wjj differential cross-section results, with comparisons to the MC predictions given by Sherpa, Powheg + Pythia8, and hej. Comparisons to hej are only performed in regions of high purity for strong Wjj production, as discussed in Section 4.1.

Figure 14 shows the normalized differential cross section as a function of the number of $p_{\mathrm{T}} > 30$ GeV jets emitted into the rapidity gap for progressively increasing M_{jj} thresholds. In the lowest invariant-mass fiducial region, strong Wjj production dominates and predictions from Powheg + Pythia8, Sherpa, and hej all describe the data well, for up to eight additional jet emissions. As the dijet invariant mass threshold is increased, the differences in shape between predictions with and without the EW Wjj contribution become apparent.

The value in the zero-jet bin corresponds to the efficiency of a central jet veto for each dijet invariant mass threshold. This efficiency is higher for EW Wjj production due to the absence of colour exchange; as the M_{jj} threshold increases the EW Wjj purity increases and its effect on the efficiency increases. Table 7 summarizes the measured jet-veto efficiency and the predictions from Powheg + Pythia8 QCD and QCD+EW Wjj simulations. The data efficiencies quoted in Table 7 show compatibility with the efficiencies of the combined Wjj processes in the simulation.

Jet centrality is related to the number of jets in the rapidity gap, as events with $C_j < 0.5$ have a jet within the gap. Figure 15 shows good agreement between the predictions and data in the differential cross section weighted by the mean number of gap jets.

The differential cross section in the inclusive region as a function of lepton centrality is shown in Figure 15 for two M_{jj} thresholds. These measurements indirectly probe the rapidity of the W boson relative to the dijet rapidity interval. Data with lepton centrality below 0.4 correspond to the presence of a lepton inside the rapidity region defined in Figure 3. All theoretical predictions adequately describe the lepton centrality in the region with the lowest dijet mass threshold, which is dominated by QCD Wjj production. As the M_{jj} threshold is increased the differences between QCD and QCD+EW Wjj production become more apparent, particularly at low lepton centrality where EW Wjj production is enhanced. At even larger invariant masses, Sherpa predicts a higher rate than data in the high-centrality, or forward-lepton, region (see Appendix A).

Figure 16 shows the cross sections as a function of the dijet invariant mass in four fiducial regions enriched in strong Wjj production: the inclusive region, the forward-lepton control region, the central-jet validation region, and the forward-lepton/central-jet validation region. Predictions from hej, which are expected to provide a good description of strong Wjj production at high dijet invariant mass where large logarithms contribute, are similar to the NLO predictions from Powheg + Pythia8. Sherpa predicts more events at high dijet invariant mass than observed in data in these fiducial regions, and has a larger disagreement in shape with the data, than Powheg + Pythia8 or hej. The dijet rapidity separation (Figure 17) also discriminates between strong (at low separation) and electroweak (at high separation) Wjj production, and is generally well modelled by the different predictions in the forward-lepton and central-jet fiducial

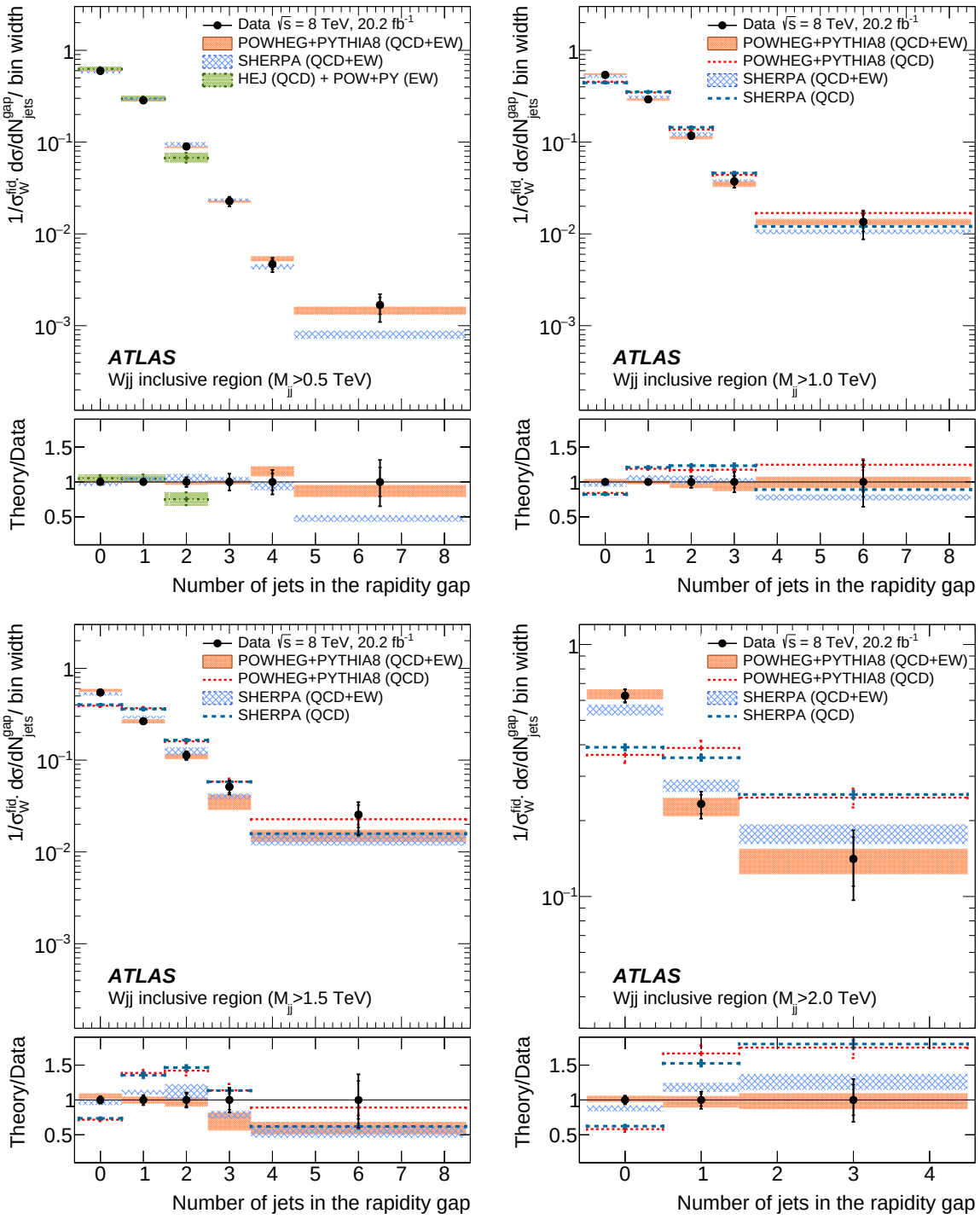

Figure 14: Unfolded normalized distribution of the number of jets with $p_{\mathrm{T}} > 30$ GeV in the rapidity interval bounded by the two highest-p_{T} jets in the inclusive fiducial region with M_{jj} thresholds of 0.5 TeV (top left), 1.0 TeV (top right), 1.5 TeV (bottom left), and 2.0 TeV (bottom right). Both statistical (inner bar) and total (outer bar) measurement uncertainties are shown, as well as ratios of the theoretical predictions to the data (the bottom panel in each distribution).

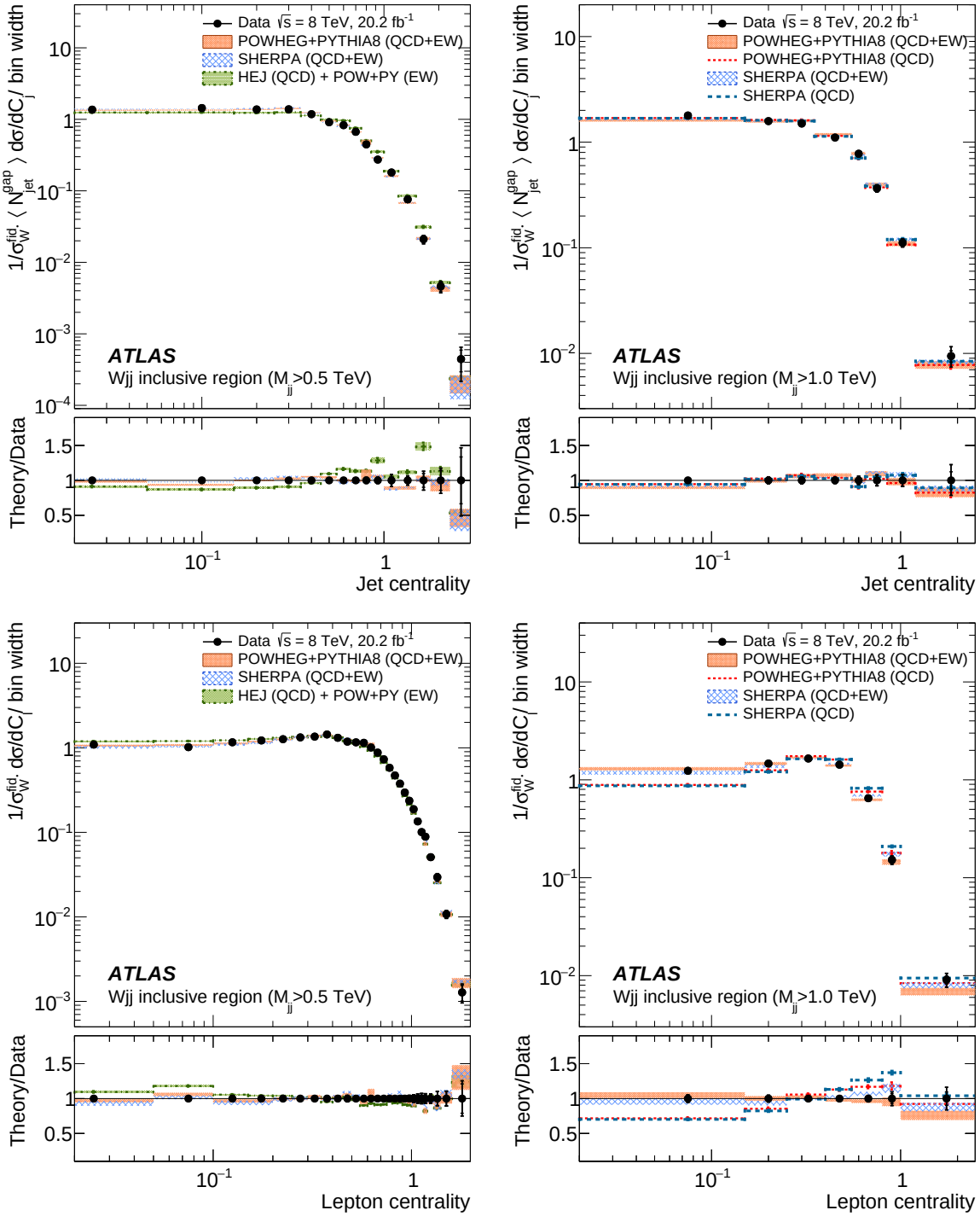

Figure 15: Unfolded normalized differential Wjj production cross sections as a function of jet centrality (top) and lepton centrality (bottom) for the inclusive fiducial region with $M_{jj} > 0.5$ TeV (left) and 1.0 TeV (right). Both statistical (inner bar) and total (outer bar) measurement uncertainties are shown, as well as ratios of the theoretical predictions to the data (the bottom panel in each distribution).

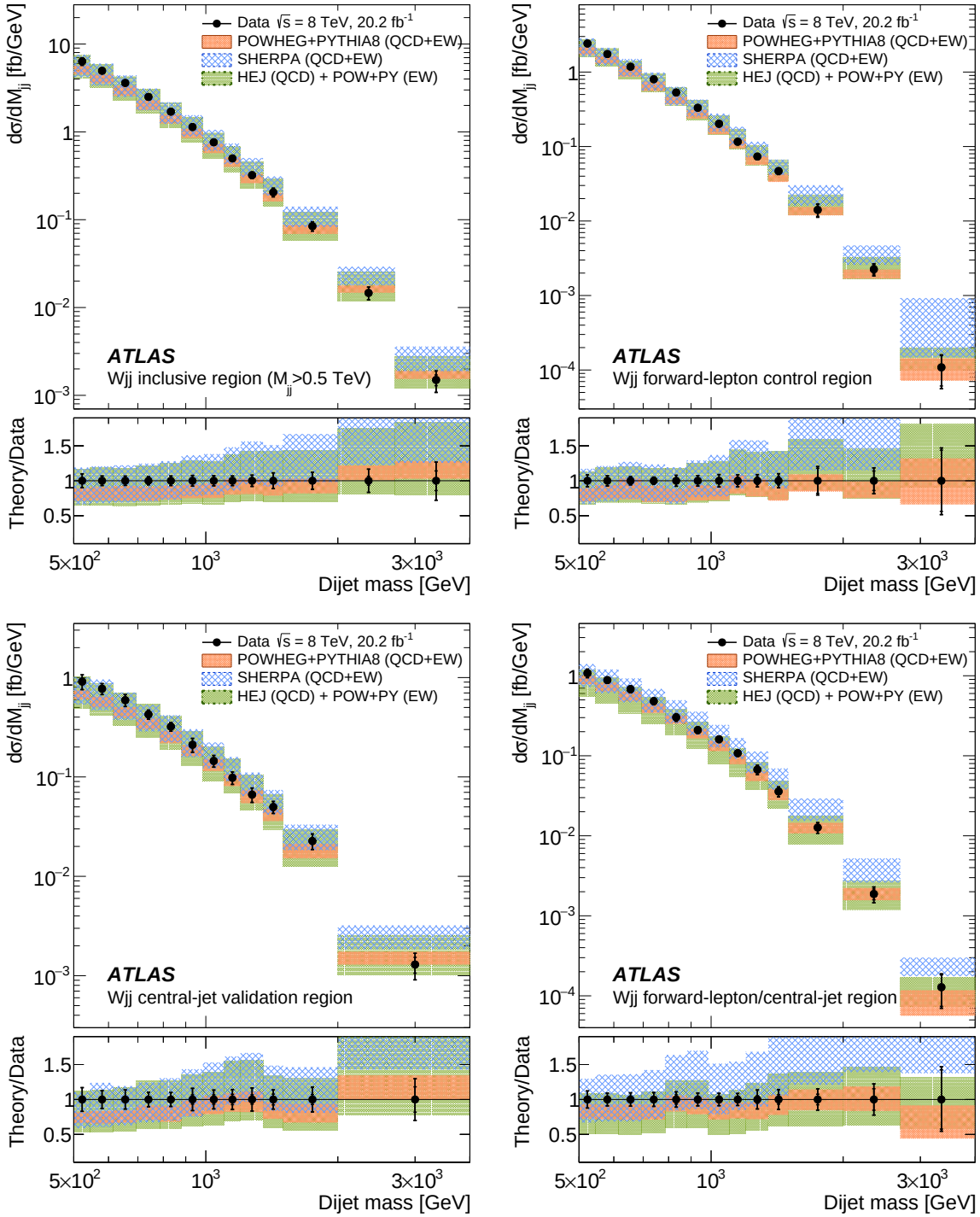

Figure 16: Unfolded differential Wjj production cross sections as a function of dijet mass for the inclusive (top left), forward-lepton (top right), central-jet (bottom left), and forward-lepton/central-jet (bottom right) fiducial regions, which are enriched in strong Wjj production. Both statistical (inner bar) and total (outer bar) measurement uncertainties are shown, as well as ratios of the theoretical predictions to the data (the bottom panel in each distribution).

Table 7: Jet-veto efficiency for each M_{jj} threshold compared to POWHEG + PYTHIA8 QCD+EW and QCD Wjj simulations. The uncertainties comprise statistical and systematic components added in quadrature.

	Jet-veto efficiency			
	$M_{jj} > 0.5$ TeV	$M_{jj} > 1.0$ TeV	$M_{jj} > 1.5$ TeV	$M_{jj} > 2.0$ TeV
Data	0.596 ± 0.014	0.54 ± 0.02	0.55 ± 0.03	0.63 ± 0.04
POWHEG +PYTHIA8 (QCD+EW)	0.597 ± 0.005	0.55 ± 0.01	0.57 ± 0.02	0.63 ± 0.03
POWHEG +PYTHIA8 (QCD)	0.569 ± 0.002	0.45 ± 0.01	0.39 ± 0.01	0.36 ± 0.03

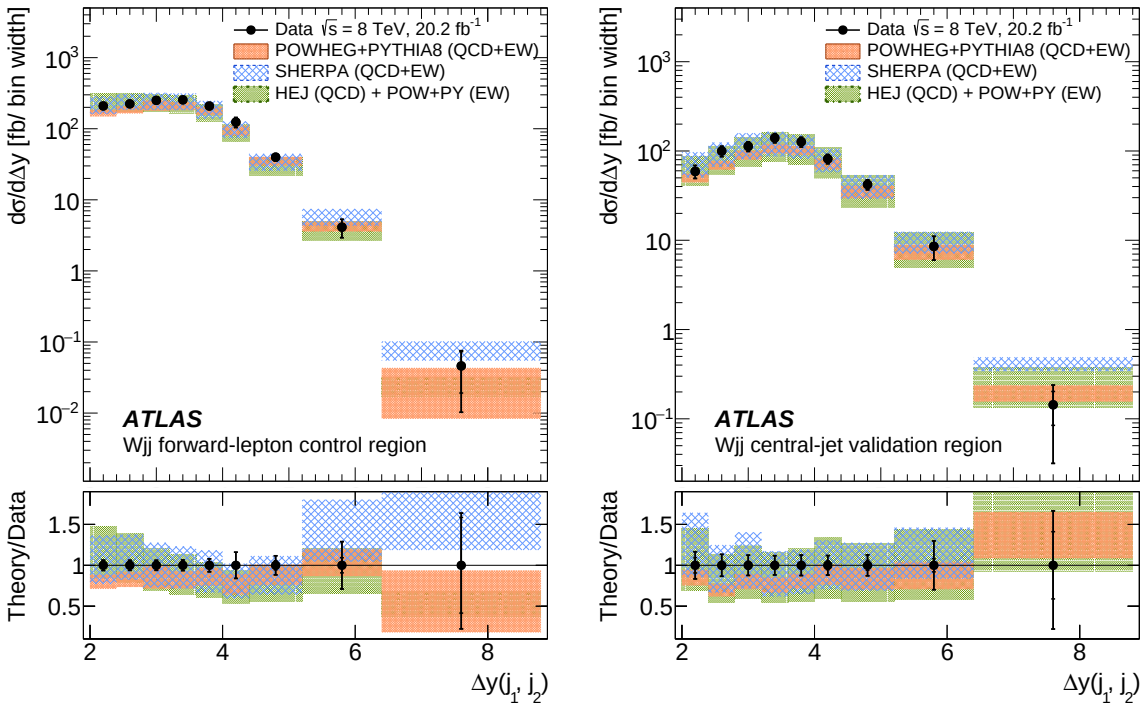

Figure 17: Unfolded absolute differential Wjj production cross sections as a function of dijet rapidity separation for the forward-lepton control and central-jet validation regions, which are dominated by strong Wjj production. Both statistical (inner bar) and total (outer bar) measurement uncertainties are shown, as well as ratios of the theoretical predictions to the data (the bottom panel in each distribution).

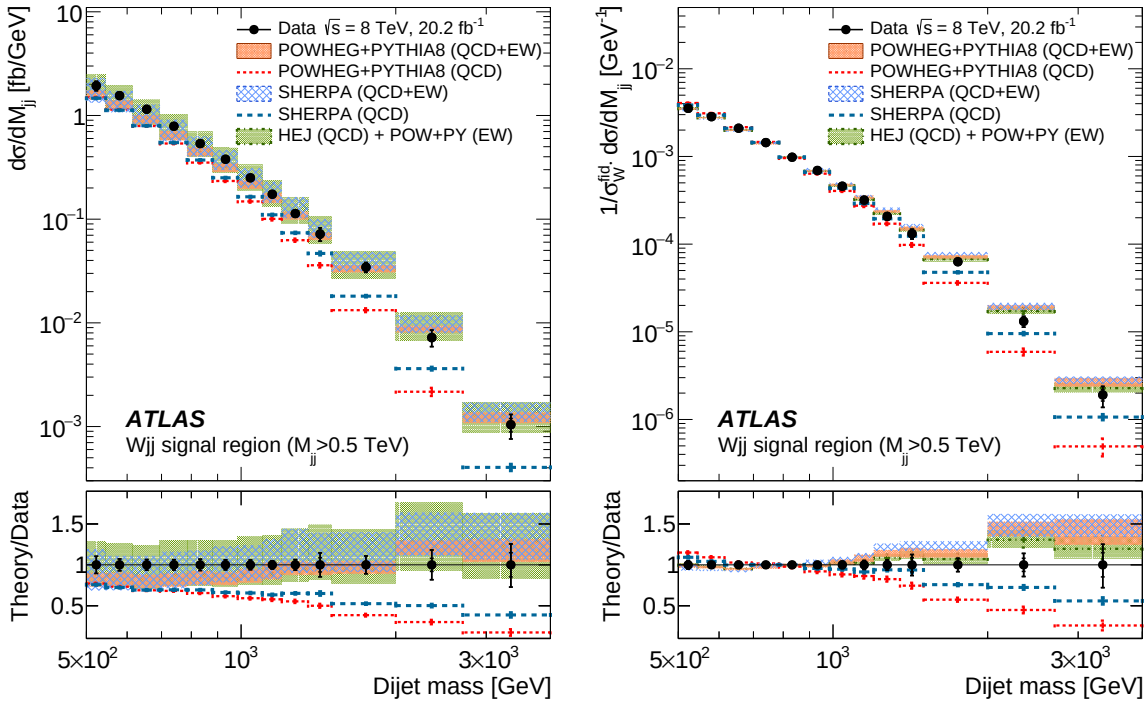

Figure 18: Unfolded absolute (left) and normalized (right) differential Wjj production cross section as a function of dijet mass for the signal fiducial region. Both statistical (inner bar) and total (outer bar) measurement uncertainties are shown, as well as ratios of the theoretical predictions to the data (the bottom panel in each distribution).

regions where strong Wjj production dominates (although there are some shape differences between data and HEJ in the forward-lepton control region).

In the signal region (Figure 18), the discrimination power between electroweak and strong Wjj predictions is enhanced, with the data supporting the presence of electroweak Wjj production. The excess of POWHEG + PYTHIA8 over data at high M_{jj} is consistent with a measured $\mu_{\mathrm{EW}} < 1$ (see Sec. 5.3).

Figure 19 shows the dijet rapidity interval distribution in the inclusive region with increasing M_{jj} thresholds that increasingly enhance the EW Wjj signal. The predictions from all generators broadly describe the data. The ratio of the POWHEG + PYTHIA8 strong Wjj prediction to the data has a positive slope, predicting smaller interval sizes than observed and demonstrating the presence of an EW Wjj signal component.

The behaviour of the EW Wjj signal as a function of the dijet rapidity interval distribution is further studied in Figure 20, which shows a clear difference between the predictions with and without the EW Wjj process. Both POWHEG + PYTHIA8 and SHERPA describe the data distribution reasonably well in these signal-enhanced regions with $M_{jj} > 0.5$ TeV and 1.0 TeV. Predictions from HEJ show shape differences with respect to the data at the $\approx 10\%$ level.

The normalized differential cross sections for Wjj production as a function of the azimuthal angle between the two leading jets are shown in the inclusive, forward-lepton control, central-jet validation, and signal fiducial regions in Figure 21. Good agreement between the data and all predictions is seen, with a slight tendency for predictions to overestimate the relative rate at small angles in all fiducial regions.

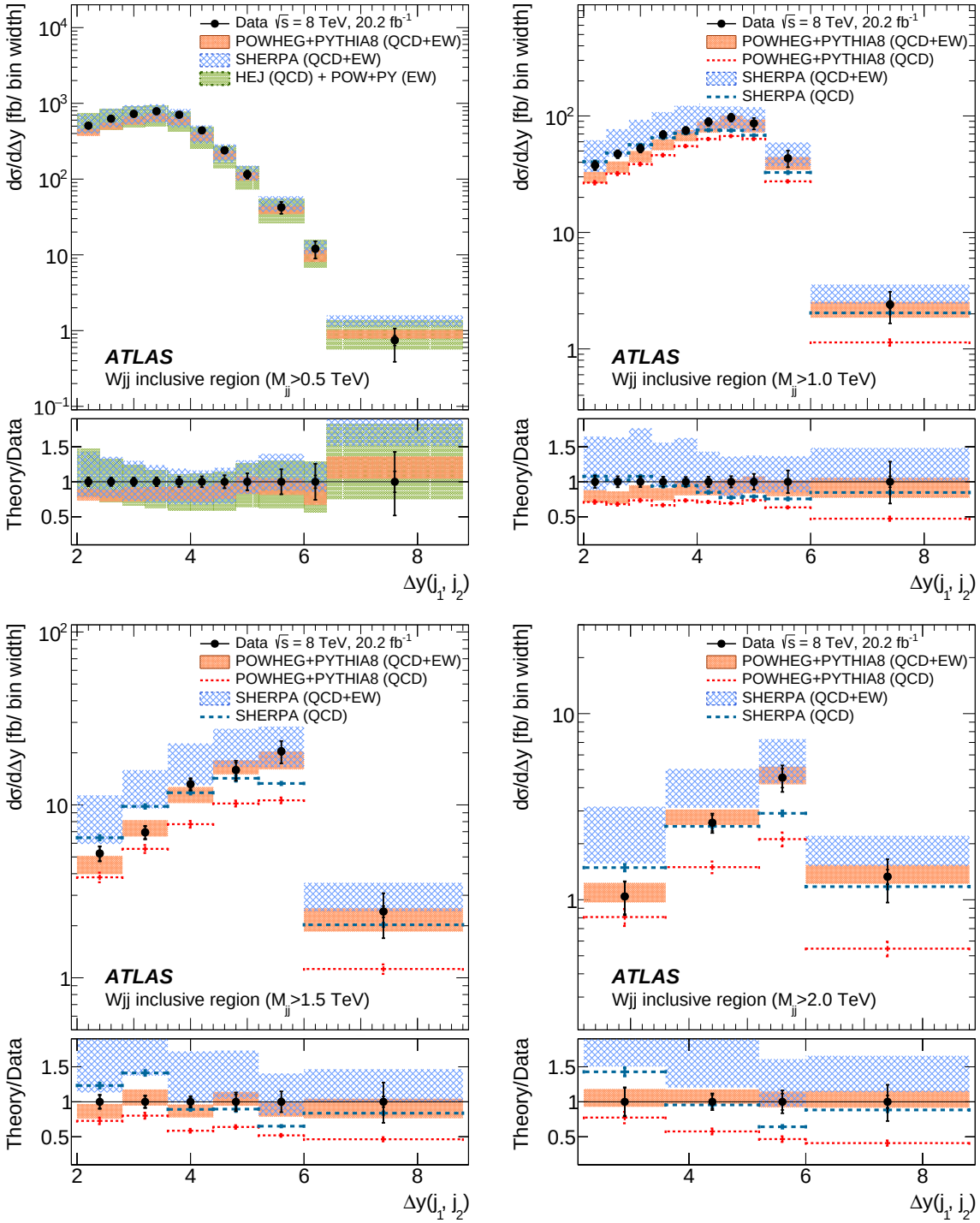

Figure 19: Unfolded absolute differential Wjj production cross sections as a function of $\Delta y(j_1, j_2)$ for the inclusive fiducial region with progressively increasing dijet mass thresholds. Both statistical (inner bar) and total (outer bar) measurement uncertainties are shown, as well as ratios of the theoretical predictions to the data (the bottom panel in each distribution).

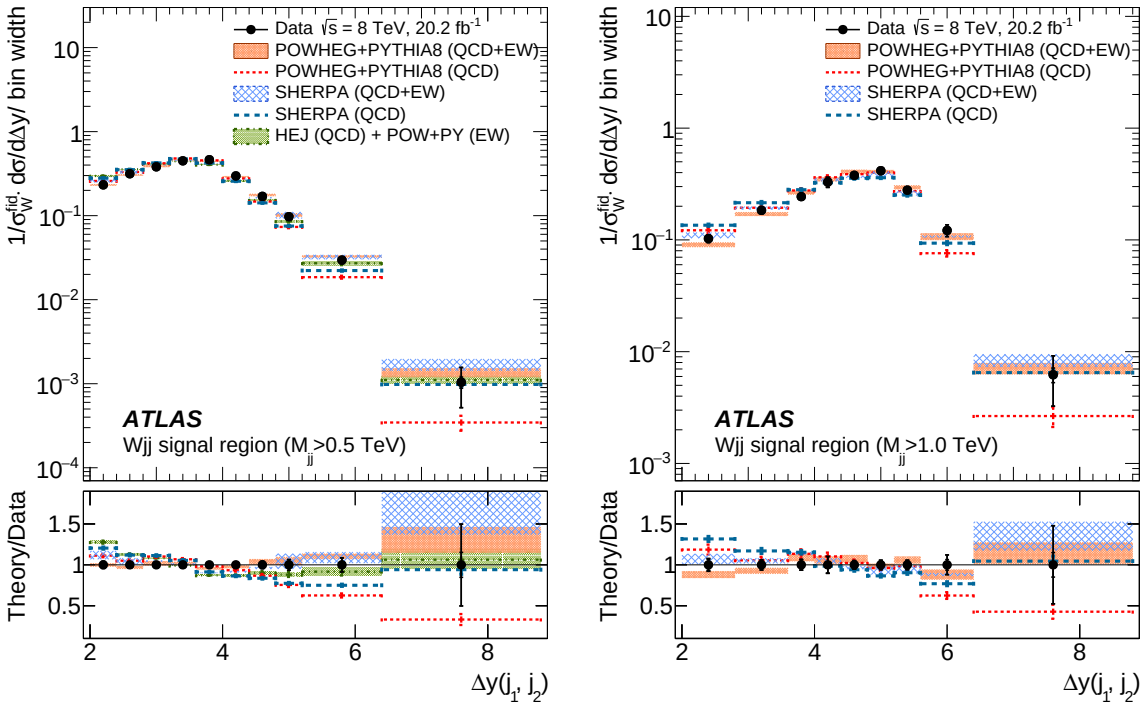

Figure 20: Unfolded normalized differential Wjj production cross sections as a function of $\Delta y(j_1, j_2)$ for the signal regions with $M_{jj} > 0.5$ TeV (left) and $M_{jj} > 1.0$ TeV (right). Both statistical (inner bar) and total (outer bar) measurement uncertainties are shown, as well as ratios of the theoretical predictions to the data (the bottom panel in each distribution).

Figure 22 shows the measured normalized p_{T} distribution of the dijet system compared to the various predictions. There is a trend for all predictions to overestimate the relative rate at high dijet p_{T} in the inclusive and signal-enhanced regions, while the central-jet validation region (shown in Appendix A) does not show such a trend. Increasing the dijet invariant mass threshold to enhance the EW Wjj signal does not increase the magnitude of the disagreement with data, suggesting that the difference is related to the modelling of the QCD Wjj production. Recent studies [66] of NLO electroweak corrections to strong Wjj production predict negative corrections to the production cross section at high W-boson and leading-jet p_{T}, offering a possible explanation for this discrepancy.

The transverse momentum distribution of the leading jet, shown in Figure 23, is globally well described by Powheg + Pythia8. Predictions from Sherpa and hej both show a harder spectrum than observed in data, with this behaviour seen in regions that are enriched in either QCD Wjj production or in EW Wjj production. Comparisons of unfolded data and theoretical predictions in the inclusive fiducial regions are shown in Appendix A (Figure 34).

6.4 Electroweak Wjj measurements

As discussed in Section 6.1, cross sections of pure electroweak Wjj production are measured in fiducial regions with high EW Wjj purity. Additional uncertainties in the modelling of strong Wjj production and the interference between the strong and electroweak Wjj processes are included, as discussed in Section 6.2. The interference uncertainty is shown explicitly as a shaded area in each bin of the measured

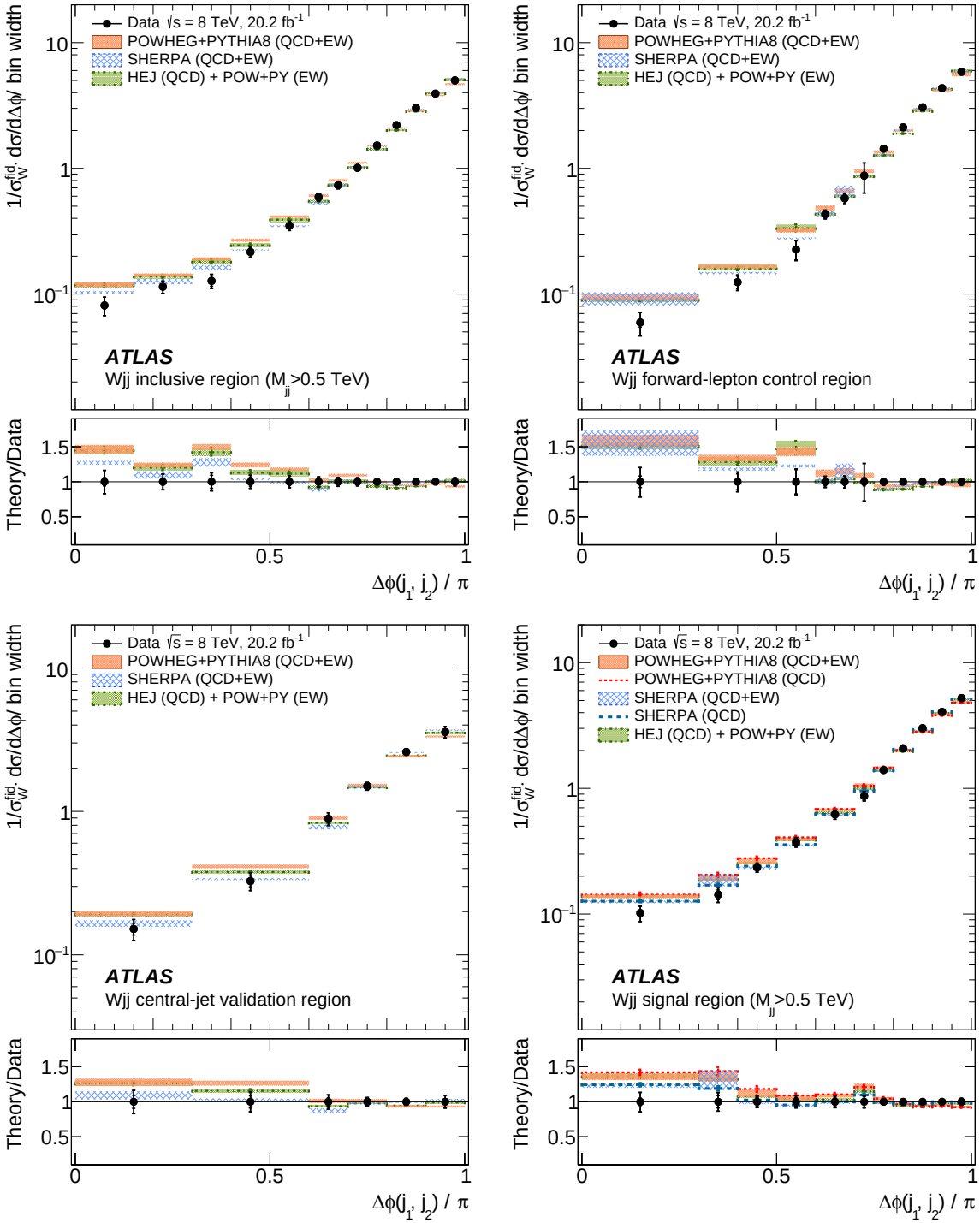

Figure 21: Unfolded normalized differential Wjj production cross sections as a function of $\Delta\phi(j_1, j_2)$ for the inclusive, forward-lepton control, central-jet validation, and signal fiducial regions. Both statistical (inner bar) and total (outer bar) measurement uncertainties are shown, as well as ratios of the theoretical predictions to the data (the bottom panel in each distribution).

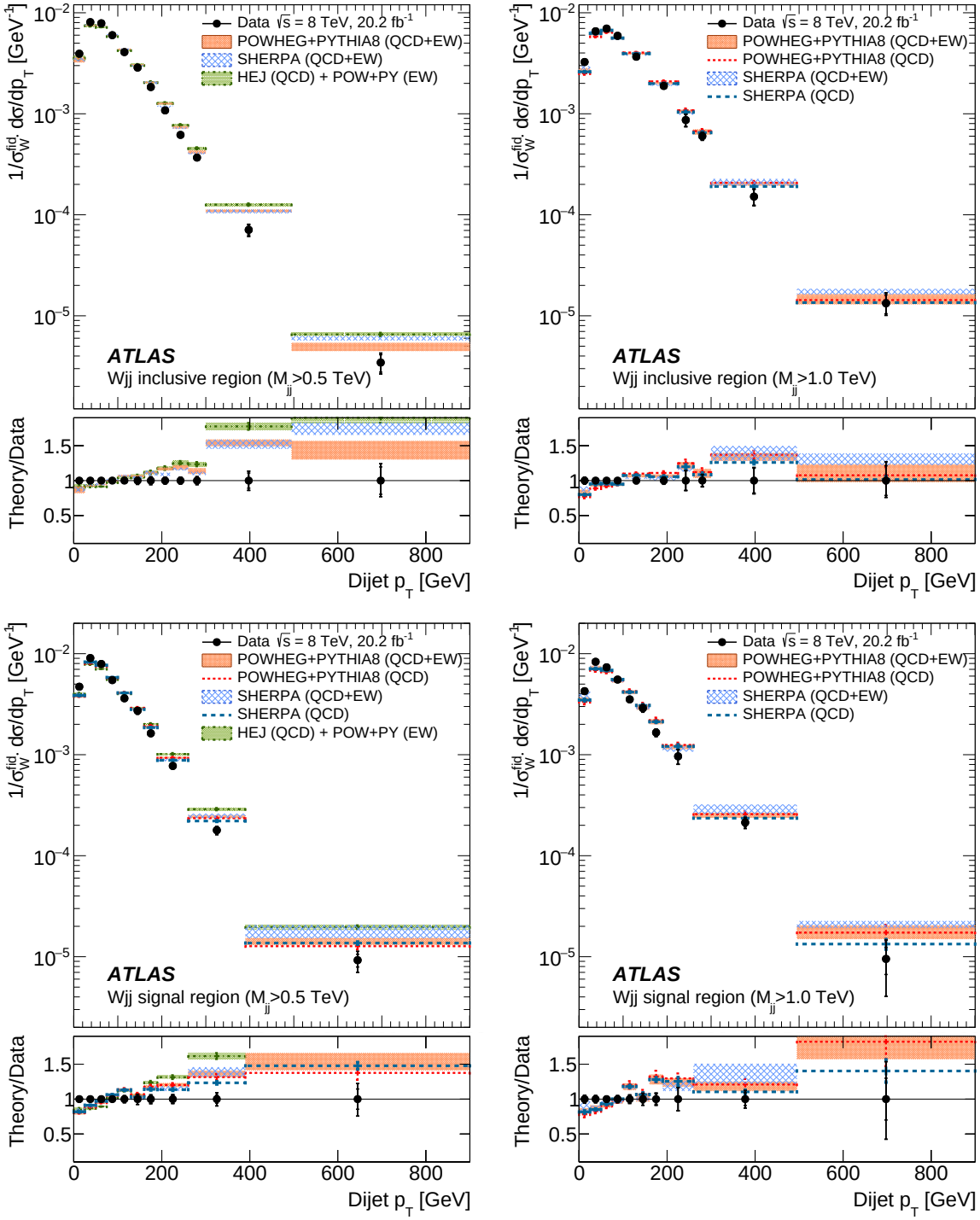

Figure 22: Unfolded normalized differential Wjj production cross sections as a function of dijet p_{T} for the inclusive (top) and signal (bottom) regions with $M_{jj} > 0.5$ TeV (left) and $M_{jj} > 1.0$ TeV (right). Both statistical (inner bar) and total (outer bar) measurement uncertainties are shown, as well as ratios of the theoretical predictions to the data (the bottom panel in each distribution).

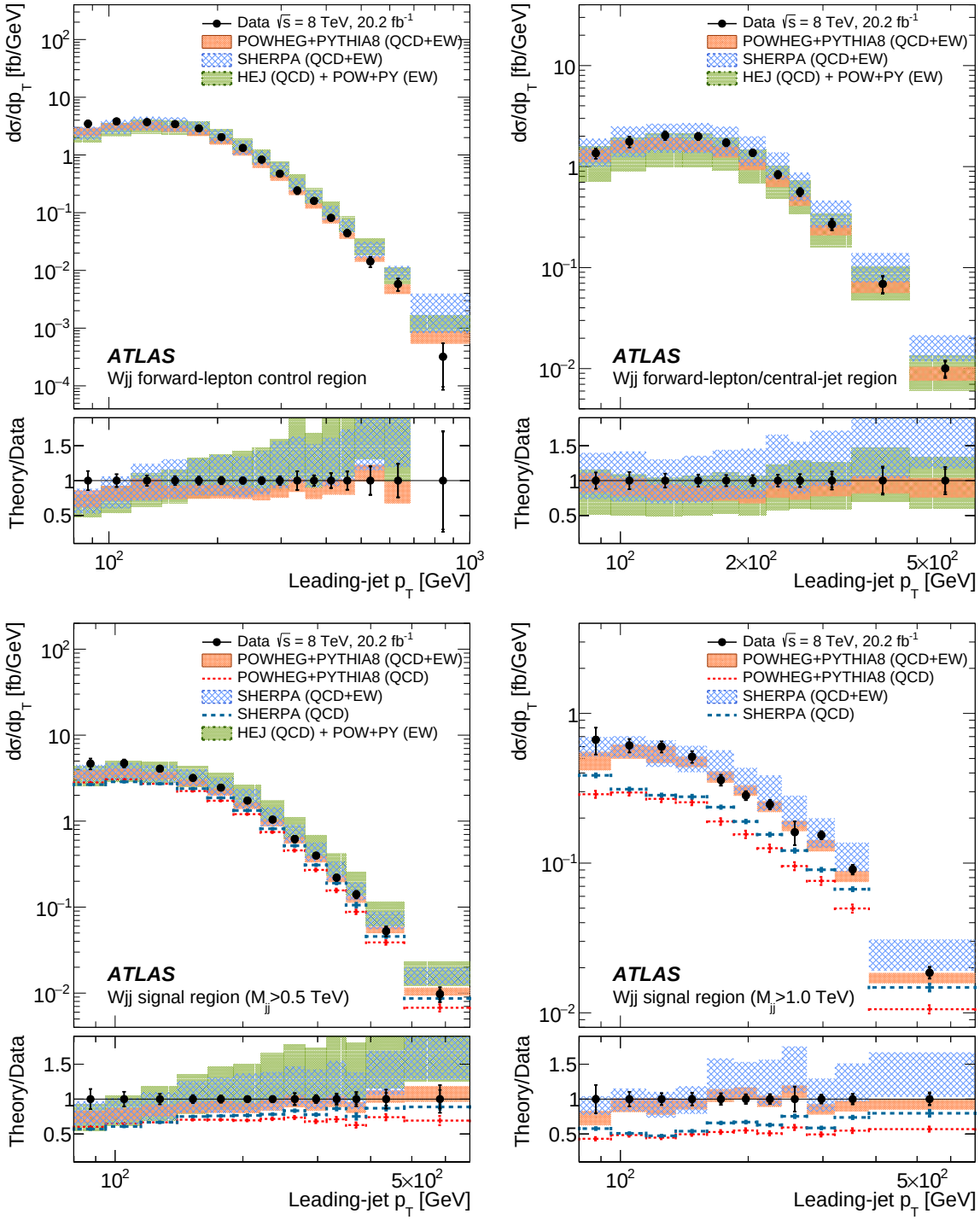

Figure 23: Unfolded absolute differential Wjj production cross sections as a function of leading-jet p_{T} for the forward-lepton control region, forward-lepton/central-jet fiducial region, and for the signal regions with $M_{jj} >$ 0.5 TeV and 1.0 TeV. Both statistical (inner bar) and total (outer bar) measurement uncertainties are shown, as well as ratios of the theoretical predictions to the data (the bottom panel in each distribution).

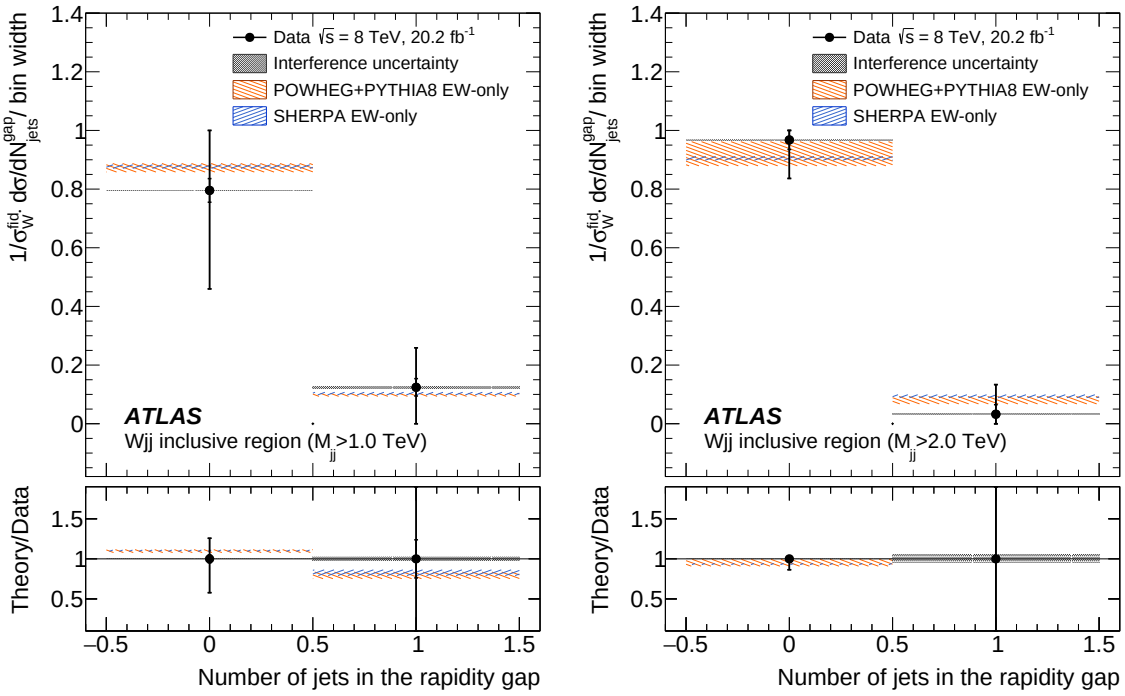

Figure 24: Unfolded normalized differential EW Wjj production cross sections as a function of the number of jets with $p_{\mathrm{T}} > 30$ GeV in the rapidity interval bounded by the two highest-p_{T} jets in the inclusive fiducial region, with $M_{jj} > 1.0$ TeV (left) and $M_{jj} > 2.0$ TeV (right). Both statistical (inner bar) and total (outer bar) measurement uncertainties are shown, as well as ratios of the theoretical predictions to the data (the bottom panel in each distribution).

distributions. Results are presented in the EW Wjj signal region defined in Table 1 and the inclusive regions with dijet mass requirements of $M_{jj} > 1.0$, 1.5, and 2.0 TeV. A subset of the measured differential results are shown here; additional distributions are tabulated in HEPDATA. Results are compared to EW Wjj predictions from SHERPA and POWHEG + PYTHIA8.

Figure 24 shows the normalized cross sections as a function of the number of jets with $p_{\mathrm{T}} > 30$ GeV emitted into the rapidity interval bounded by the two leading jets, for two dijet invariant-mass thresholds (1.0 TeV and 2.0 TeV) in the inclusive fiducial region. The measured fraction of EW Wjj events with no additional central jets is higher than that of QCD+EW Wjj events (which are shown in Figure 14). The impact of QCD–EW interference on this observable is negligible.

Figure 25 shows the normalized cross section as a function of dijet invariant mass for the inclusive and signal regions with $M_{jj} > 1.0$ TeV. This observable is used to extract the EW Wjj signal in Section 5 and is well described by the Monte Carlo simulation within uncertainties. Figure 26 shows the distribution of the rapidity interval between the two leading jets in the inclusive and signal regions with $M_{jj} > 1.0$ TeV, and for the inclusive region with invariant-mass thresholds of 1.5 and 2.0 TeV. Significant interference contributions are observed at low $\Delta y(j_1, j_2)$, where modelling uncertainties associated with the strong Wjj subtraction also limit the precision.

Figure 27 shows the normalized cross section as a function of the azimuthal angle between the two leading jets for the inclusive and signal fiducial regions with $M_{jj} > 1.0$ TeV. This observable is sensitive to the presence of anomalous CP-violating couplings [82].

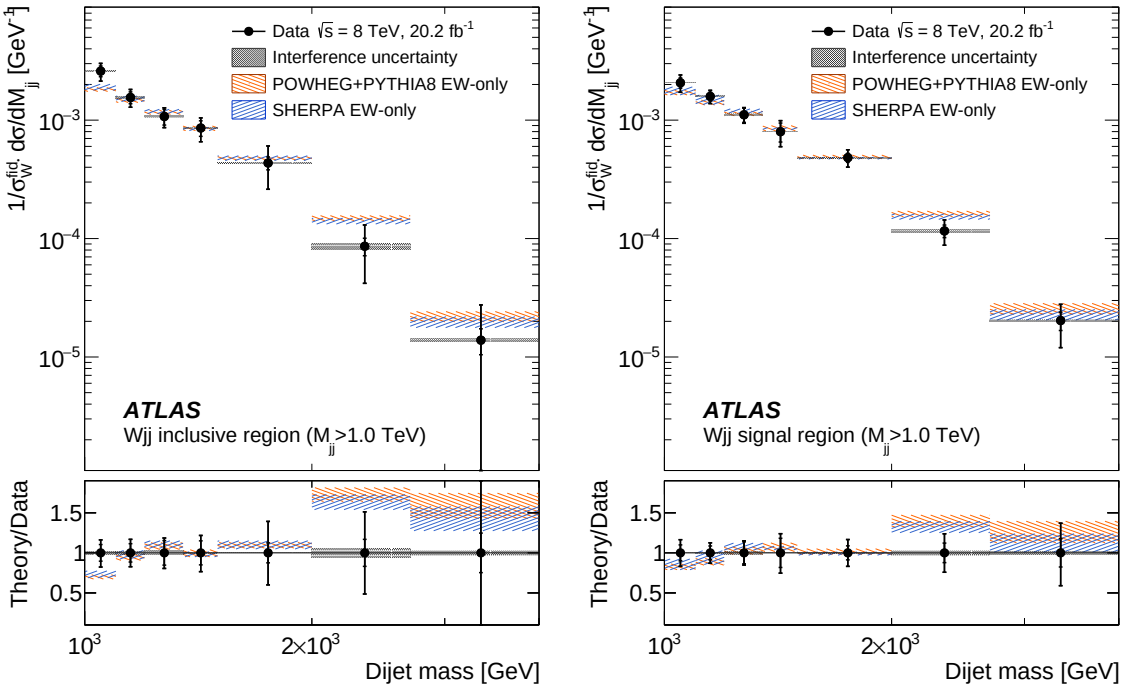

Figure 25: Unfolded normalized differential EW Wjj production cross sections as a function of the dijet invariant mass for the inclusive and signal fiducial regions with $M_{jj} > 1.0$ TeV. Both statistical (inner bar) and total (outer bar) measurement uncertainties are shown, as well as ratios of the theoretical predictions to the data (the bottom panel in each distribution).

All measured distributions in Figures 24–27 are modelled well by both Powheg + Pythia8 and Sherpa. Figure 28 shows the distribution of the normalized cross section as a function of leading-jet p_{T} in the inclusive fiducial region with $M_{jj} > 1.0$ TeV, 1.5 TeV, and 2.0 TeV, and the electroweak signal region with $M_{jj} > 1.0$ TeV. Good agreement with the predictions is seen at low dijet invariant mass; at higher masses ($M_{jj} > 1.5$ TeV) both the Powheg + Pythia8 and Sherpa predictions give a harder spectrum than observed in the data. This feature is not seen for Powheg + Pythia8 in the QCD+EW Wjj production cross sections shown in Figure 23. The overestimation of rates at high jet p_{T} may be reduced by the inclusion of NLO electroweak corrections [66].

6.5 Integrated fiducial cross sections

Integrated cross sections for Wjj production are determined in each fiducial region. Figure 29 and Table 8 show the measured integrated production cross sections times branching fractions ($\sigma^{\mathrm{fid}}_{Wjj} \times \mathcal{B}_{W\to\ell\nu}$) for QCD+EW Wjj production and, in high dijet invariant-mass regions, for EW Wjj production. Also shown is the value of the EW Wjj cross section extracted from the constrained fit described in Section 5.3. All measurements are compared to predictions from Powheg + Pythia8.

The measured data and Powheg + Pythia8 predictions are broadly compatible across all measured fiducial volumes. In fiducial regions dominated by strong Wjj production, the measured cross sections are approximately 15–20% higher than predictions. The harder M_{jj} distribution in Powheg + Pythia8 relative

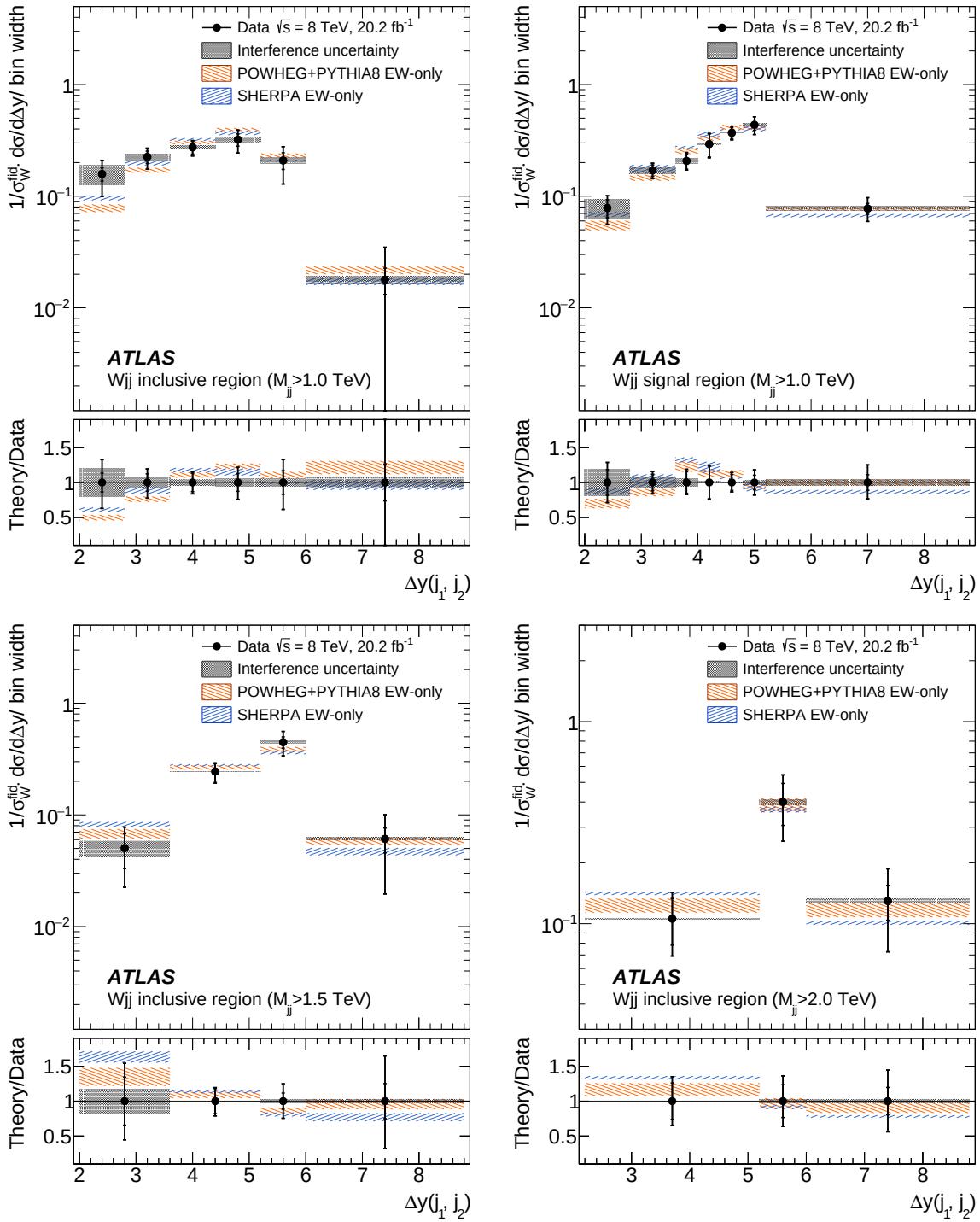

Figure 26: Unfolded normalized differential EW Wjj production cross sections as a function of $\Delta y(j_1, j_2)$ for the inclusive fiducial region with three thresholds on the dijet invariant mass, 1.0 TeV (top left), 1.5 TeV (bottom left), and 2.0 TeV (bottom right), and for the signal-enriched fiducial region with a minimum dijet invariant mass of 1.0 TeV (top right). Both statistical (inner bar) and total (outer bar) measurement uncertainties are shown, as well as ratios of the theoretical predictions to the data (the bottom panel in each distribution).

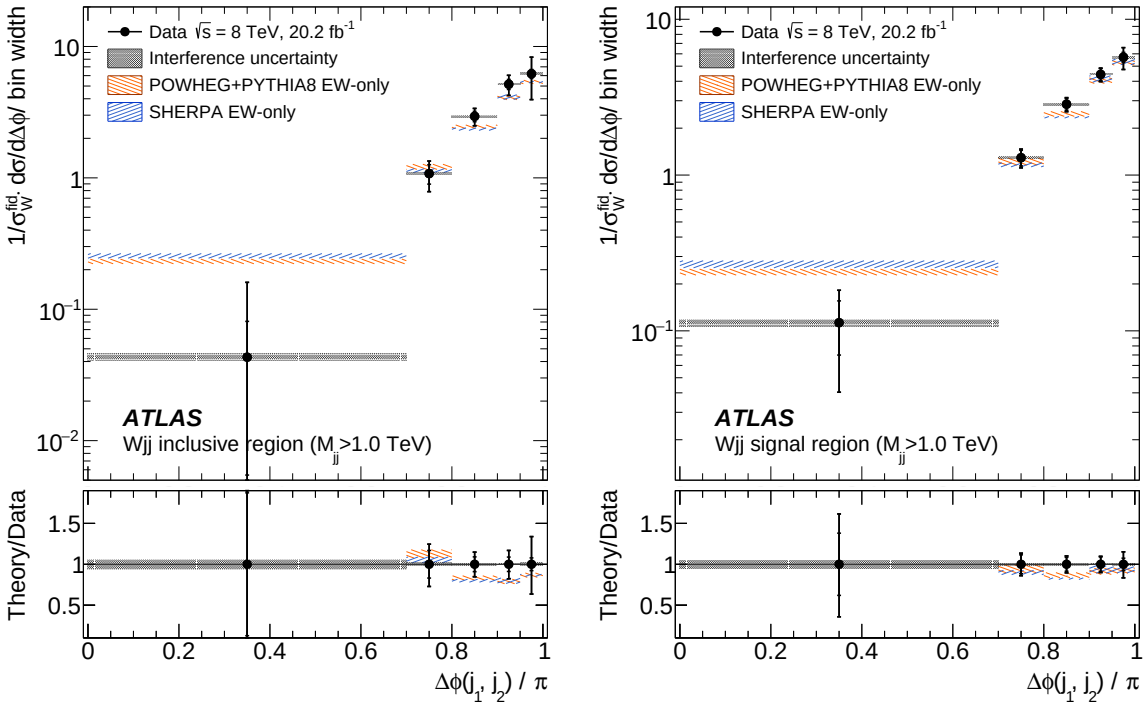

Figure 27: Unfolded normalized differential EW Wjj production cross sections as a function of the azimuthal angle between the two leading jets, for the inclusive and signal fiducial regions with $M_{jj} > 1.0$ TeV. Both statistical (inner bar) and total (outer bar) measurement uncertainties are shown, as well as ratios of the theoretical predictions to the data (the bottom panel in each distribution).

Table 8: Integrated production cross sections times branching fractions for QCD+EW Wjj production and EW Wjj production in each measured particle-level fiducial region and the equivalent prediction from Powheg + Pythia8. The uncertainties displayed are the values of the statistical and systematic uncertainties added in quadrature.

Fiducial region	$\sigma^{\text{fid}}_{Wjj} \times \mathcal{B}_{W\to\ell\nu}$ [fb]			
	QCD+EW		EW	
	Data	Powheg + Pythia8	Data	Powheg + Pythia8
Inclusive $M_{jj} > 0.5$ TeV	1700 ± 110	1420 ± 150	—	—
Inclusive $M_{jj} > 1.0$ TeV	263 ± 21	234 ± 26	64 ± 36	52 ± 1
Inclusive $M_{jj} > 1.5$ TeV	56 ± 5	53 ± 5	20 ± 8	19 ± 0.5
Inclusive $M_{jj} > 2.0$ TeV	13 ± 2	14 ± 1	5.6 ± 2.1	6.9 ± 0.2
Forward-lepton	545 ± 39	455 ± 51	—	—
Central-jet	292 ± 36	235 ± 28	—	—
Forward-lepton/central-jet	313 ± 30	265 ± 32	—	—
Signal $M_{jj} > 0.5$ TeV	546 ± 35	465 ± 39	159 ± 27	198 ± 12
Signal $M_{jj} > 1.0$ TeV	96 ± 8	89 ± 7	43 ± 11	41 ± 1

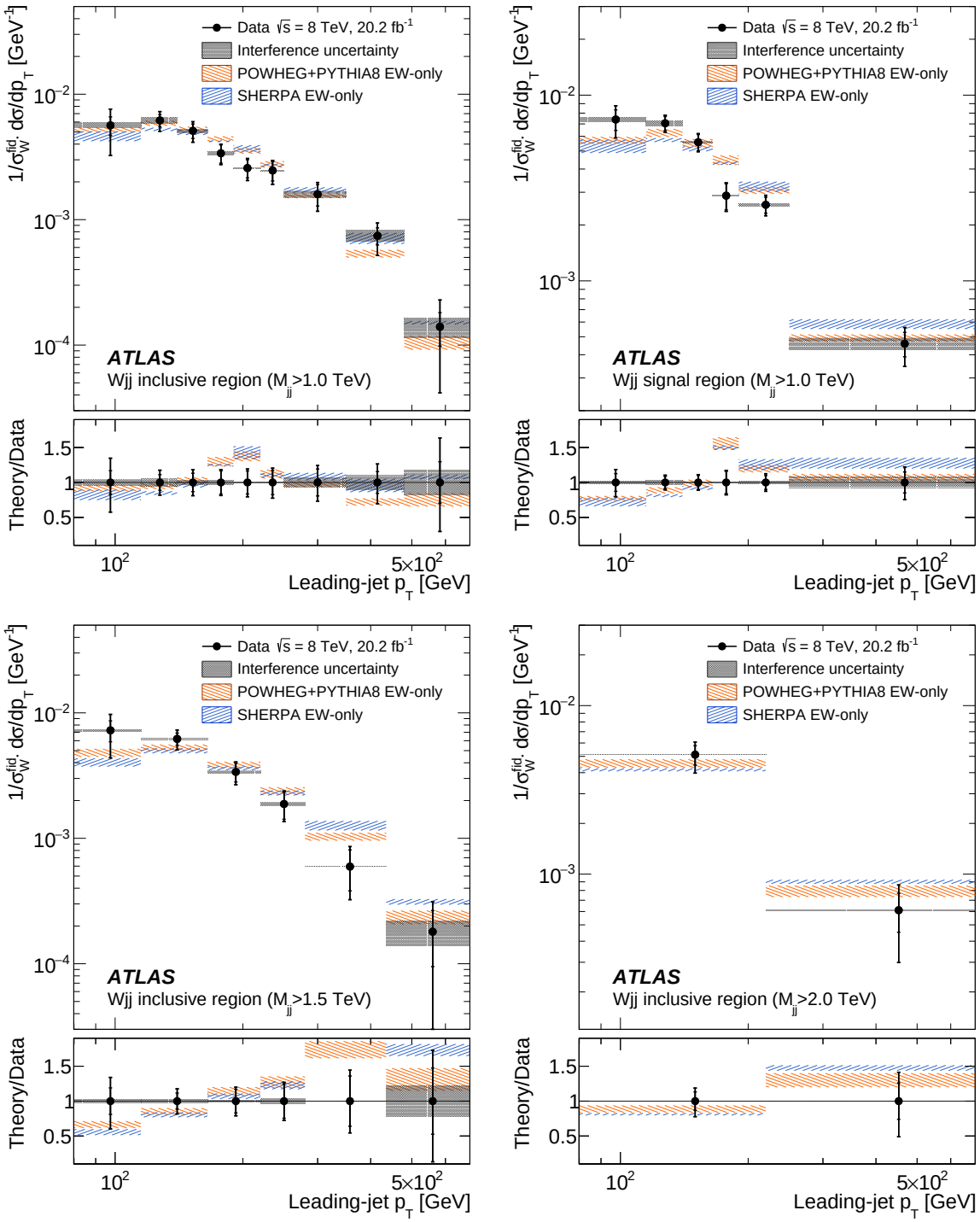

Figure 28: Unfolded normalized differential EW Wjj production cross sections as a function of the leading-jet p_{T} for the inclusive fiducial region with three thresholds on the dijet invariant mass (1.0 TeV, 1.5 TeV, and 2.0 TeV), and for the signal-enriched fiducial region with a minimum dijet invariant mass of 1.0 TeV. Both statistical (inner bar) and total (outer bar) measurement uncertainties are shown, as well as ratios of the theoretical predictions to the data (the bottom panel in each distribution).

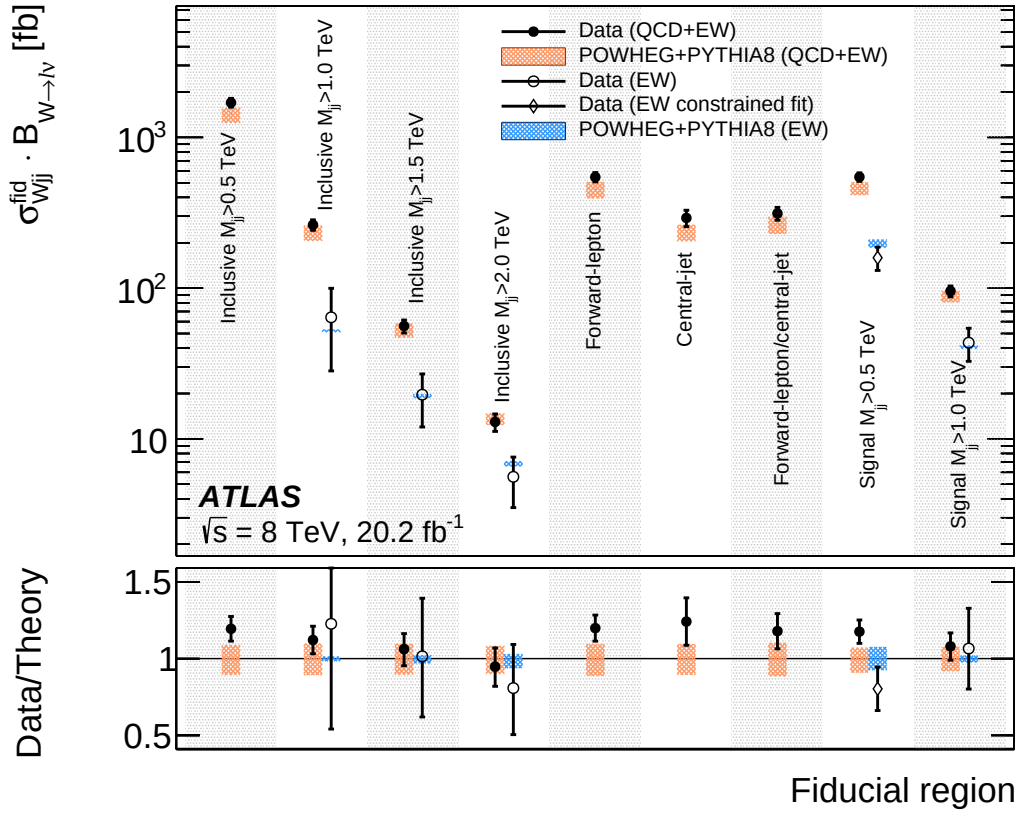

Figure 29: Integrated production cross sections times branching fractions for QCD+EW Wjj production (solid data points) and EW Wjj production (open data points) in each measured particle-level fiducial region; EW Wjj production is only measured in a subset of fiducial regions where there is sufficient purity. For each measurement the error bar represents the statistical and systematic uncertainties summed in quadrature. Comparisons are made to predictions from Powheg + Pythia8 for QCD+EW or EW Wjj production. The bottom pane shows the ratio of data to Powheg + Pythia8 predictions.

to data (Figures 16 and 18) results in a progressively decreasing ratio of measured to predicted cross sections for combined QCD+EW Wjj production. The measured EW Wjj production cross sections have larger uncertainties than the precisely constrained fiducial electroweak Wjj cross-section measurement described in Section 5.3 (also shown in Figure 29).

The measurements of electroweak Wjj fiducial cross sections are compared to measurements of electroweak Zjj production and VBF Higgs boson production in Figure 30. These other measurements are extrapolated to lower dijet mass (for Zjj production) or to inclusive production (for Higgs boson production) so their apparent cross sections are increased relative to the Wjj fiducial cross sections.

7 Anomalous triple-gauge-boson couplings

The triple-gauge-boson vertex is directly probed by the vector-boson-fusion process. Non-SM couplings at this vertex would affect the production rates and distributions. The couplings are constrained in the context of an aTGC or EFT framework, using the yield in the anomalous coupling signal region (Table 1)

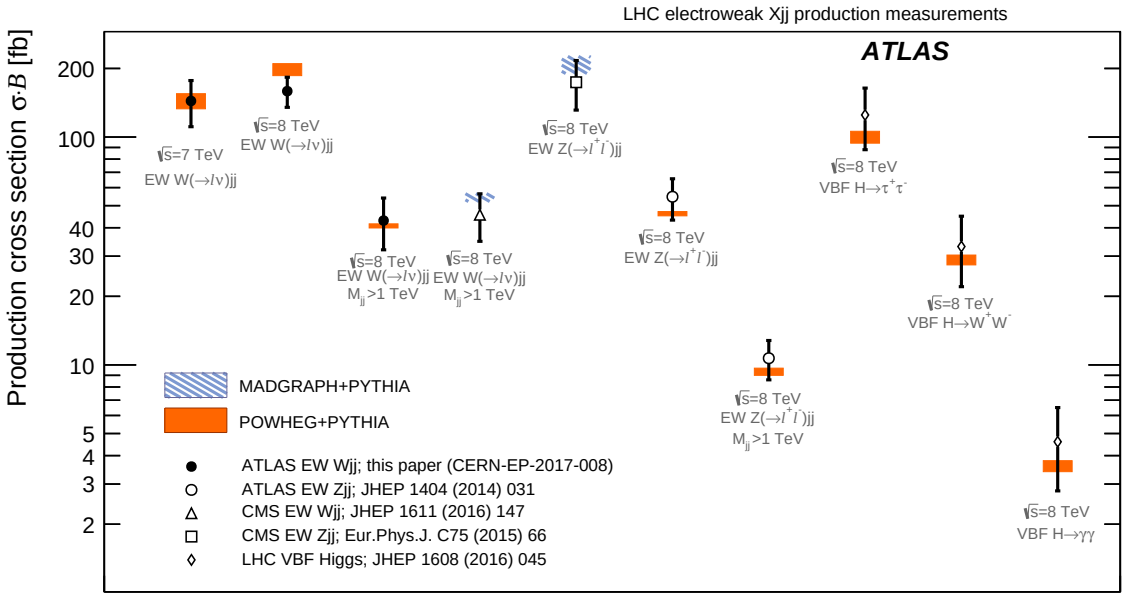

Figure 30: Measurements of the cross sections times branching fractions of electroweak production of a single W, Z, or Higgs boson with two jets at high dijet invariant mass and in fiducial measurement regions. For each measurement the error bar represents the statistical and systematic uncertainties summed in quadrature. Shaded bands represent the theory predictions. The M_{jj} threshold defining the fiducial Zjj region differs between ATLAS and CMS, leading to different inclusive cross sections.

to constrain the parameters. The results are complementary to those obtained in diboson production [83], which corresponds to the exchange of one off-shell boson in the s-channel rather than two in the t-channel.

7.1 Theoretical overview

The signal-region measurements are sensitive to the WWV ($V = Z$ or γ) couplings present in the t-channel production mode shown in Figure 1(a). These couplings can be characterized by an effective Lagrangian $\mathcal{L}_{\text{eff}}^{WWV}$ including operators up to mass-dimension six [34]:

$$i\mathcal{L}_{\text{eff}}^{WWV} = g_{WWV}\left\{\left[g_1^V V^\mu (W^-_{\mu\nu}W^{+\nu} - W^+_{\mu\nu}W^{-\nu}) + \kappa_V W^+_\mu W^-_\nu V^{\mu\nu} + \frac{\lambda_V}{m_W^2} V^{\mu\nu} W^{+\rho}_\nu W^-_{\rho\mu}\right]\right.$$
$$\left. - \left[\frac{\tilde{\kappa}_V}{2} W^-_\mu W^+_\nu \epsilon^{\mu\nu\rho\sigma} V_{\rho\sigma} + \frac{\tilde{\lambda}_V}{2m_W^2} W^-_{\rho\mu} W^{+\mu}_\nu \epsilon^{\nu\rho\alpha\beta} V_{\alpha\beta}\right]\right\},$$

where $W^\pm_{\mu\nu} = \partial_\mu W^\pm_\nu - \partial_\nu W^\pm_\mu$, with $W^\pm_\mu$ the $W^\pm$ field; $V_{\mu\nu} = \partial_\mu V_\nu - \partial_\nu V_\mu$, with V_μ the Z or γ field; m_W is the W-boson mass; and the individual couplings have SM values $g_1^V = 1$, $\kappa_V = 1$, $\lambda_V = 0$, $\tilde{\kappa}_V = 0$, and $\tilde{\lambda}_V = 0$. The overall coupling constants g_{WWV} are given by $g_{WW\gamma} = -e$ and $g_{WWZ} = -e \cdot \cot(\theta_W)$, where e is the electromagnetic coupling and θ_W is the weak mixing angle. The terms in the first row of the Lagrangian conserve C, P, and CP, while those in the second violate CP. Deviations of the g_1^V and κ_V parameters

from the SM are denoted by $\Delta g_1^Z = g_1^Z - 1$ and $\Delta\kappa_V = \kappa_V - 1$, respectively. The requirement of gauge invariance at the level of dimension-six operators leads to the following relations [84]:

$$\Delta g_1^Z = \Delta\kappa_Z + \tan^2\theta_W \Delta\kappa_\gamma, \quad \lambda_\gamma = \lambda_Z \equiv \lambda_V, \quad g_1^\gamma = 1, \quad \tilde{\kappa}_\gamma = -\cot^2\theta_W \tilde{\kappa}_Z, \quad \text{and} \quad \tilde{\lambda}_\gamma = \tilde{\lambda}_Z \equiv \tilde{\lambda}_V.$$

The presence of anomalous couplings leads to unphysically large cross sections when the square of the momentum transfer (q^2) between the incoming partons is large. To preserve unitarity, a form factor is introduced with a new-physics scale Λ that suppresses the anomalous coupling at high energies:

$$\alpha(q^2) = \frac{\alpha}{(1 + q^2/\Lambda^2)^2},$$

where α is the anomalous coupling of interest. In the following, 95% confidence-level intervals are set for a unitarization scale of $\Lambda = 4\,\text{TeV}$ and for a scale that effectively removes the form factor (shown as $\Lambda = \infty$). The scale $\Lambda = 4\,\text{TeV}$ is chosen because it does not violate unitarity for any parameter in the expected range of sensitivity.

An alternative to the use of a form factor is to restrict the couplings to the perturbative regime in an effective field theory. The EFT is an expansion in inverse powers of a scale not directly probed by the data. The additional terms at dimension six in the EFT operators take the form

$$\mathcal{L}_{\text{EFT}} = \sum_i \frac{c_i}{\Lambda^2} O_i,$$

where O_i are field operators with dimension ≤ 6, the scale of new physics is Λ, and c_i are dimensionless coefficients. The operators relevant to triple-gauge-boson couplings in the HISZ basis [84] are

$$\begin{aligned}
O_B &= (D_\mu H)^\dagger B^{\mu\nu} D_\nu H, \\
O_W &= (D_\mu H)^\dagger W^{\mu\nu} D_\nu H, \\
O_{WWW} &= \text{Tr}[W_{\mu\nu} W^\nu_\rho W^{\rho\mu}], \\
O_{\tilde{W}} &= (D_\mu H)^\dagger \tilde{W}^{\mu\nu} D_\nu H, \\
O_{\tilde{W}WW} &= \text{Tr}[W_{\mu\nu} W^\nu_\rho \tilde{W}^{\rho\mu}],
\end{aligned}$$

where H is the Higgs-boson field, $B_{\mu\nu} = \partial_\mu B_\nu - \partial_\nu B_\mu$, B^μ is the $\text{U}(1)_\text{Y}$ gauge field, and $\tilde{W}^{\mu\nu} = \frac{1}{2}\epsilon_{\mu\nu\rho\sigma} W^{\rho\sigma}$. The coefficients of these operators are related to the aTGC parameters via the following equations:

$$\begin{aligned}
\frac{c_W}{\Lambda^2} &= \frac{2}{m_Z^2}(g_1^Z - 1), \\
\frac{c_B}{\Lambda^2} &= \frac{2}{\tan^2\theta_W m_Z^2}(g_1^Z - 1) - \frac{2}{\sin^2\theta_W m_Z^2}(\kappa_Z - 1), \\
\frac{c_{WWW}}{\Lambda^2} &= \frac{2}{3g^2 m_W^2}\lambda_V, \\
\frac{c_{\tilde{W}}}{\Lambda^2} &= -\frac{2}{\tan^2\theta_W m_W^2}\tilde{\kappa}_Z, \\
\frac{c_{\tilde{W}WW}}{\Lambda^2} &= \frac{2}{3g^2 m_W^2}\tilde{\lambda}_V,
\end{aligned}$$

where g is the weak coupling, m_Z is the Z-boson mass, and the aTGC parameters do not have any form-factor suppression.

7.2 Experimental method

The signal region defined to increase the sensitivity to anomalous triple-gauge-boson couplings requires $M_{jj} > 1$ TeV and leading-jet $p_{\mathrm{T}} > 600$ GeV (Table 1). The leading-jet p_{T} is chosen because it is highly correlated with the q^2 of the signal t-channel process. The p_{T} threshold is optimized to maximize sensitivity to anomalous couplings, considering both the statistical and systematic uncertainties. The event yields in the reconstructed signal region used for setting the constraints are given in Table 4. The SM prediction is negligible for $p_{\mathrm{T}} > 1$ TeV, yielding an approximate lower bound for the validity of the EFT constraints.

The effects of anomalous couplings are modelled with Sherpa. Each sample is normalized by a factor k = NLO/LO given by the ratio of Powheg + Pythia8 to Sherpa SM predictions of electroweak Wjj production. The number of events expected for a given parameter value is calculated as:

$$N_{\mathrm{reco}} = \mathcal{L} \times \sigma \times \mathcal{B}_{W\to\ell\nu} \times \mathcal{A} \times C \times k,$$

where $\mathcal{L}$ is the integrated luminosity of the 2012 data set, $\sigma \times \mathcal{B}_{W\to\ell\nu}$ is the cross section times branching fraction for the corresponding anomalous-coupling variation, $\mathcal{A}$ is the selection acceptance at particle level, and C is the ratio of selected reconstruction-level events to the particle-level events in the fiducial phase-space region. The factor containing the cross section, branching fraction, and acceptance ($\sigma \times$ $\times\mathcal{B}_{W\to\ell\nu} \times \mathcal{A}$) is parameterized as a quadratic function of each aTGC parameter, with a 10% statistical uncertainty in the parameterization.

Theoretical uncertainties due to missing higher orders, estimated with factors of 2 and 1/2 variations of the renormalization and factorization scales, are estimated to be 8% of the strong Wjj yield and 14% of the electroweak Wjj yield in the region with leading-jet $p_{\mathrm{T}} > 600$ GeV. Detector uncertainties are correlated between strong and electroweak production and are estimated to be 11% of the combined yield.

7.3 Confidence-level intervals for aTGC parameters

Confidence-level (C.L.) intervals are calculated using a frequentist approach [85]. A negative log-likelihood function is constructed based on the expected numbers of background and signal events, and the number of observed data events. The likelihood is calculated as a function of individual aTGC parameter variations, with the other parameters set to their SM values. To obtain 95% confidence-level intervals, pseudoexperiments are produced with the number of pseudodata events drawn from a Poisson distribution, where the mean is given by the total SM prediction Gaussian-fluctuated according to theoretical and experimental uncertainties.

Tables 9 and 10 give the expected and observed 95% C.L. interval for each parameter probed, with the other parameters set to their SM values. All observed intervals are narrower than the expected intervals due to a slight deficit of data events compared with the SM prediction (Table 4). The λ_V intervals are competitive with those derived from WW production [83]. The 95% C.L. regions in planes with two parameters deviating from their SM values are shown in Figure 31. Since the regions are determined using a single measured yield, only one effective dimension is constrained. Thus, along an axis where one parameter is equal to zero, the corresponding one-parameter C.L. interval is recovered. The constraints on $\tilde{\lambda}_V$ are similar to λ_V since the sensitivity is dominated by the square of the anomalous-coupling amplitude rather than its interference with the SM amplitude.

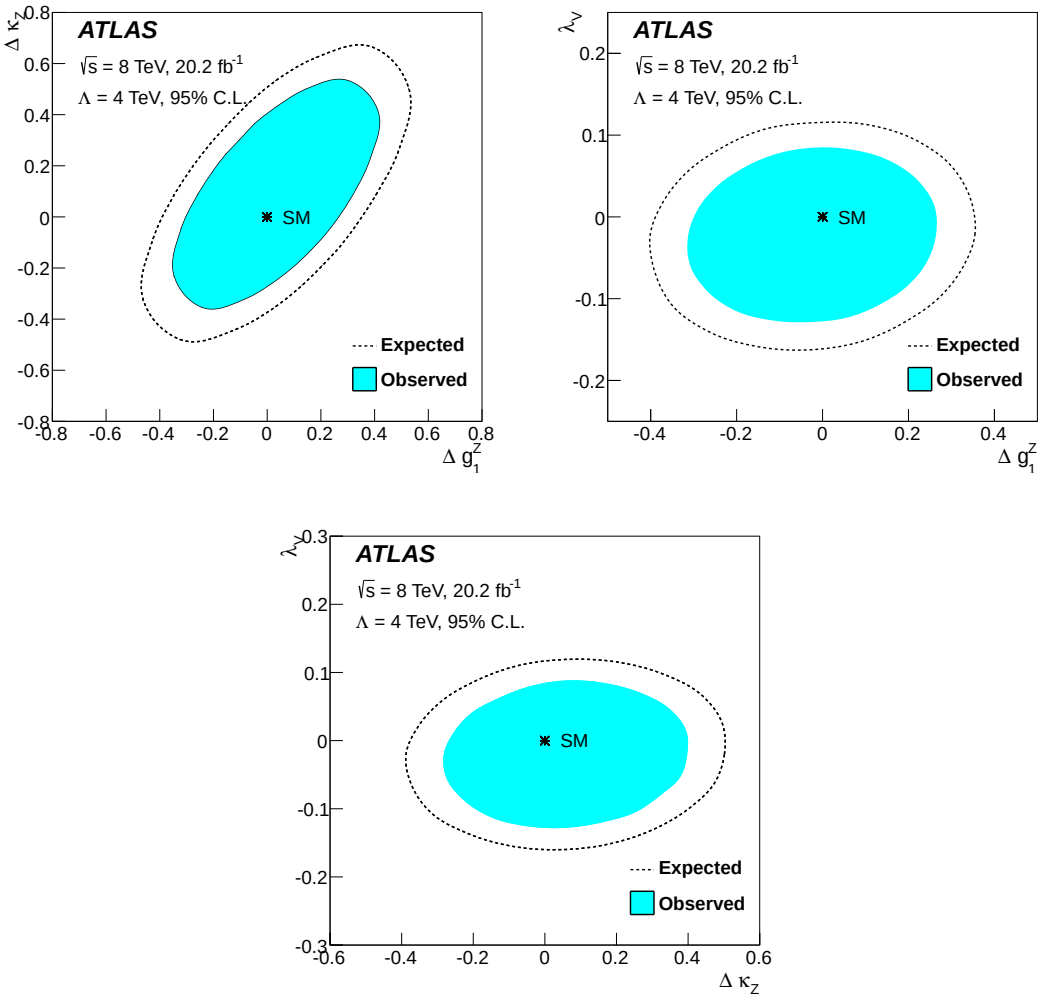

Figure 31: The observed (solid blue) and expected (open dashed) 95% C.L. allowed regions in two-parameter planes for $\Lambda = 4$ TeV. The regions are derived using a single measured yield and therefore reduce to the corresponding one-parameter interval when the other parameter is set to zero. Constraints on $\tilde{\lambda}_V$ are similar to those on λ_V.

Table 9: Expected and observed 95% C.L. allowed ranges for all aTGC parameters considered with the other parameters set to their SM values. A form factor with unitarization scale equal to 4 TeV enforces unitarity for all aTGC parameters. The results are derived from the high-q^2 region yields given in Table 4.

	$\Lambda = 4$ TeV		$\Lambda = \infty$	
	Expected	Observed	Expected	Observed
Δg_1^Z	$[-0.39, 0.35]$	$[-0.32, 0.28]$	$[-0.16, 0.15]$	$[-0.13, 0.12]$
$\Delta\kappa_Z$	$[-0.38, 0.51]$	$[-0.29, 0.42]$	$[-0.19, 0.19]$	$[-0.15, 0.16]$
λ_V	$[-0.16, 0.12]$	$[-0.13, 0.090]$	$[-0.064, 0.054]$	$[-0.053, 0.042]$
$\tilde{\kappa}_Z$	$[-1.7, 1.8]$	$[-1.4, 1.4]$	$[-0.70, 0.70]$	$[-0.56, 0.56]$
$\tilde{\lambda}_V$	$[-0.13, 0.15]$	$[-0.10, 0.12]$	$[-0.058, 0.057]$	$[-0.047, 0.046]$

Table 10: Expected and observed 95% C.L. intervals for individual EFT coefficients divided by the square of the new physics scale Λ, with other coefficients set to zero. Intervals are calculated using the high-q^2 region yields (Table 4).

Parameter	Expected [TeV^{-2}]	Observed [TeV^{-2}]
$\frac{c_W}{\Lambda^2}$	$[-39, 37]$	$[-33, 30]$
$\frac{c_B}{\Lambda^2}$	$[-200, 190]$	$[-170, 160]$
$\frac{c_{WWW}}{\Lambda^2}$	$[-16, 13]$	$[-13, 9]$
$\frac{c_{\tilde{W}}}{\Lambda^2}$	$[-720, 720]$	$[-580, 580]$
$\frac{c_{\tilde{W}WW}}{\Lambda^2}$	$[-14, 14]$	$[-11, 11]$

8 Summary

Measurements of the fiducial and differential cross sections of electroweak production of W bosons in association with two jets have been performed using the lepton decay channel and events with high dijet invariant mass. The measurements use data collected by the ATLAS detector from proton–proton collisions at the LHC at centre-of-mass energies of $\sqrt{s} = 7$ and 8 TeV, corresponding to 4.7 and 20.2 fb^{-1} of integrated luminosity, respectively. The cross sections in a fiducial region with a signal purity of $O(15\%)$ are

$$\begin{aligned}\sigma^{\text{fid}}_{\text{EW } W(\to\ell\nu)jj}\,(7\text{ TeV}) &= 144 \pm 23\ (\text{stat})\ \pm 23\ (\text{exp})\ \pm 13\ (\text{th})\ \text{fb},\\ \sigma^{\text{fid}}_{\text{EW } W(\to\ell\nu)jj}\,(8\text{ TeV}) &= 159 \pm 10\ (\text{stat})\ \pm 17\ (\text{exp})\ \pm 20\ (\text{th})\ \text{fb},\end{aligned}$$

corresponding to a deviation of $< 0.1\sigma$ (1.3σ) from the SM prediction of 144 ± 11 (198 ± 12) fb at $\sqrt{s} = 7$ (8) TeV. The large sample size of the 8 TeV measurement yields the smallest relative uncertainty of existing fiducial cross-section measurements of electroweak boson production in a VBF topology.

Differential cross sections of the $\sqrt{s} = 8$ TeV electroweak Wjj production process are measured in a high-purity region with $M_{jj} > 1$ TeV. The cross sections are measured as a function of dijet mass, dijet rapidity separation, dijet azimuthal angular separation, dijet p_{T}, leading-jet p_{T}, the number of jets within the dijet rapidity gap, and lepton and jet centralities. Additionally, differential cross sections are measured in various fiducial regions for the combined electroweak and strong Wjj production with high dijet invariant mass. The differential measurements are integrated in each fiducial region to obtain additional fiducial cross-section measurements. The most inclusive region, where $M_{jj} > 0.5$ TeV, $\Delta y(j_1, j_2) > 2$, $p_{\mathrm{T}}^{j_1} > 80$ GeV, and $p_{\mathrm{T}}^{j_2} > 60$ GeV, has a measured QCD+EW fiducial cross section at $\sqrt{s} = 8$ TeV of $\sigma^{\mathrm{fid}}_{\mathrm{QCD+EW}\ W(\to \ell\nu)jj} = 1700 \pm 110$ fb.

The region of increased purity for electroweak production of Wjj ($M_{jj} > 1$ TeV) is used to constrain dimension-six triple-gauge-boson operators motivated by an effective field theory. To improve the sensitivity to high-scale physics affecting the triple-gauge-boson vertex, events with leading-jet $p_{\mathrm{T}} > 600$ GeV are also used to constrain CP-conserving and CP-violating operators in the HISZ scenario, both with and without a form-factor suppression. A 95% C.L. range of $[-0.13, 0.09]$ is determined for λ_V with a suppression scale of 4 TeV and the other parameters set to their SM values. Limits are also set on the parameters of an effective field theory. The operator coefficient c_{WWW}/Λ^2 is proportional to λ_V and is constrained to $[-13, 9]/\mathrm{TeV}^2$ at 95% C.L. Constraints on CP-violating operators are similar to those on the CP-conserving operators.

Acknowledgements

We thank CERN for the very successful operation of the LHC, as well as the support staff from our institutions without whom ATLAS could not be operated efficiently.

We acknowledge the support of ANPCyT, Argentina; YerPhI, Armenia; ARC, Australia; BMWFW and FWF, Austria; ANAS, Azerbaijan; SSTC, Belarus; CNPq and FAPESP, Brazil; NSERC, NRC and CFI, Canada; CERN; CONICYT, Chile; CAS, MOST and NSFC, China; COLCIENCIAS, Colombia; MSMT CR, MPO CR and VSC CR, Czech Republic; DNRF and DNSRC, Denmark; IN2P3-CNRS, CEA-DSM/IRFU, France; SRNSF, Georgia; BMBF, HGF, and MPG, Germany; GSRT, Greece; RGC, Hong Kong SAR, China; ISF, I-CORE and Benoziyo Center, Israel; INFN, Italy; MEXT and JSPS, Japan; CNRST, Morocco; NWO, Netherlands; RCN, Norway; MNiSW and NCN, Poland; FCT, Portugal; MNE/IFA, Romania; MES of Russia and NRC KI, Russian Federation; JINR; MESTD, Serbia; MSSR, Slovakia; ARRS and MIZŠ, Slovenia; DST/NRF, South Africa; MINECO, Spain; SRC and Wallenberg Foundation, Sweden; SERI, SNSF and Cantons of Bern and Geneva, Switzerland; MOST, Taiwan; TAEK, Turkey; STFC, United Kingdom; DOE and NSF, United States of America. In addition, individual groups and members have received support from BCKDF, the Canada Council, CANARIE, CRC, Compute Canada, FQRNT, and the Ontario Innovation Trust, Canada; EPLANET, ERC, ERDF, FP7, Horizon 2020 and Marie Skłodowska-Curie Actions, European Union; Investissements d'Avenir Labex and Idex, ANR, Région Auvergne and Fondation Partager le Savoir, France; DFG and AvH Foundation, Germany; Herakleitos, Thales and Aristeia programmes co-financed by EU-ESF and the Greek NSRF; BSF, GIF and Minerva, Israel; BRF, Norway; CERCA Programme Generalitat de Catalunya, Generalitat Valenciana, Spain; the Royal Society and Leverhulme Trust, United Kingdom.

The crucial computing support from all WLCG partners is acknowledged gratefully, in particular from CERN, the ATLAS Tier-1 facilities at TRIUMF (Canada), NDGF (Denmark, Norway, Sweden), CC-IN2P3 (France), KIT/GridKA (Germany), INFN-CNAF (Italy), NL-T1 (Netherlands), PIC (Spain), ASGC

(Taiwan), RAL (UK) and BNL (USA), the Tier-2 facilities worldwide and large non-WLCG resource providers. Major contributors of computing resources are listed in Ref. [86].

A Appendix

This section includes normalized and absolute differential QCD+EW Wjj (Figures 32–52) and EW Wjj (Figures 53–58) production cross-section measurements not directly discussed in the main text. The complete set of measured differential spectra is available in HEPDATA [77].

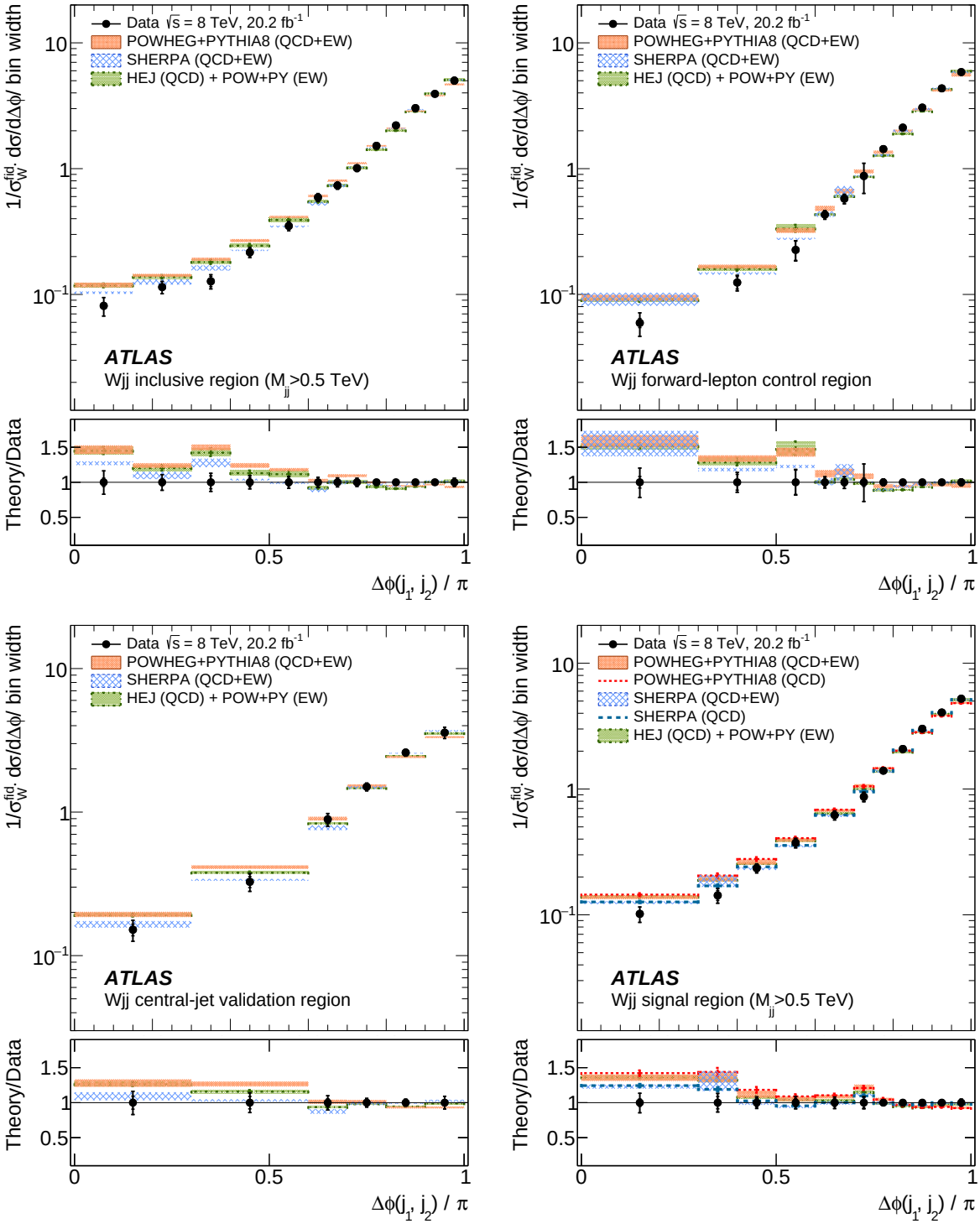

Figure 32: Unfolded normalized differential production cross sections as a function of $\Delta\phi(j_1, j_2)$ for the inclusive, forward-lepton control, central-jet validation, and signal fiducial regions. Both statistical (inner bar) and total (outer bar) measurement uncertainties are shown, as well as ratios of the theoretical predictions to the data (the bottom panel in each distribution).

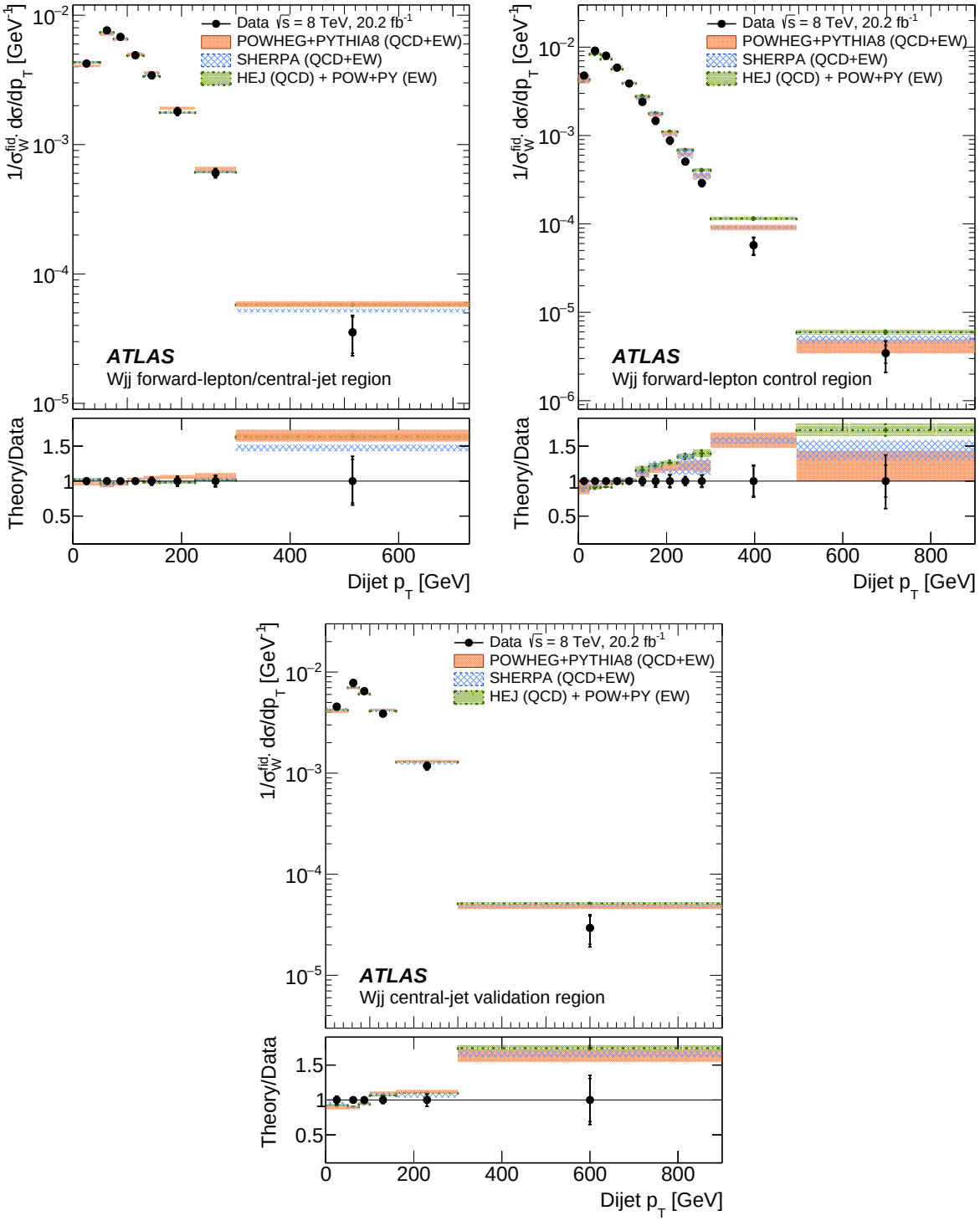

Figure 33: Unfolded normalized differential $W\,j\,j$ production cross sections as a function of dijet p_{T} in the forward-lepton/central-jet, forward-lepton, and central-jet fiducial regions. Both statistical (inner bar) and total (outer bar) measurement uncertainties are shown, as well as ratios of the theoretical predictions to the data (the bottom panel in each distribution).

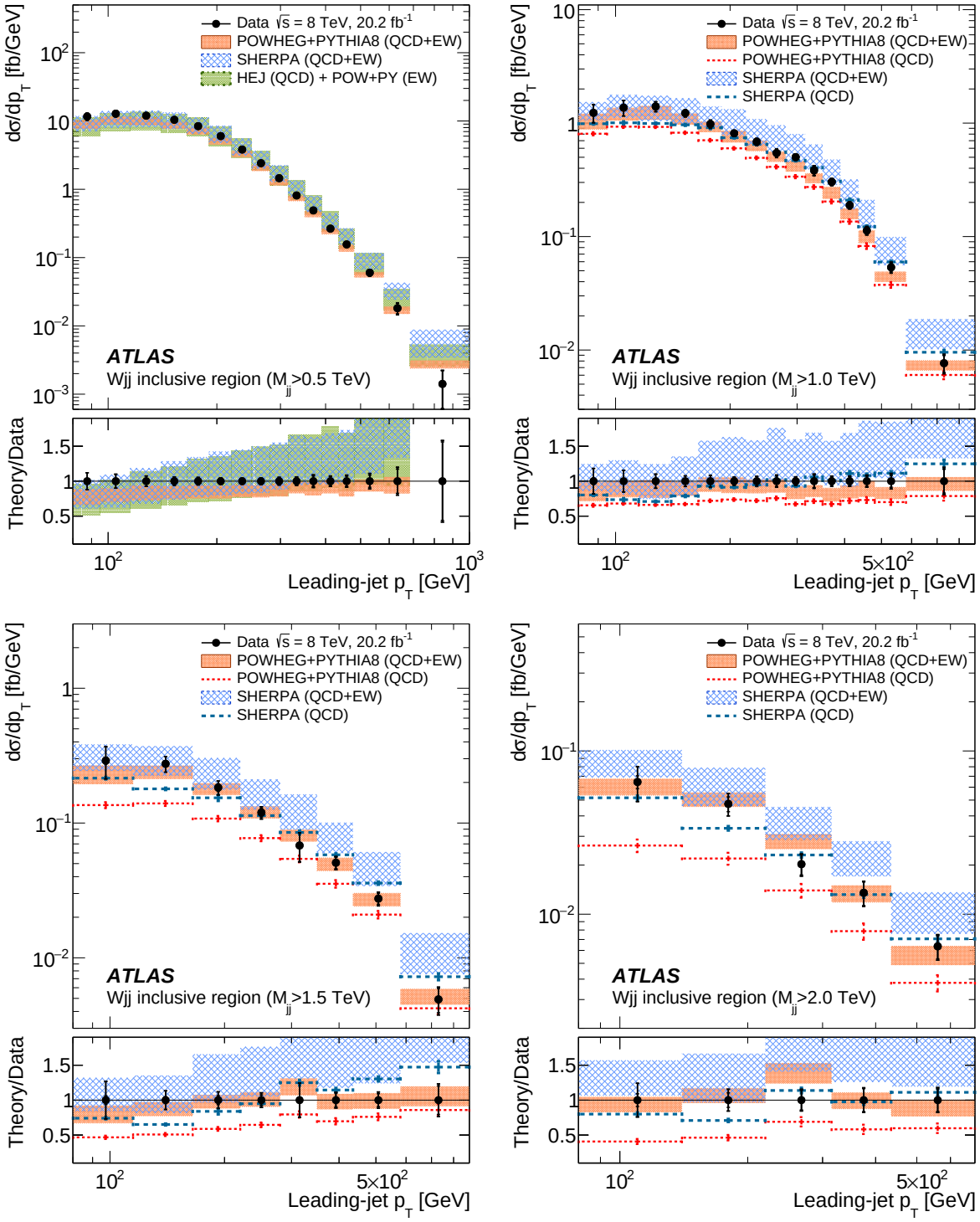

Figure 34: Unfolded absolute differential Wjj production cross sections as a function of leading-jet p_{T} for the inclusive fiducial region when the dijet invariant mass threshold is progressively raised in 500 GeV increments from 0.5 TeV (top left) to 2.0 TeV (bottom right). Both statistical (inner bar) and total (outer bar) measurement uncertainties are shown, as well as ratios of the theoretical predictions to the data (the bottom panel in each distribution).

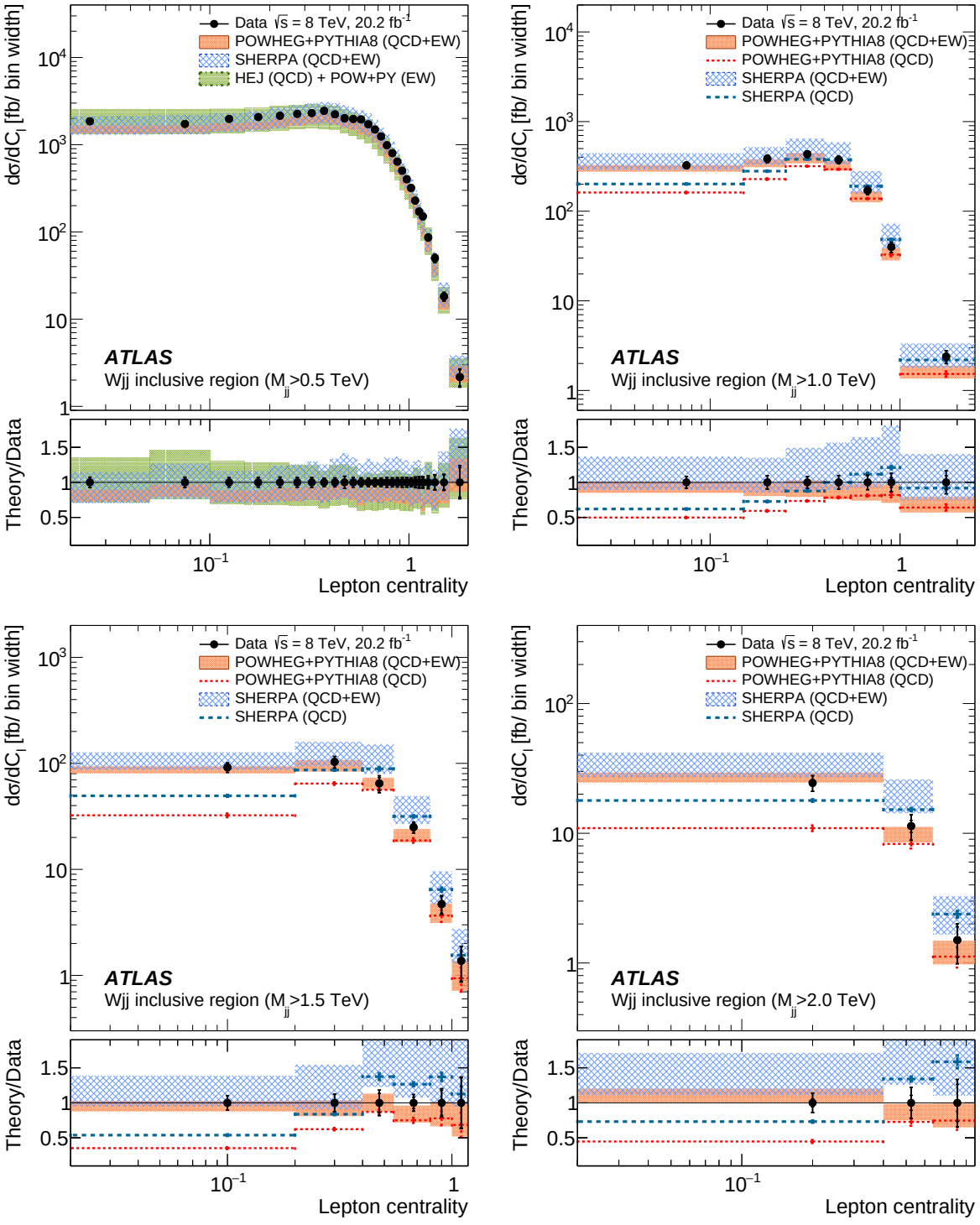

Figure 35: Unfolded differential Wjj production cross sections as a function of lepton centrality in the inclusive fiducial region with four thresholds on the dijet invariant mass (0.5 TeV, 1.0 TeV, 1.5 TeV, and 2.0 TeV). Both statistical (inner bar) and total (outer bar) measurement uncertainties are shown, as well as ratios of the theoretical predictions to the data (the bottom panel in each distribution).

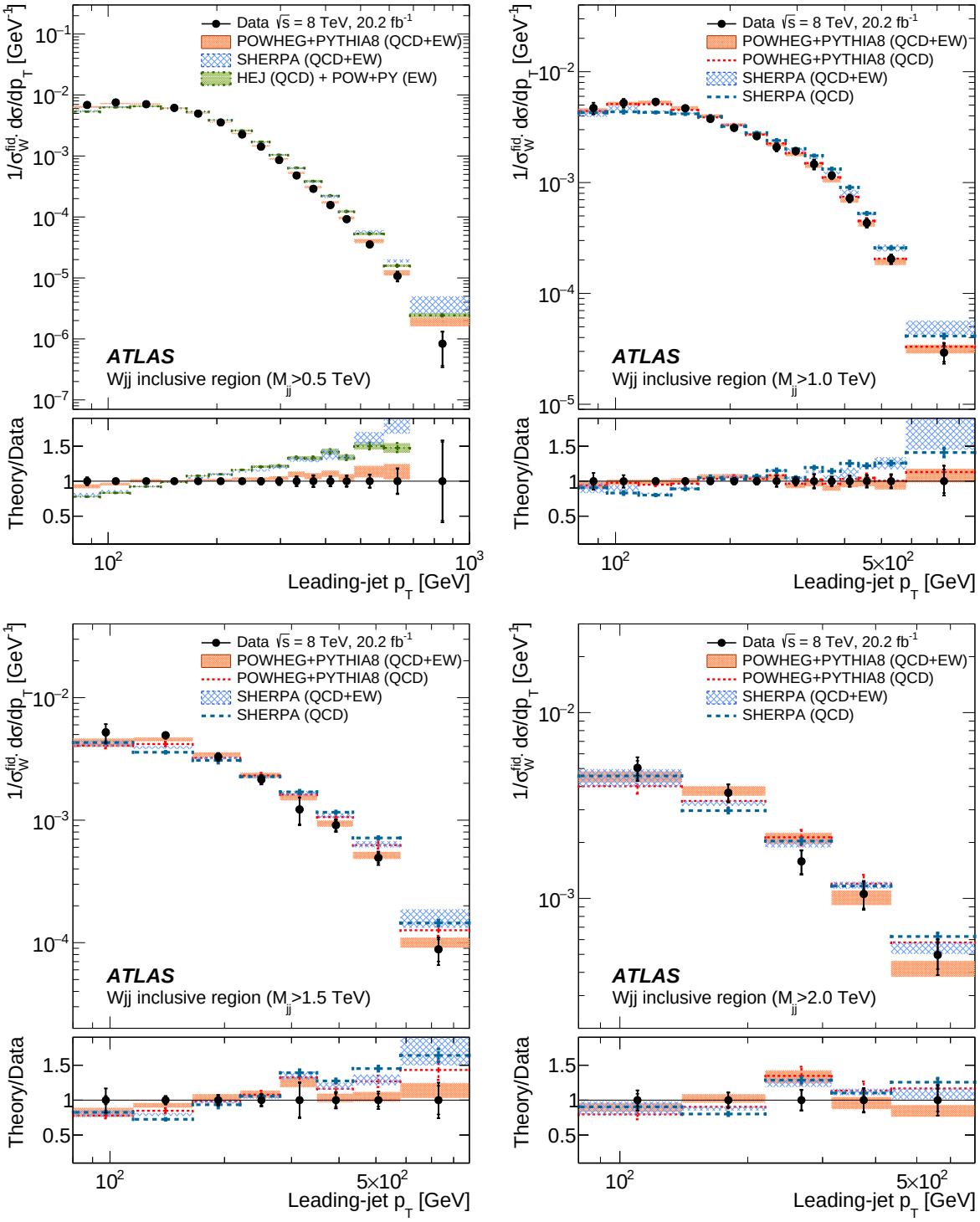

Figure 36: Unfolded normalized differential Wjj production cross sections as a function of the leading-jet p_{T} in the inclusive fiducial region with four thresholds on the dijet invariant mass (0.5 TeV, 1.0 TeV, 1.5 TeV, and 2.0 TeV). Both statistical (inner bar) and total (outer bar) measurement uncertainties are shown, as well as ratios of the theoretical predictions to the data (the bottom panel in each distribution).

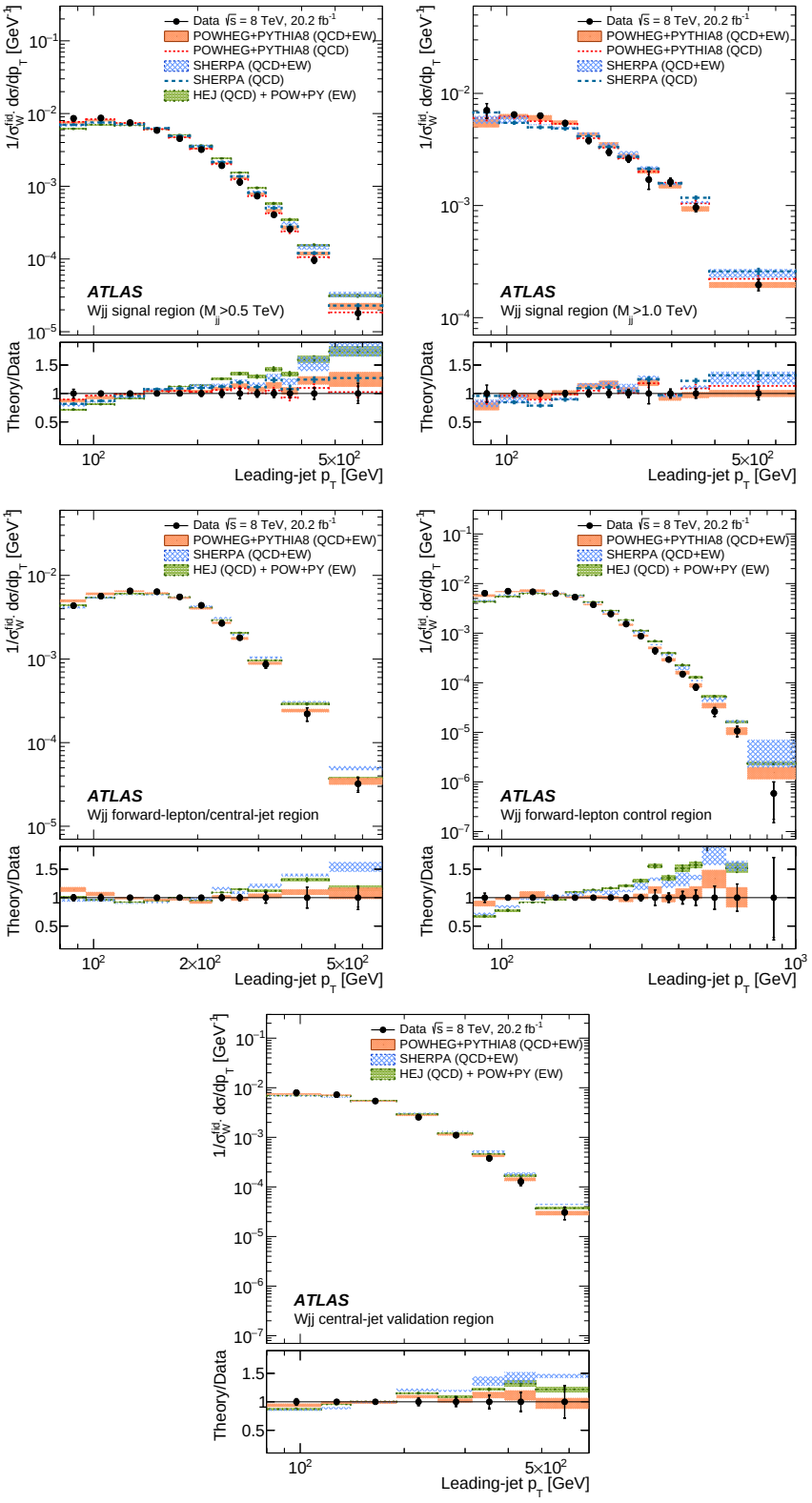

Figure 37: Unfolded normalized differential Wjj production cross sections as a function of the leading-jet p_{T} in the signal, high-mass signal, forward-lepton/central-jet, forward-lepton, and central-jet fiducial regions. Both statistical (inner bar) and total (outer bar) measurement uncertainties are shown, as well as ratios of the theoretical predictions to the data (the bottom panel in each distribution).

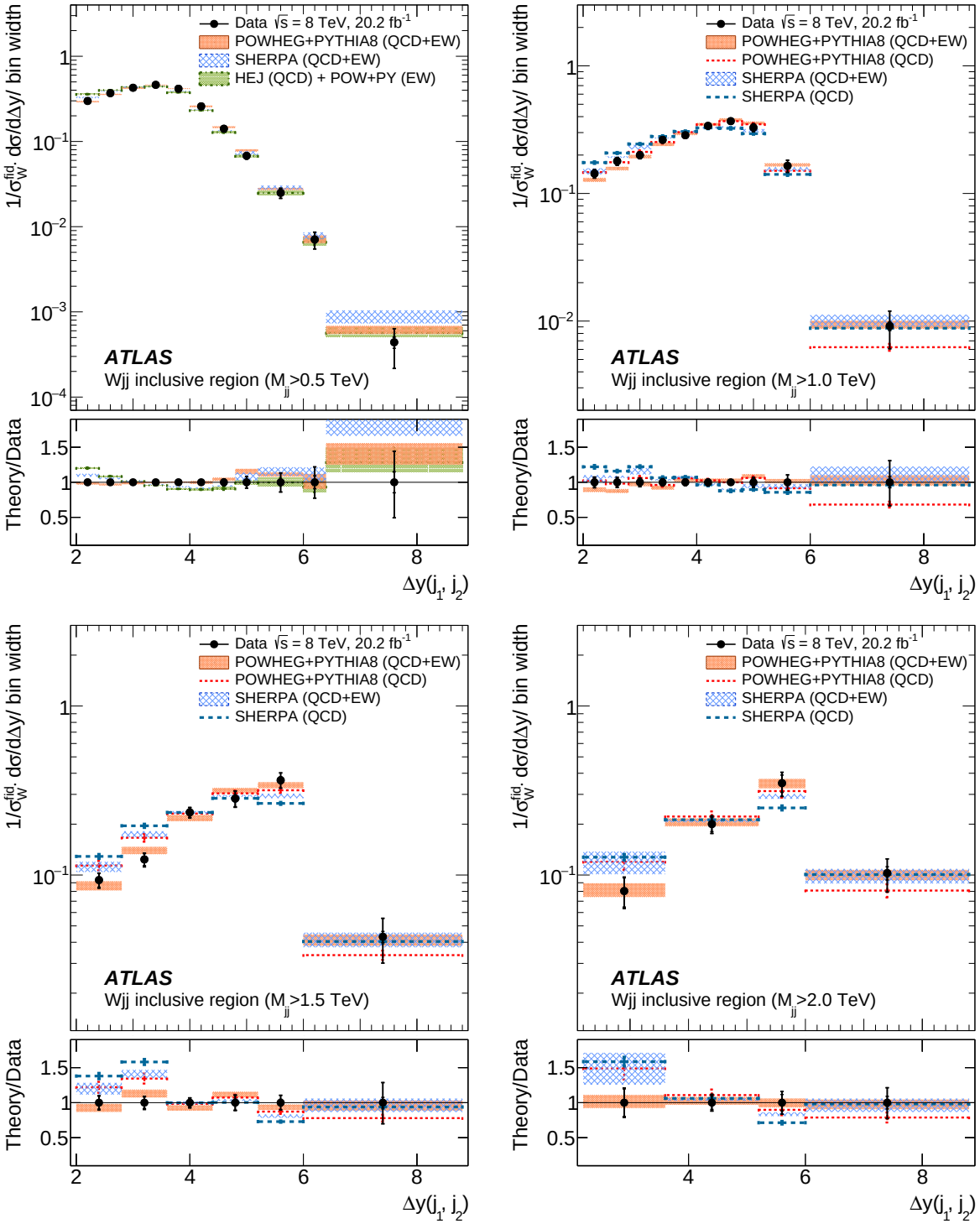

Figure 38: Unfolded normalized differential Wjj production cross sections as a function of $\Delta y(j_1, j_2)$ in the inclusive fiducial region with four thresholds on the dijet invariant mass (0.5 TeV, 1.0 TeV, 1.5 TeV, and 2.0 TeV). Both statistical (inner bar) and total (outer bar) measurement uncertainties are shown, as well as ratios of the theoretical predictions to the data (the bottom panel in each distribution).

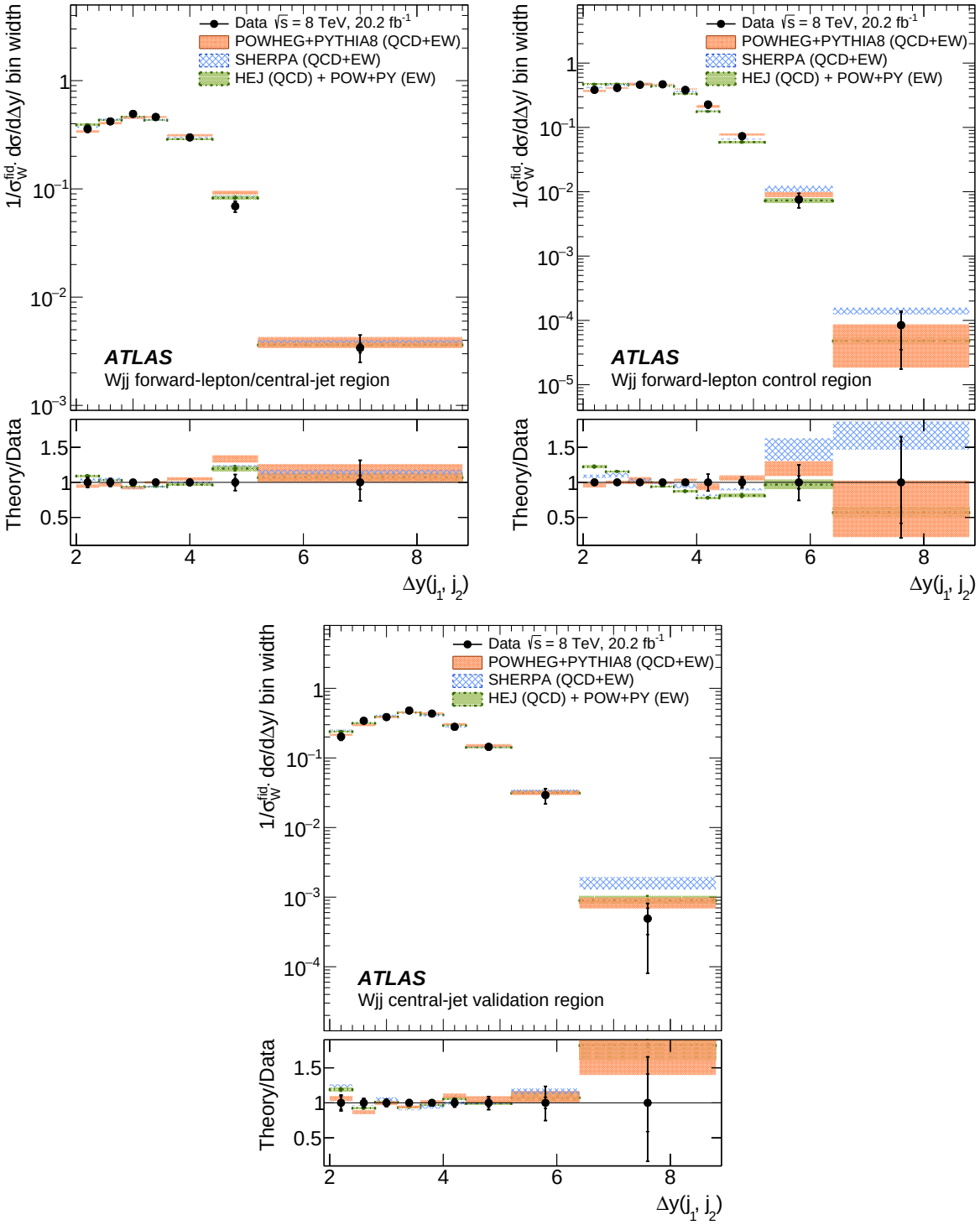

Figure 39: Unfolded normalized differential Wjj production cross sections as a function of $\Delta y(j_1, j_2)$ in the forward-lepton/central-jet, forward-lepton, and central-jet fiducial regions. Both statistical (inner bar) and total (outer bar) measurement uncertainties are shown, as well as ratios of the theoretical predictions to the data (the bottom panel in each distribution).

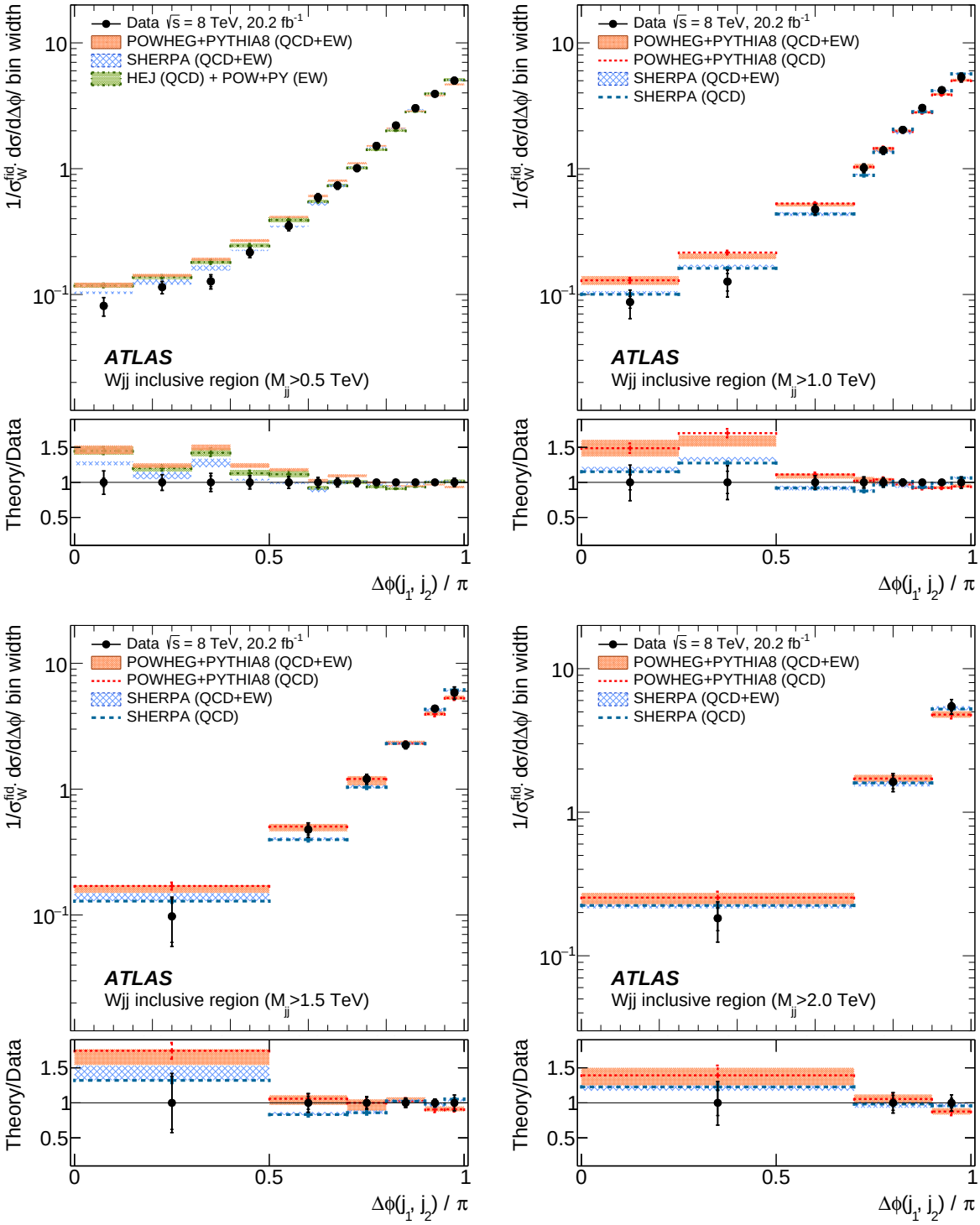

Figure 40: Unfolded normalized differential Wjj production cross sections as a function of $\Delta\phi(j_1, j_2)$ in the inclusive fiducial region with four thresholds on the dijet invariant mass (0.5 TeV, 1.0 TeV, 1.5 TeV, and 2.0 TeV). Both statistical (inner bar) and total (outer bar) measurement uncertainties are shown, as well as ratios of the theoretical predictions to the data (the bottom panel in each distribution).

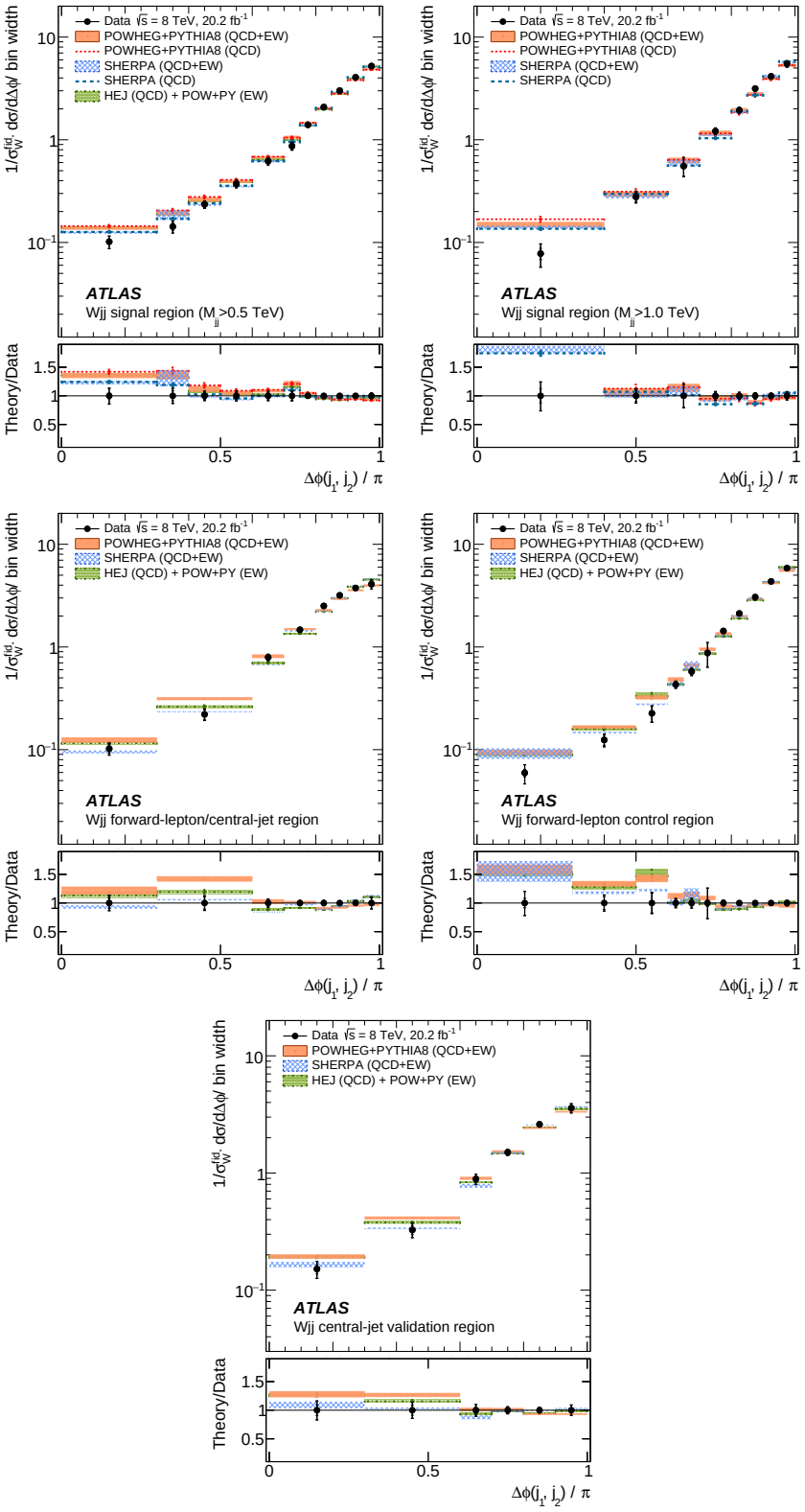

Figure 41: Unfolded normalized differential Wjj production cross sections as a function of $\Delta\phi(j_1, j_2)$ in the signal, high-mass signal, forward-lepton/central-jet, forward-lepton, and central-jet fiducial regions. Both statistical (inner bar) and total (outer bar) measurement uncertainties are shown, as well as ratios of the theoretical predictions to the data (the bottom panel in each distribution).

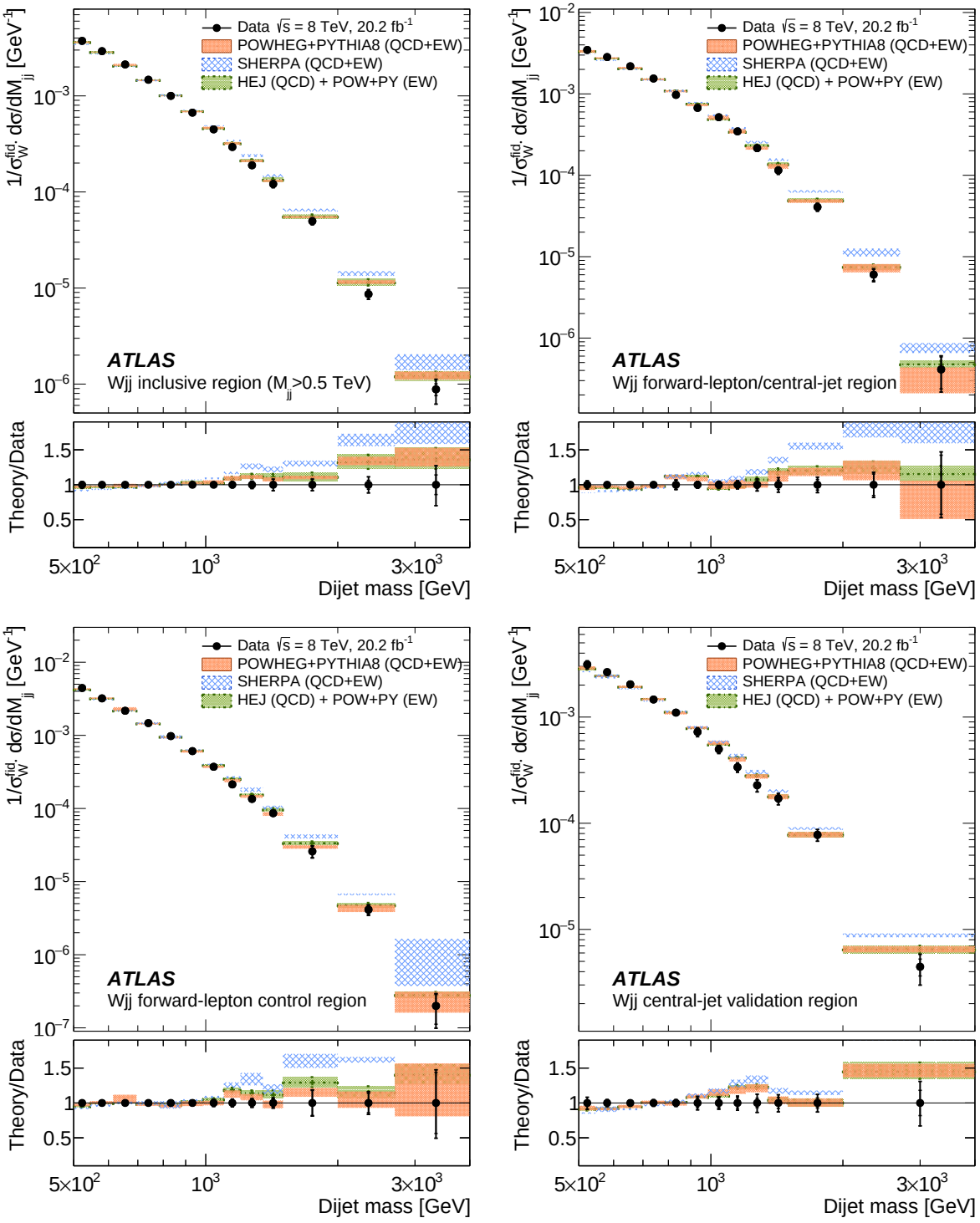

Figure 42: Unfolded normalized differential Wjj production cross sections as a function of dijet invariant mass in the inclusive, forward-lepton/central-jet, forward-lepton, and central-jet fiducial regions. Both statistical (inner bar) and total (outer bar) measurement uncertainties are shown, as well as ratios of the theoretical predictions to the data (the bottom panel in each distribution).

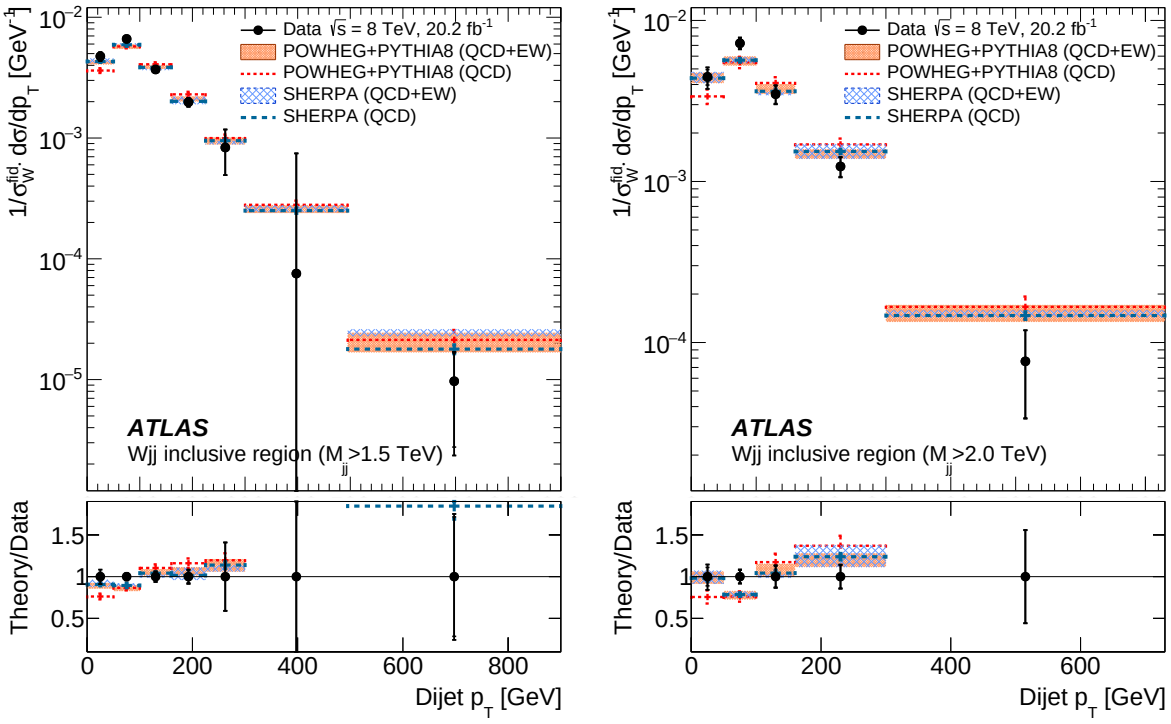

Figure 43: Unfolded normalized differential Wjj production cross sections as a function of dijet p_{T} in the inclusive fiducial region with two thresholds on the dijet invariant mass (1.5 TeV, and 2.0 TeV). Both statistical (inner bar) and total (outer bar) measurement uncertainties are shown, as well as ratios of the theoretical predictions to the data (the bottom panel in each distribution).

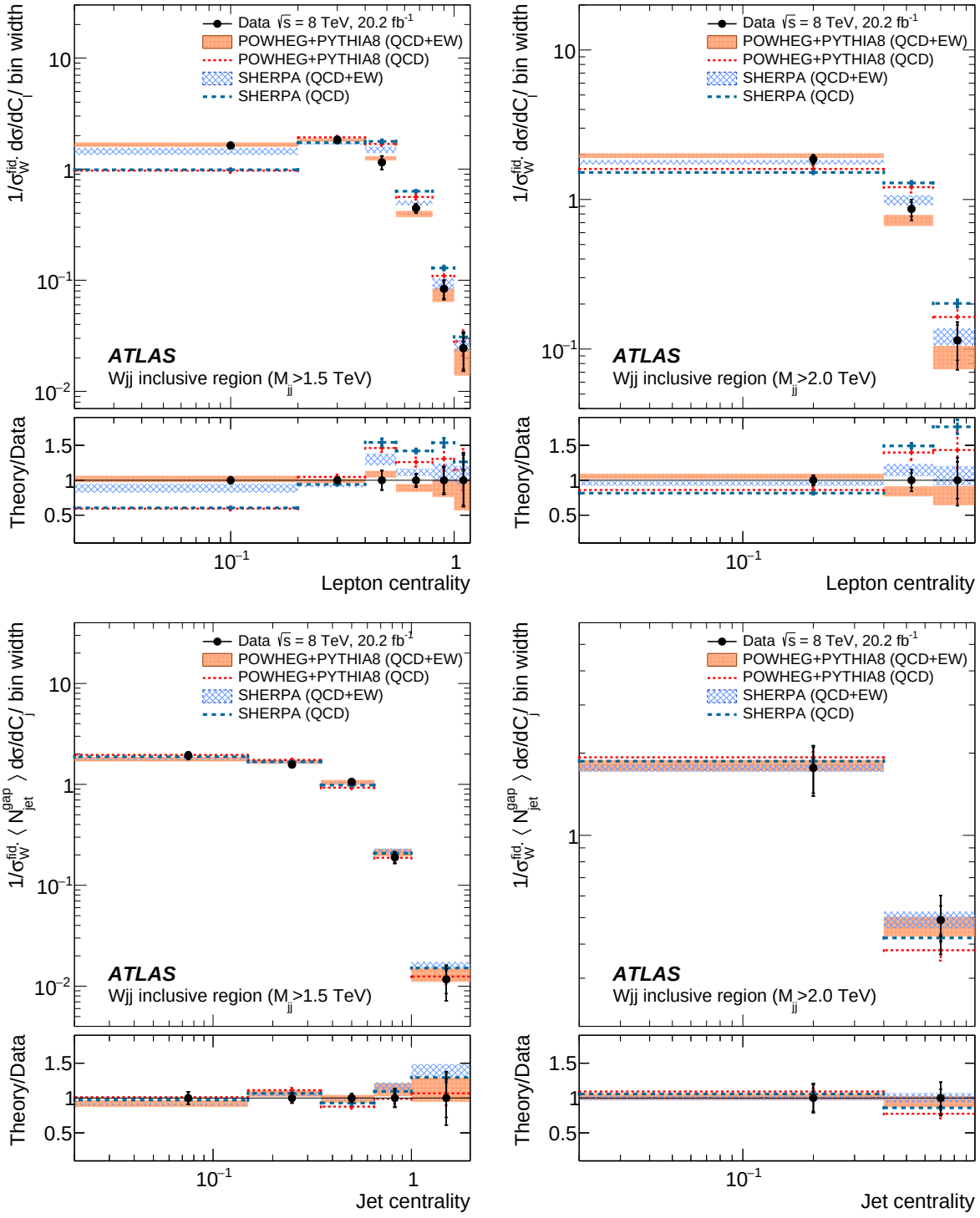

Figure 44: Unfolded normalized differential Wjj production cross sections as a function of lepton centrality (top) and jet centrality (bottom) for the inclusive fiducial region with $M_{jj} > 1.5$ TeV (left) and 2.0 TeV (right). Both statistical (inner bar) and total (outer bar) measurement uncertainties are shown, as well as ratios of the theoretical predictions to the data (the bottom panel in each distribution).

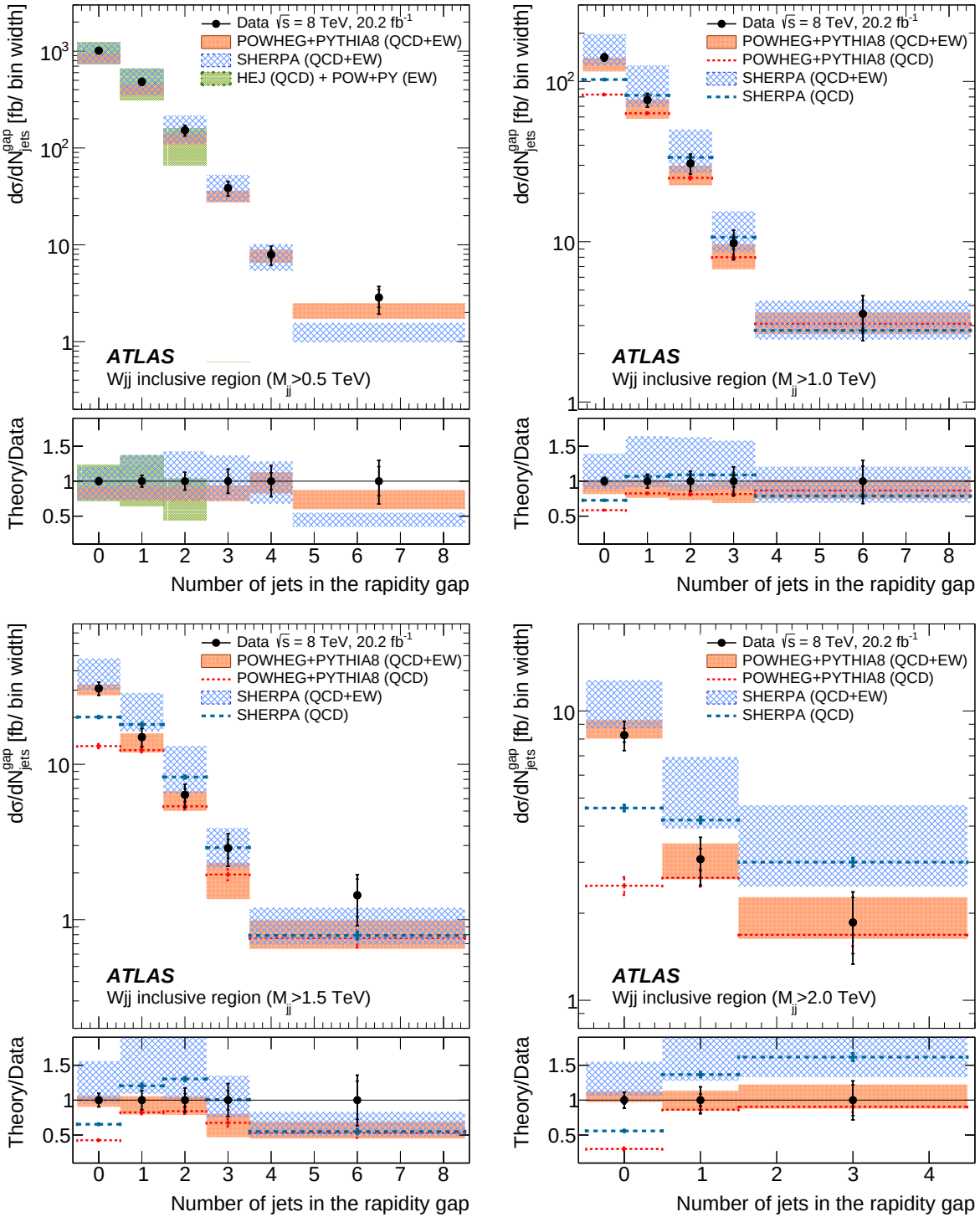

Figure 45: Differential Wjj production cross sections as a function of the number of hard jets in the rapidity interval between the two leading jets in the inclusive fiducial region with four thresholds on the dijet invariant mass (0.5 TeV, 1.0 TeV, 1.5 TeV, and 2.0 TeV). Both statistical (inner bar) and total (outer bar) measurement uncertainties are shown, as well as ratios of the theoretical predictions to the data (the bottom panel in each distribution).

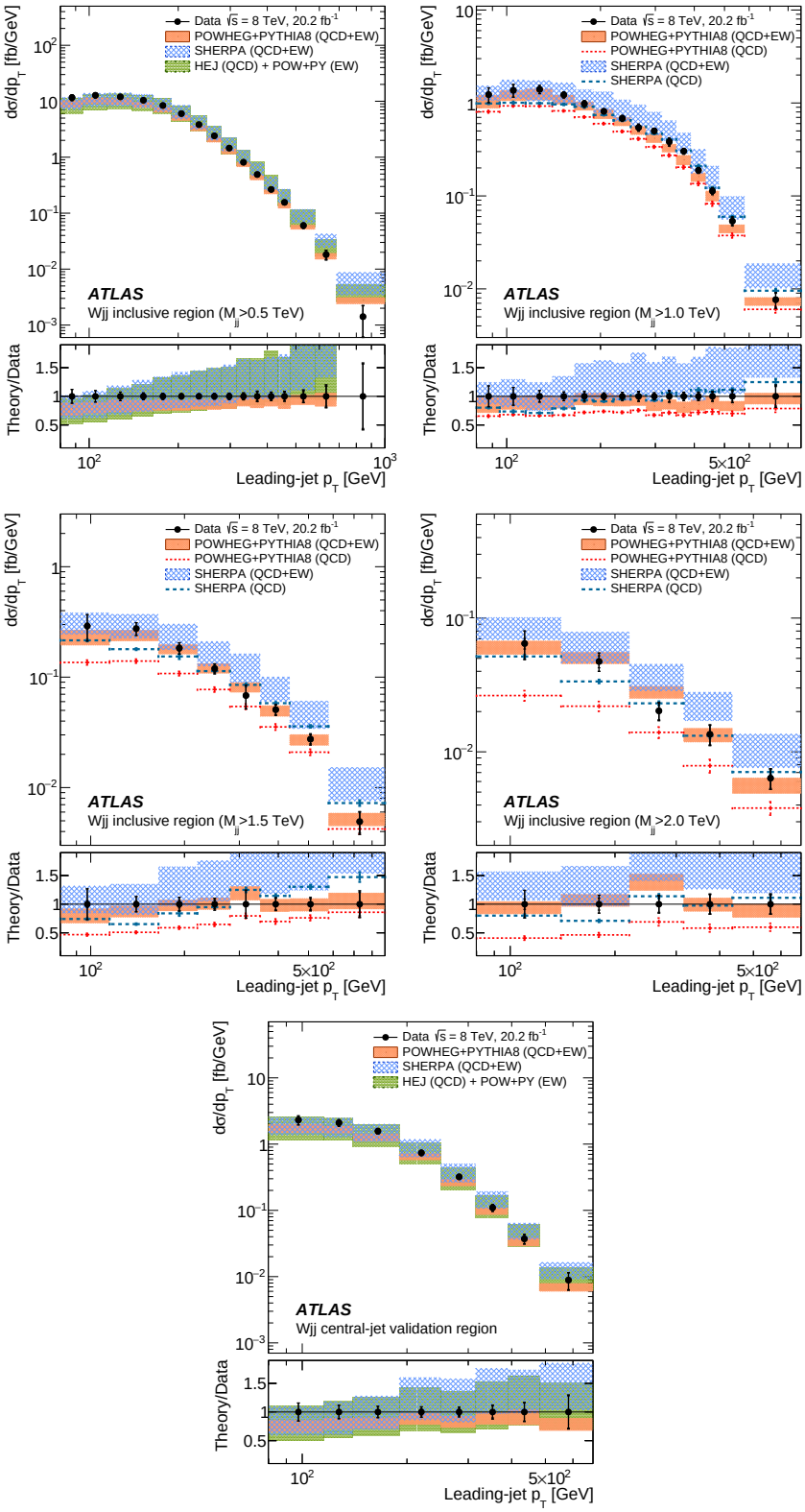

Figure 46: Differential Wjj production cross sections as a function of leading-jet p_{T} in the inclusive fiducial region with four thresholds on the dijet invariant mass (0.5 TeV, 1.0 TeV, 1.5 TeV, and 2.0 TeV), and in the central-jet fiducial region. Both statistical (inner bar) and total (outer bar) measurement uncertainties are shown, as well as ratios of the theoretical predictions to the data (the bottom panel in each distribution).

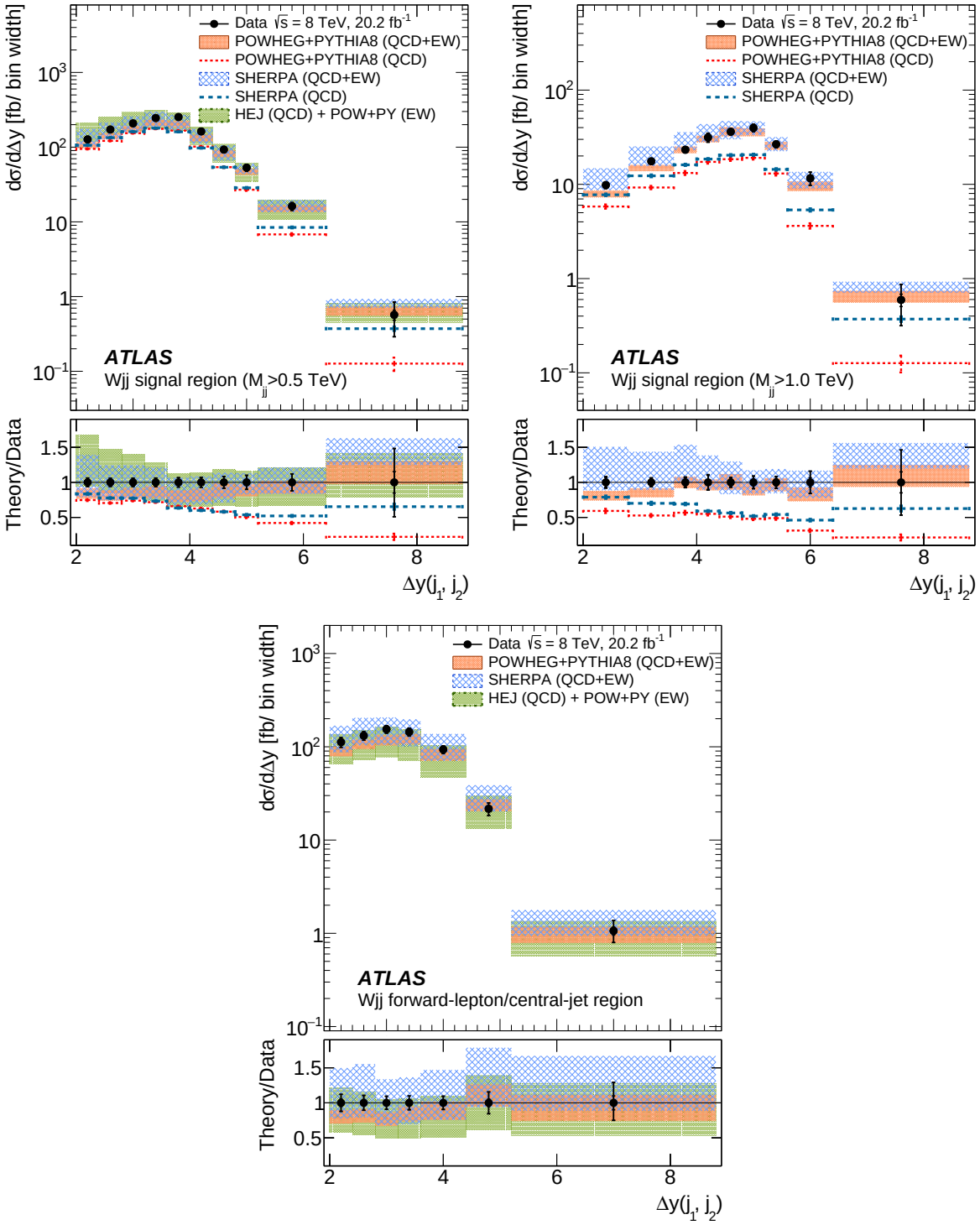

Figure 47: Differential Wjj production cross sections as a function of $\Delta y(j_1, j_2)$ in the signal and high-mass signal fiducial regions, and in the forward-lepton/central-jet fiducial region. Both statistical (inner bar) and total (outer bar) measurement uncertainties are shown, as well as ratios of the theoretical predictions to the data (the bottom panel in each distribution).

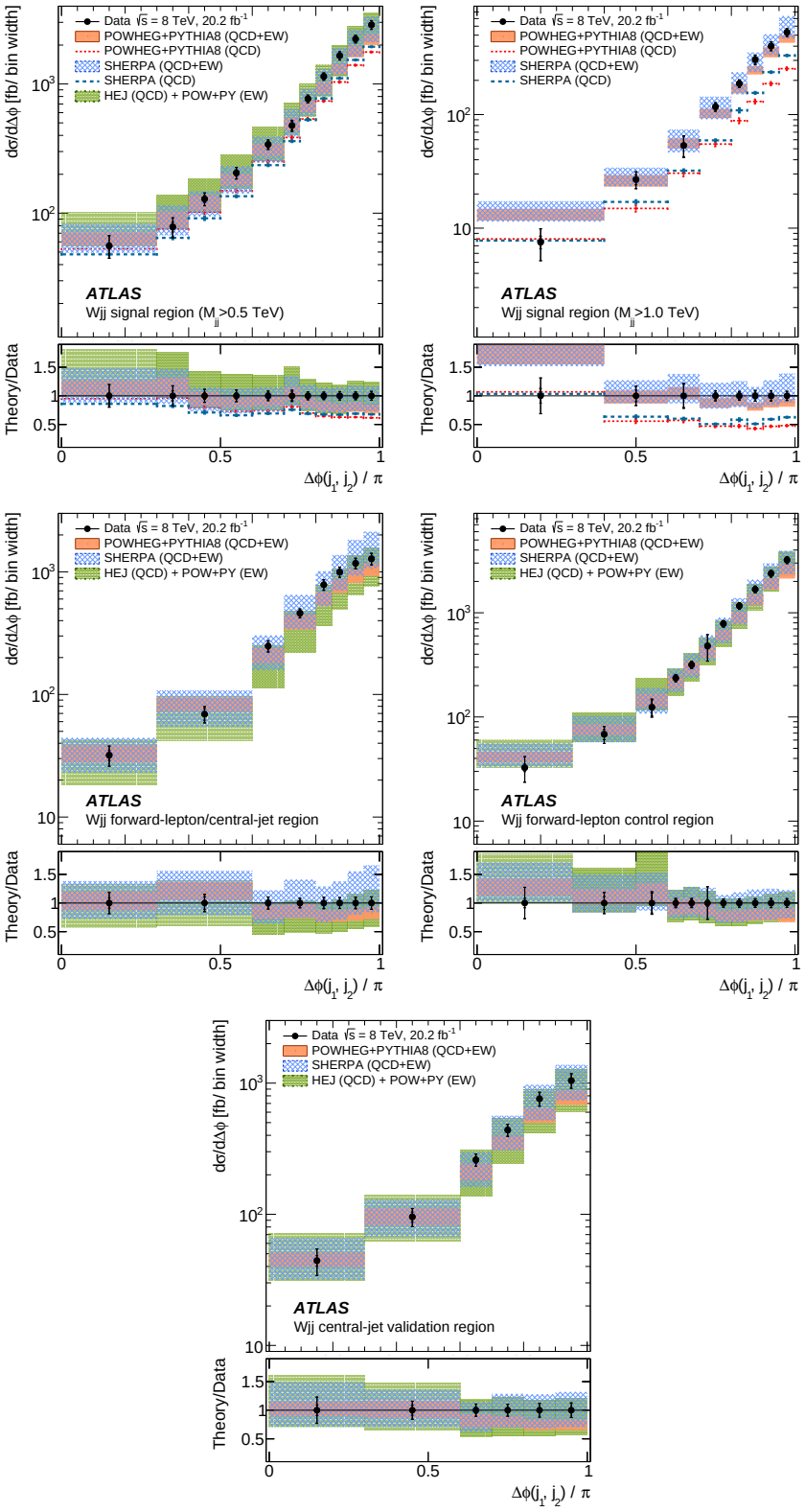

Figure 48: Differential Wjj production cross sections as a function of $\Delta\phi(j_1, j_2)$ in the signal, high-mass signal, forward-lepton/central-jet, forward-lepton, and central-jet fiducial regions. Both statistical (inner bar) and total (outer bar) measurement uncertainties are shown, as well as ratios of the theoretical predictions to the data (the bottom panel in each distribution).

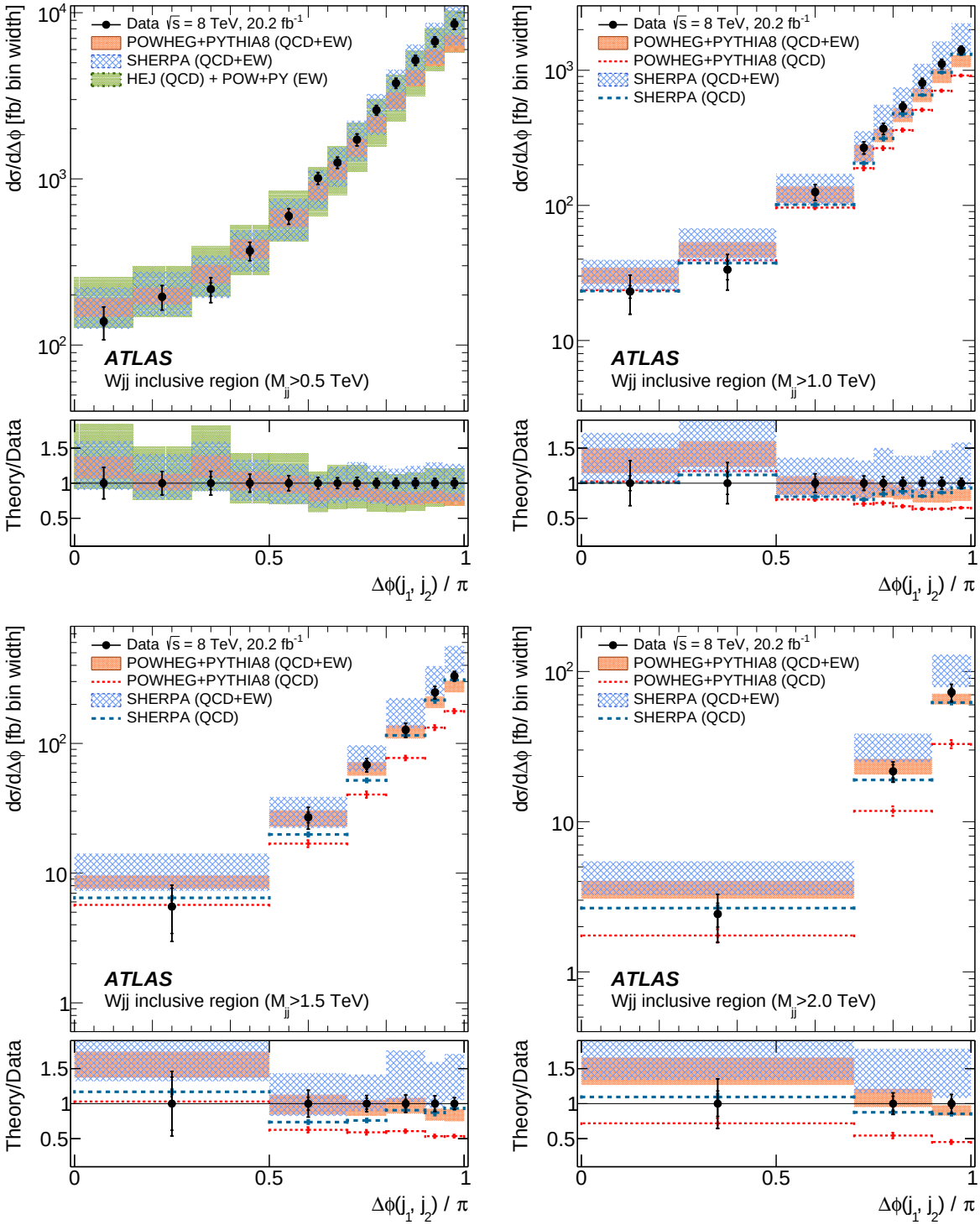

Figure 49: Differential Wjj production cross sections as a function of $\Delta\phi(j_1, j_2)$ in the inclusive fiducial region with four thresholds on the dijet invariant mass (0.5 TeV, 1.0 TeV, 1.5 TeV, and 2.0 TeV). Both statistical (inner bar) and total (outer bar) measurement uncertainties are shown, as well as ratios of the theoretical predictions to the data (the bottom panel in each distribution).

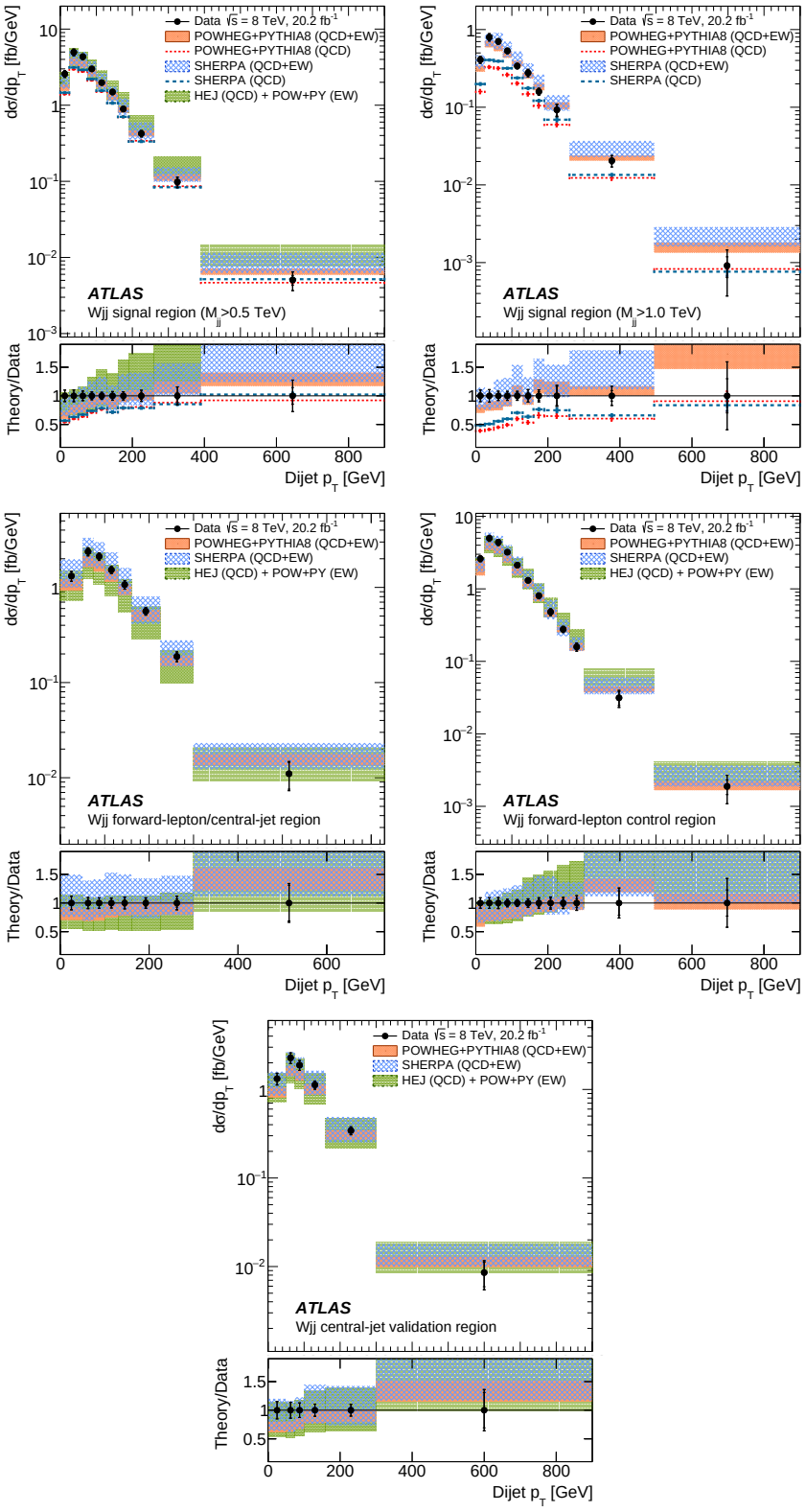

Figure 50: Differential Wjj production cross sections as a function of dijet p_{T} in the signal, high-mass signal, forward-lepton/central-jet, forward-lepton, and central-jet fiducial regions. Both statistical (inner bar) and total (outer bar) measurement uncertainties are shown, as well as ratios of the theoretical predictions to the data (the bottom panel in each distribution).

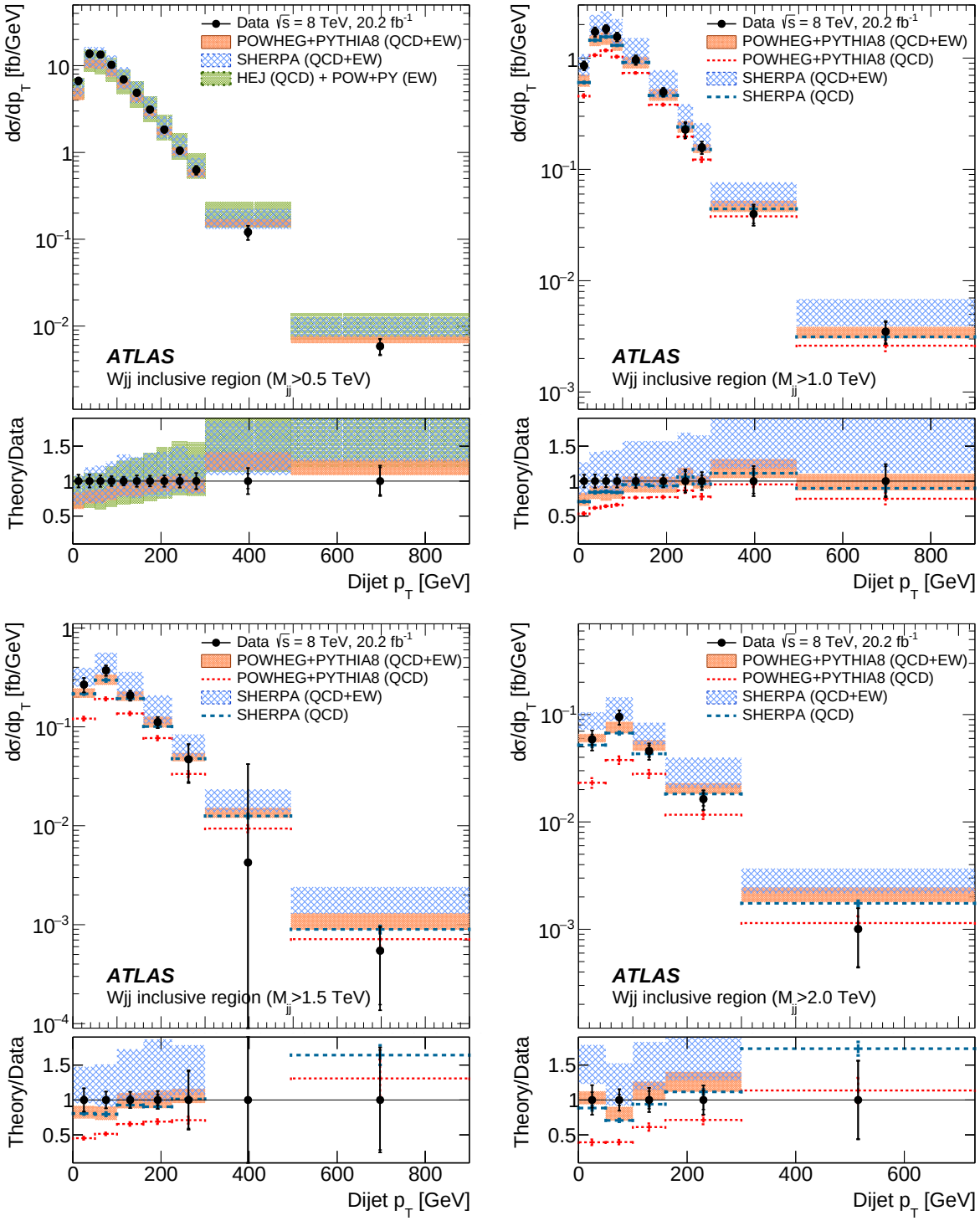

Figure 51: Differential Wjj production cross sections as a function of dijet p_{T} in the inclusive fiducial region with four thresholds on the dijet invariant mass (0.5 TeV, 1.0 TeV, 1.5 TeV, and 2.0 TeV). Both statistical (inner bar) and total (outer bar) measurement uncertainties are shown, as well as ratios of the theoretical predictions to the data (the bottom panel in each distribution).

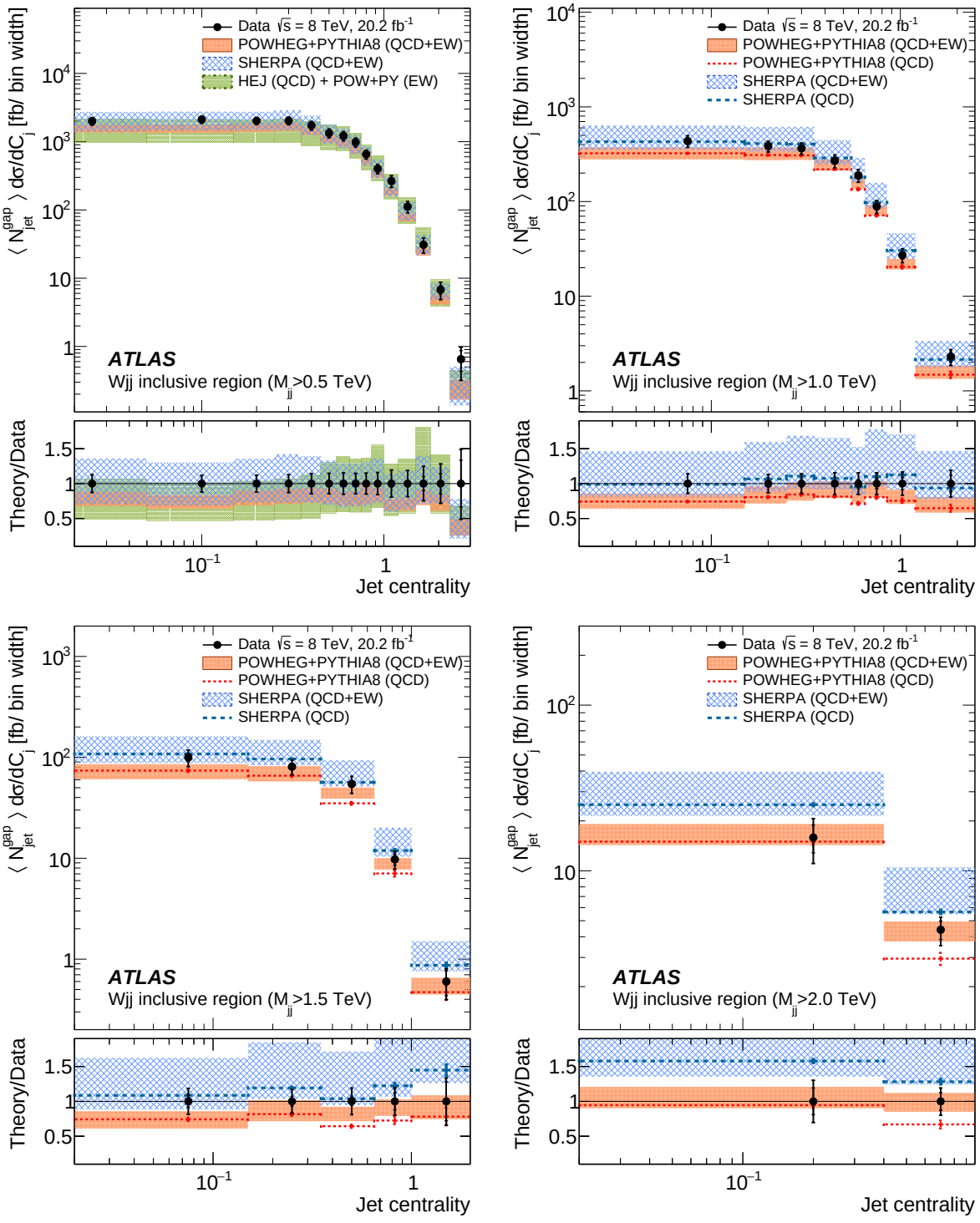

Figure 52: Differential Wjj production cross sections as a function of jet centrality in the inclusive fiducial region with four thresholds on the dijet invariant mass (0.5 TeV, 1.0 TeV, 1.5 TeV, and 2.0 TeV). Both statistical (inner bar) and total (outer bar) measurement uncertainties are shown, as well as ratios of the theoretical predictions to the data (the bottom panel in each distribution).

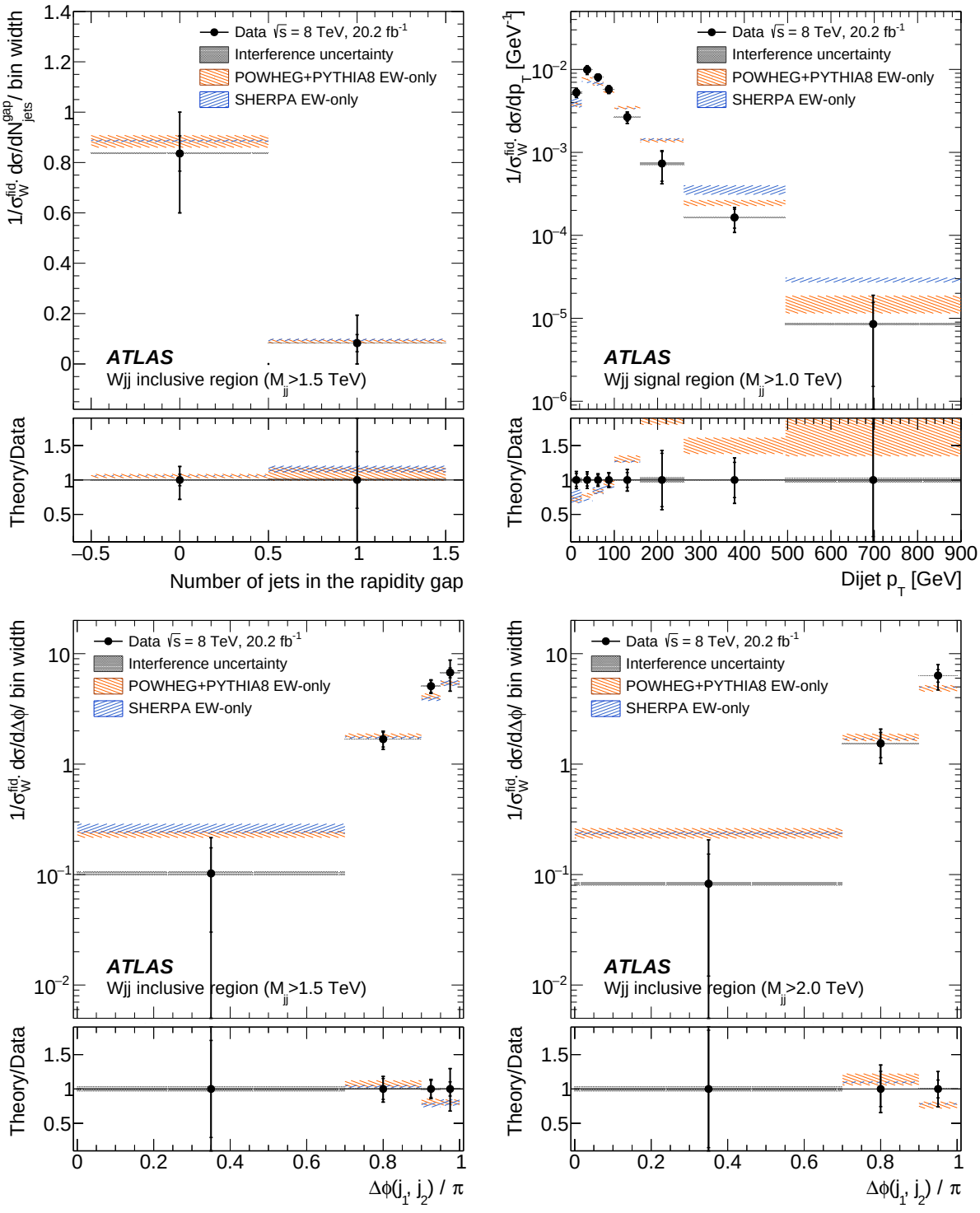

Figure 53: Unfolded normalized differential electroweak Wjj production cross sections as a function of the number of hard jets in the rapidity gap between the two leading jets in the inclusive $M_{jj} > 1.5$ TeV fiducial region, the dijet p_{T} in the high-mass signal region, and the azimuthal angle difference between the two leading jets in the inclusive high-mass ($M_{jj} > 1.5$ TeV and $M_{jj} > 2.0$ TeV) region. Both statistical (inner bar) and total (outer bar) measurement uncertainties are shown, as well as ratios of the theoretical predictions to the data (the bottom panel in each distribution).

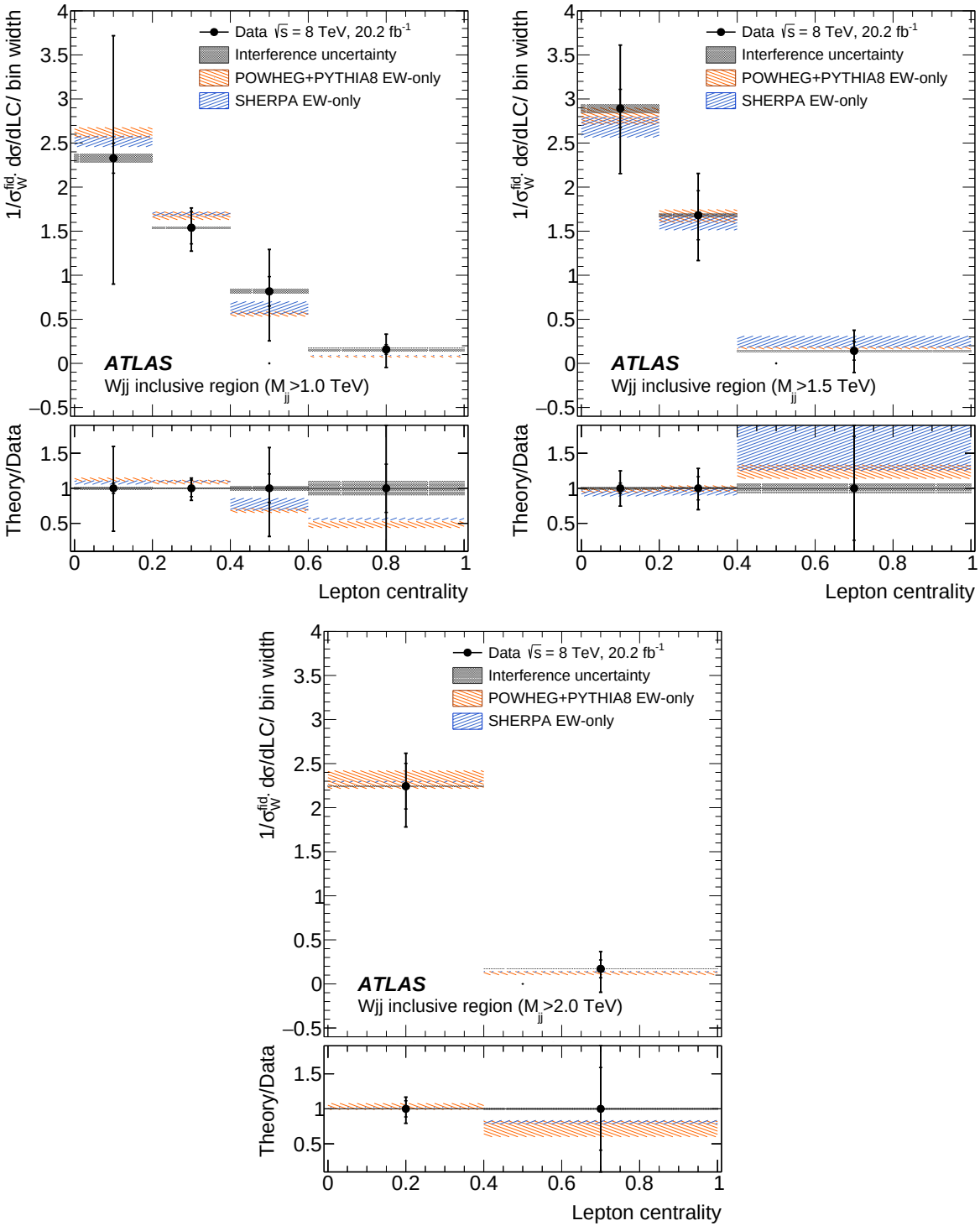

Figure 54: Unfolded normalized differential electroweak Wjj production cross sections as a function of lepton centrality in the inclusive fiducial region with three thresholds on the dijet invariant mass (1.0 TeV, 1.5 TeV, and 2.0 TeV). Both statistical (inner bar) and total (outer bar) measurement uncertainties are shown, as well as ratios of the theoretical predictions to the data (the bottom panel in each distribution).

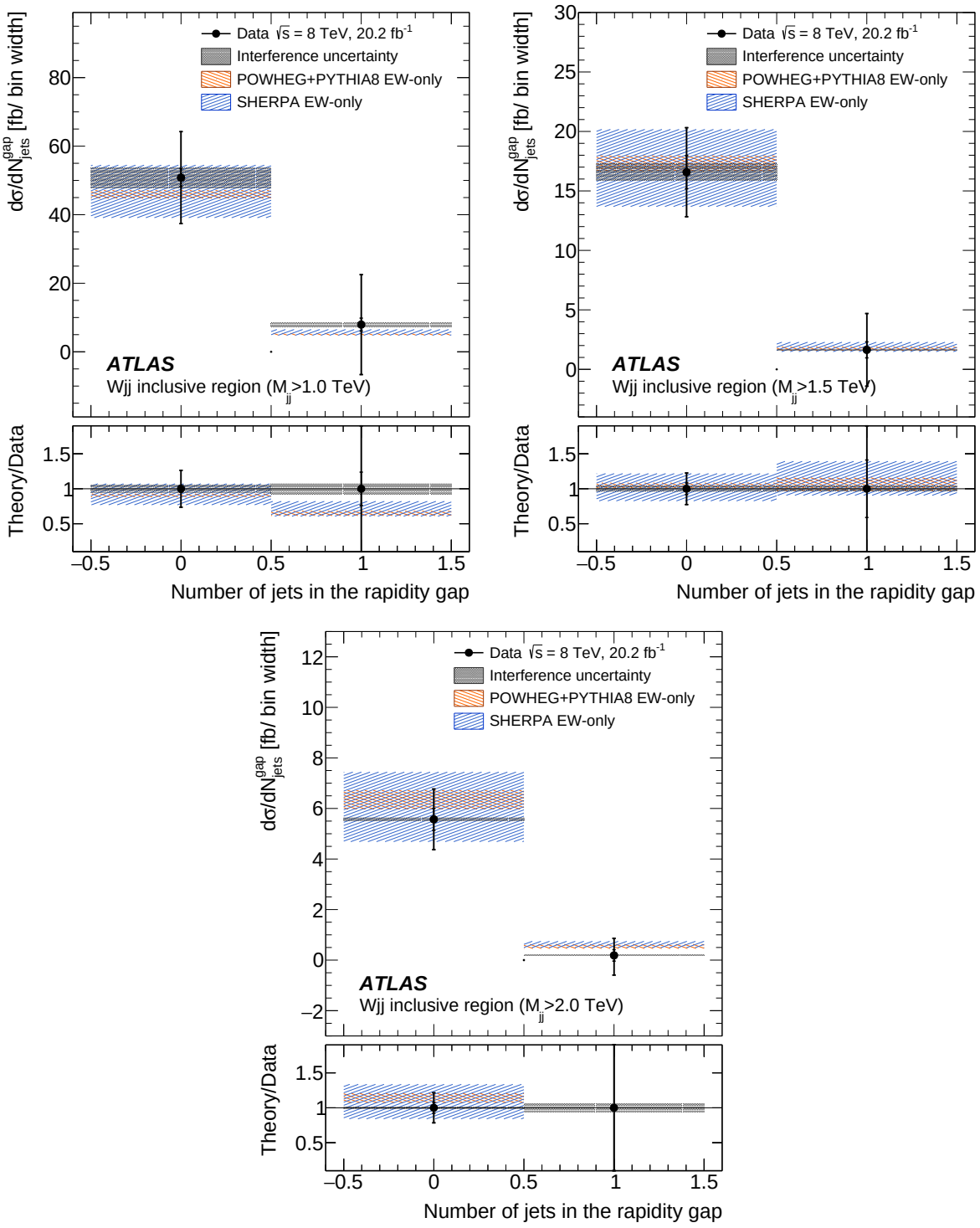

Figure 55: Differential electroweak Wjj production cross sections as a function of the number of hard jets in the rapidity gap between the two leading jets in the inclusive fiducial region with three thresholds on the dijet invariant mass (1.0 TeV, 1.5 TeV, and 2.0 TeV). Both statistical (inner bar) and total (outer bar) measurement uncertainties are shown, as well as ratios of the theoretical predictions to the data (the bottom panel in each distribution).

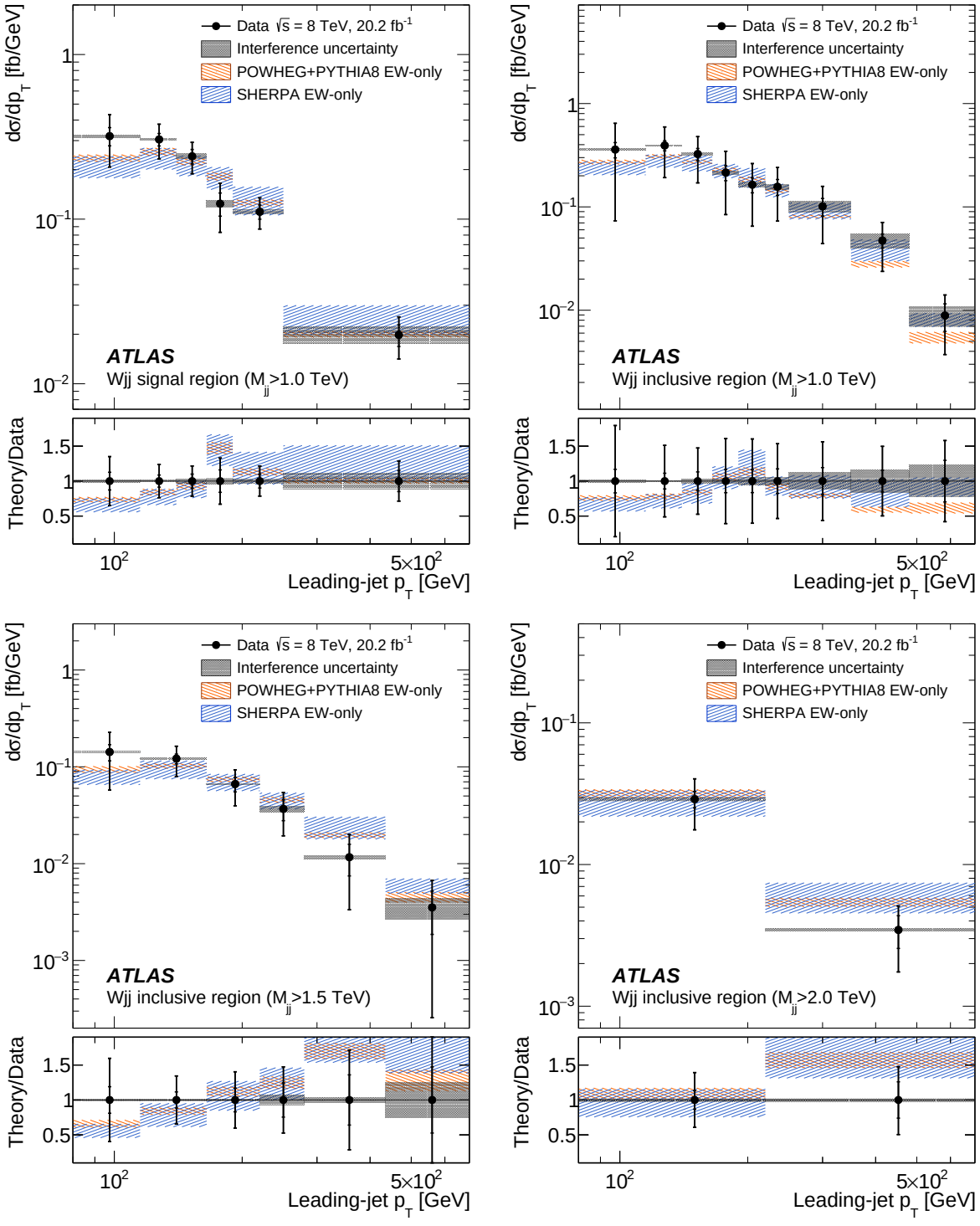

Figure 56: Differential electroweak Wjj production cross sections as a function of the leading-jet p_{T} in the high-mass signal region and the inclusive fiducial region with three thresholds on the dijet invariant mass (1.0 TeV, 1.5 TeV, and 2.0 TeV). Both statistical (inner bar) and total (outer bar) measurement uncertainties are shown, as well as ratios of the theoretical predictions to the data (the bottom panel in each distribution).

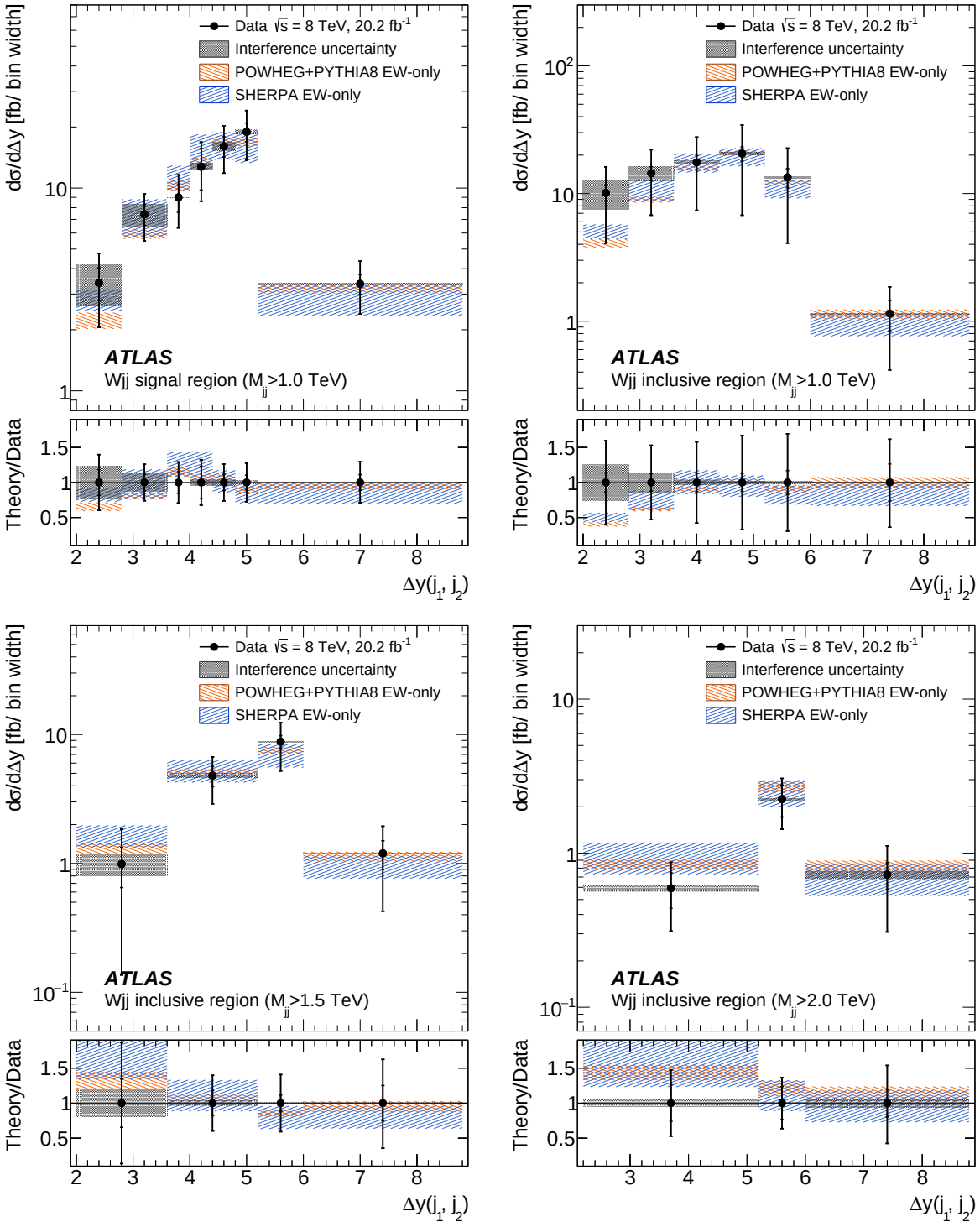

Figure 57: Differential electroweak Wjj production cross sections as a function of $\Delta y(j_1, j_2)$ in the high-mass signal region and the inclusive fiducial region with three thresholds on the dijet invariant mass (1.0 TeV, 1.5 TeV, and 2.0 TeV). Both statistical (inner bar) and total (outer bar) measurement uncertainties are shown, as well as ratios of the theoretical predictions to the data (the bottom panel in each distribution).

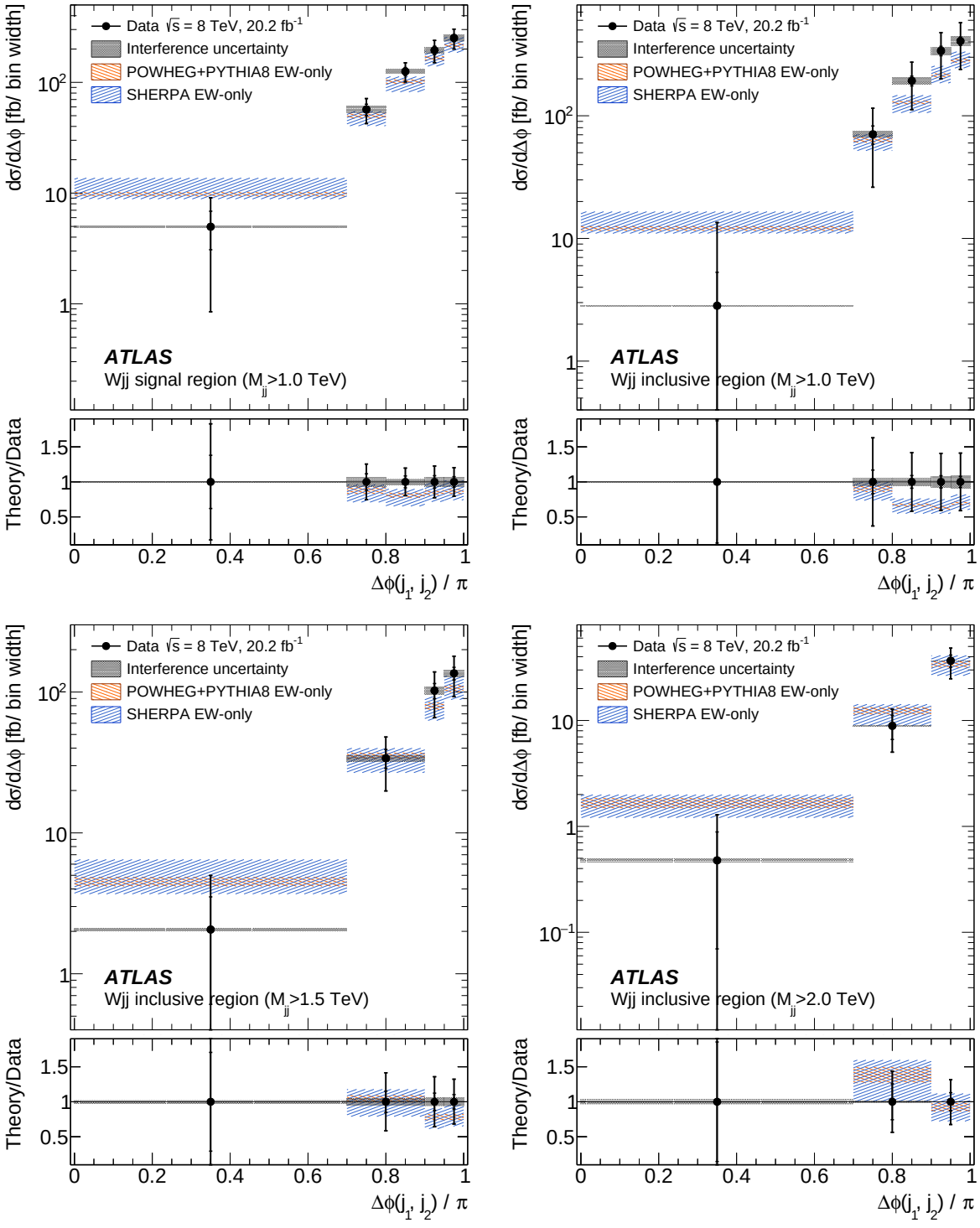

Figure 58: Differential electroweak Wjj production cross sections as a function of $\Delta\phi(j_1, j_2)$ in the high-mass signal region and the inclusive fiducial region with three thresholds on the dijet invariant mass (1.0 TeV, 1.5 TeV, and 2.0 TeV). Both statistical (inner bar) and total (outer bar) measurement uncertainties are shown, as well as ratios of the theoretical predictions to the data (the bottom panel in each distribution).

References

[1] ATLAS Collaboration, *Search for invisible decays of a Higgs boson using vector-boson fusion in pp collisions at* $\sqrt{s} = 8$ *TeV with the ATLAS detector*, JHEP **01** (2016) 172, arXiv: 1508.07869 [hep-ex].

[2] CMS Collaboration, *Searches for invisible decays of the Higgs boson in pp collisions at* $\sqrt{s} = 7$, *8, and 13 TeV*, (2016), arXiv: 1610.09218 [hep-ex].

[3] CMS Collaboration, *Search for invisible decays of Higgs bosons in the vector boson fusion and associated ZH production modes*, Eur. Phys. J. C **74** (2014) 2980, arXiv: 1404.1344 [hep-ex].

[4] ATLAS Collaboration, *Search for a Charged Higgs Boson Produced in the Vector-Boson Fusion Mode with Decay* $H^{\pm} \to W^{\pm}Z$ *using pp Collisions at* $\sqrt{s} = 8$ *TeV with the ATLAS Experiment*, Phys. Rev. Lett. **114** (2015) 231801, arXiv: 1503.04233 [hep-ex].

[5] CMS Collaboration, *Search for dark matter and supersymmetry with a compressed mass spectrum in the vector boson fusion topology in proton-proton collisions at* $\sqrt{s} = 8$ *TeV*, Phys. Rev. Lett. **118** (2017) 021802, arXiv: 1605.09305 [hep-ex].

[6] CMS Collaboration, *Search for supersymmetry in the vector-boson fusion topology in proton-proton collisions at* $\sqrt{s} = 8$ *TeV*, JHEP **11** (2015) 189, arXiv: 1508.07628 [hep-ex].

[7] A. G. Delannoy et al., *Probing Dark Matter at the LHC using Vector Boson Fusion Processes*, Phys. Rev. Lett. **111** (2013) 061801, arXiv: 1304.7779 [hep-ph].

[8] B. Dutta et al., *Vector Boson Fusion Processes as a Probe of Supersymmetric Electroweak Sectors at the LHC*, Phys. Rev. D **87** (2013) 035029, arXiv: 1210.0964 [hep-ph].

[9] T. Liu, L. Wang and J. M. Yang, *Pseudo-goldstino and electroweakinos via VBF processes at LHC*, JHEP **02** (2015) 177, arXiv: 1411.6105 [hep-ph].

[10] C. Englert, E. Re and M. Spannowsky, *Pinning down Higgs triplets at the LHC*, Phys. Rev. D **88** (2013) 035024, arXiv: 1306.6228 [hep-ph].

[11] G. Bambhaniya, J. Chakrabortty, J. Gluza, T. Jelinski and R. Szafron, *Search for doubly charged Higgs bosons through vector boson fusion at the LHC and beyond*, Phys. Rev. D **92** (2015) 015016, arXiv: 1504.03999 [hep-ph].

[12] J. D. Bjorken, *Rapidity gaps and jets as a new physics signature in very high-energy hadron hadron collisions*, Phys. Rev. D **47** (1993) 101.

[13] CMS Collaboration, *Measurement of electroweak production of a W boson and two forward jets in proton-proton collisions at* $\sqrt{s} = 8$ *TeV*, JHEP **11** (2016) 147, arXiv: 1607.06975 [hep-ex].

[14] ATLAS Collaboration, *Measurement of the electroweak production of dijets in association with a Z boson and distributions sensitive to vector boson fusion in proton-proton collisions at* $\sqrt{s} = 8$ *TeV using the ATLAS detector*, JHEP **04** (2014) 031, arXiv: 1401.7610 [hep-ex].

[15] CMS Collaboration, *Measurement of electroweak production of two jets in association with a Z boson in proton-proton collisions at* $\sqrt{s} = 8$ *TeV*, Eur. Phys. J. C **75** (2015) 66, arXiv: 1410.3153 [hep-ex].

[16] ATLAS and CMS Collaborations,
Measurements of the Higgs boson production and decay rates and constraints on its couplings from a combined ATLAS and CMS analysis of the LHC pp collision data at $\sqrt{s} = 7$ *and* 8 *TeV*,
JHEP **08** (2016) 045, arXiv: 1606.02266 [hep-ex].

[17] ATLAS Collaboration, *Measurements of the W production cross sections in association with jets with the ATLAS detector*, Eur. Phys. J. C **75** (2015) 82, arXiv: 1409.8639 [hep-ex].

[18] CMS Collaboration, *Differential cross section measurements for the production of a W boson in association with jets in proton–proton collisions at* $\sqrt{s} = 7$ *TeV*, Phys. Lett. B **741** (2015) 12, arXiv: 1406.7533 [hep-ex].

[19] CDF Collaboration, T. Aaltonen et al., *Measurement of the cross section for* W^- *boson production in association with jets in* $p\bar{p}$ *collisions at* $\sqrt{s} = 1.96$*-TeV*, Phys. Rev. D **77** (2008) 011108, arXiv: 0711.4044 [hep-ex].

[20] D0 Collaboration, V. M. Abazov et al.,
Studies of W boson plus jets production in $p\bar{p}$ *collisions at* $\sqrt{s} = 1.96$ *TeV*,
Phys. Rev. D **88** (2013) 092001, arXiv: 1302.6508 [hep-ex].

[21] J. M. Campbell and R. K. Ellis,
Next-to-leading order corrections to W+2 jet and Z+2 jet production at hadron colliders,
Phys. Rev. D **65** (2002) 113007, arXiv: hep-ph/0202176.

[22] J. M. Campbell, R. K. Ellis and D. L. Rainwater,
Next-to-leading order QCD predictions for W + 2 jet and Z + 2 jet production at the CERN LHC,
Phys. Rev. D **68** (2003) 094021, arXiv: hep-ph/0308195.

[23] R. K. Ellis, K. Melnikov and G. Zanderighi, *W+3 jet production at the Tevatron*,
Phys. Rev. D **80** (2009) 094002, arXiv: 0906.1445 [hep-ph].

[24] C. F. Berger et al., *Precise Predictions for W + 3 Jet Production at Hadron Colliders*,
Phys. Rev. Lett. **102** (2009) 222001, arXiv: 0902.2760 [hep-ph].

[25] C. F. Berger et al., *Precise Predictions for W + 4 Jet Production at the Large Hadron Collider*,
Phys. Rev. Lett. **106** (2011) 092001, arXiv: 1009.2338 [hep-ph].

[26] Z. Bern et al., *Next-to-Leading Order W + 5-Jet Production at the LHC*,
Phys. Rev. D **88** (2013) 014025, arXiv: 1304.1253 [hep-ph].

[27] S. Hoeche, F. Krauss, M. Schoenherr and F. Siegert,
QCD matrix elements + parton showers: The NLO case, JHEP **04** (2013) 027,
arXiv: 1207.5030 [hep-ph].

[28] J. Alwall et al., *The automated computation of tree-level and next-to-leading order differential cross sections, and their matching to parton shower simulations*, JHEP **07** (2014) 079,
arXiv: 1405.0301 [hep-ph].

[29] J. M. Campbell, R. K. Ellis, P. Nason and G. Zanderighi,
W and Z bosons in association with two jets using the POWHEG method, JHEP **08** (2013) 005,
arXiv: 1303.5447 [hep-ph].

[30] J. R. Andersen and J. M. Smillie, *Constructing All-Order Corrections to Multi-Jet Rates*,
JHEP **01** (2010) 039, arXiv: 0908.2786 [hep-ph].

[31] J. R. Andersen and J. M. Smillie,
The Factorisation of the t-channel Pole in Quark-Gluon Scattering,
Phys. Rev. D **81** (2010) 114021, arXiv: 0910.5113 [hep-ph].

[32] J. R. Andersen and J. M. Smillie, *Multiple Jets at the LHC with High Energy Jets*, JHEP **06** (2011) 010, arXiv: 1101.5394 [hep-ph].

[33] J. R. Andersen, T. Hapola and J. M. Smillie, *W Plus Multiple Jets at the LHC with High Energy Jets*, JHEP **09** (2012) 047, arXiv: 1206.6763 [hep-ph].

[34] K. Hagiwara, R. D. Peccei, D. Zeppenfeld and K. Hikasa, *Probing the Weak Boson Sector in $e^+e^- \to W^+W^-$*, Nucl. Phys. B **282** (1987) 253.

[35] C. Oleari and D. Zeppenfeld, *QCD corrections to electroweak $\nu(\ell)jj$ and $\ell^+\ell^- jj$ production*, Phys. Rev. D **69** (2004) 093004, arXiv: hep-ph/0310156.

[36] F. Schissler and D. Zeppenfeld, *Parton Shower Effects on W and Z Production via Vector Boson Fusion at NLO QCD*, JHEP **04** (2013) 057, arXiv: 1302.2884 [hep-ph].

[37] ATLAS Collaboration, *The ATLAS Experiment at the CERN Large Hadron Collider*, JINST **3** (2008) S08003.

[38] ATLAS Collaboration, *The ATLAS Inner Detector commissioning and calibration*, Eur. Phys. J. C **70** (2010) 787, arXiv: 1004.5293 [physics.ins-det].

[39] ATLAS Collaboration, *Performance of the ATLAS Inner Detector Track and Vertex Reconstruction in High Pile-Up LHC Environment*, ATLAS-CONF-2012-042, 2012, URL: https://cdsweb.cern.ch/record/1435196.

[40] ATLAS Collaboration, *Electron and photon energy calibration with the ATLAS detector using LHC Run 1 data*, Eur. Phys. J. C **74** (2014) 3071, arXiv: 1407.5063 [hep-ex].

[41] ATLAS Collaboration, *Electron reconstruction and identification efficiency measurements with the ATLAS detector using the 2011 LHC proton-proton collision data*, Eur. Phys. J. C **74** (2014) 2941, arXiv: 1404.2240 [hep-ex].

[42] ATLAS Collaboration, *Electron efficiency measurements with the ATLAS detector using the 2012 LHC proton-proton collision data*, ATLAS-CONF-2014-032, 2014, URL: https://cdsweb.cern.ch/record/1706245.

[43] ATLAS Collaboration, *Measurement of the muon reconstruction performance of the ATLAS detector using 2011 and 2012 LHC proton-proton collision data*, Eur. Phys. J. C **74** (2014) 3130, arXiv: 1407.3935 [hep-ex].

[44] ATLAS Collaboration, *Jet energy measurement and its systematic uncertainty in proton-proton collisions at $\sqrt{s} = 7$ TeV with the ATLAS detector*, Eur. Phys. J. C **75** (2015) 17, arXiv: 1406.0076 [hep-ex].

[45] M. Cacciari, G. P. Salam and G. Soyez, *The anti-k_t jet clustering algorithm*, JHEP **04** (2008) 063, arXiv: 0802.1189 [hep-ph].

[46] ATLAS Collaboration, *Topological cell clustering in the ATLAS calorimeters and its performance in LHC Run 1*, (2016), submitted to Eur. Phys. J. C, arXiv: 1603.02934 [hep-ex].

[47] ATLAS Collaboration, *Monte Carlo Calibration and Combination of In-situ Measurements of Jet Energy Scale, Jet Energy Resolution and Jet Mass in ATLAS*, ATLAS-CONF-2015-037, 2015, URL: https://cdsweb.cern.ch/record/2044941.

[48] ATLAS Collaboration, *Performance of pile-up mitigation techniques for jets in pp collisions at $\sqrt{s}$ = 8 TeV using the ATLAS detector*, Eur. Phys. J. C **76** (2016) 581, arXiv: 1510.03823 [hep-ex].

[49] ATLAS Collaboration, *Performance of b-Jet Identification in the ATLAS Experiment*, JINST **11** (2016) P04008, arXiv: 1512.01094 [hep-ex].

[50] ATLAS Collaboration, *Performance of Missing Transverse Momentum Reconstruction in Proton-Proton Collisions at 7 TeV with ATLAS*, Eur. Phys. J. C **72** (2012) 1844, arXiv: 1108.5602 [hep-ex].

[51] ATLAS Collaboration, *Performance of Missing Transverse Momentum Reconstruction in ATLAS studied in Proton-Proton Collisions recorded in 2012 at 8 TeV*, ATLAS-CONF-2013-082, 2013, URL: https://cdsweb.cern.ch/record/1570993.

[52] ATLAS Collaboration, *Improved luminosity determination in pp collisions at $\sqrt{s}$ = 7 TeV using the ATLAS detector at the LHC*, Eur. Phys. J. C **73** (2013) 2518, arXiv: 1302.4393 [hep-ex].

[53] ATLAS Collaboration, *Luminosity determination in pp collisions at $\sqrt{s}$ = 8 TeV using the ATLAS detector at the LHC*, Eur. Phys. J. C **76** (2016) 653, arXiv: 1608.03953 [hep-ex].

[54] ATLAS Collaboration, *The ATLAS Simulation Infrastructure*, Eur. Phys. J. C **70** (2010) 823, arXiv: 1005.4568 [physics.ins-det].

[55] S. Agostinelli et al., *GEANT4: A simulation toolkit*, Nucl. Instrum. Meth. A **506** (2003) 250.

[56] T. Sjöstrand, S. Mrenna and P. Z. Skands, *A Brief Introduction to PYTHIA 8.1*, Comput. Phys. Commun. **178** (2008) 852, arXiv: 0710.3820 [hep-ph].

[57] P. Nason, *A New method for combining NLO QCD with shower Monte Carlo algorithms*, JHEP **11** (2004) 040, arXiv: hep-ph/0409146.

[58] S. Frixione, P. Nason and C. Oleari, *Matching NLO QCD computations with Parton Shower simulations: the POWHEG method*, JHEP **11** (2007) 070, arXiv: 0709.2092 [hep-ph].

[59] ATLAS Collaboration, *Summary of ATLAS PYTHIA 8 tunes*, ATLAS-PUB-2011-003, 2012, URL: https://cdsweb.cern.ch/record/1474107.

[60] H.-L. Lai et al., *New parton distributions for collider physics*, Phys. Rev. D **82** (2010) 074024, arXiv: 1007.2241 [hep-ph].

[61] K. Hamilton, P. Nason and G. Zanderighi, *MINLO: Multi-Scale Improved NLO*, JHEP **10** (2012) 155, arXiv: 1206.3572 [hep-ph].

[62] M. Bahr et al., *Herwig++ Physics and Manual*, Eur. Phys. J. C **58** (2008) 639, arXiv: 0803.0883 [hep-ph].

[63] J. M. Butterworth, J. R. Forshaw and M. H. Seymour, *Multiparton interactions in photoproduction at HERA*, Z. Phys. C **72** (1996) 637, arXiv: hep-ph/9601371.

[64] T. Gleisberg et al., *Event generation with SHERPA 1.1*, JHEP **02** (2009) 007, arXiv: 0811.4622 [hep-ph].

[65] S. Catani, F. Krauss, R. Kuhn and B. R. Webber, *QCD matrix elements + parton showers*, JHEP **11** (2001) 063, arXiv: hep-ph/0109231.

[66] S. Kallweit, J. M. Lindert, P. Maierhofer, S. Pozzorini and M. Schönherr, *NLO QCD+EW predictions for V + jets including off-shell vector-boson decays and multijet merging*, JHEP **04** (2016) 021, arXiv: 1511.08692 [hep-ph].

[67] S. Kallweit, J. M. Lindert, P. Maierhöfer, S. Pozzorini and M. Schönherr, *NLO electroweak automation and precise predictions for W+multijet production at the LHC*, JHEP **04** (2015) 012, arXiv: 1412.5157 [hep-ph].

[68] M. Czakon and A. Mitov, *Top++: A Program for the Calculation of the Top-Pair Cross-Section at Hadron Colliders*, Comput. Phys. Commun. **185** (2014) 2930, arXiv: 1112.5675 [hep-ph].

[69] S. Frixione and B. R. Webber, *Matching NLO QCD computations and parton shower simulations*, JHEP **06** (2002) 029, arXiv: hep-ph/0204244.

[70] G. Corcella et al., *HERWIG 6: An Event generator for hadron emission reactions with interfering gluons (including supersymmetric processes)*, JHEP **0101** (2001) 010, arXiv: hep-ph/0011363.

[71] T. Sjöstrand, S. Mrenna and P. Z. Skands, *PYTHIA 6.4 Physics and Manual*, JHEP **05** (2006) 026, arXiv: hep-ph/0603175.

[72] B. P. Kersevan and E. Richter-Was, *The Monte Carlo event generator AcerMC versions 2.0 to 3.8 with interfaces to PYTHIA 6.4, HERWIG 6.5 and ARIADNE 4.1*, Comput. Phys. Commun. **184** (2013) 919, arXiv: hep-ph/0405247.

[73] J. Pumplin et al., *New generation of parton distributions with uncertainties from global QCD analysis*, JHEP **07** (2002) 012, arXiv: hep-ph/0201195.

[74] S. Hoeche, F. Krauss, M. Schoenherr and F. Siegert, *NLO matrix elements and truncated showers*, JHEP **08** (2011) 123, arXiv: 1009.1127 [hep-ph].

[75] J. M. Campbell, R. K. Ellis and C. Williams, *Vector boson pair production at the LHC*, JHEP **07** (2011) 018, arXiv: 1105.0020 [hep-ph].

[76] W. Verkerke and D. P. Kirkby, *The RooFit toolkit for data modeling*, 2003, arXiv: physics/0306116 [physics.data-an].

[77] HEPDATA repository for all differential and integrated production cross-sections, uncertainties, and correlations measured in this paper, 2016, URL: http://HEPDATA-TO-BE-ADDED.

[78] T. Adye, *Unfolding algorithms and tests using RooUnfold*, 2011, arXiv: 1105.1160 [physics.data-an].

[79] G. D'Agostini, *Improved iterative Bayesian unfolding*, 2010, arXiv: 1010.0632 [physics.data-an].

[80] K. G. Hayes, M. L. Perl and B. Efron, *Application of the Bootstrap Statistical Method to the Tau Decay Mode Problem*, Phys. Rev. D **39** (1989) 274.

[81] A. Denner, L. Hofer, A. Scharf and S. Uccirati, *Electroweak corrections to lepton pair production in association with two hard jets at the LHC*, JHEP **01** (2015) 094, arXiv: 1411.0916 [hep-ph].

[82] T. Plehn, D. Rainwater and D. Zeppenfeld, *Determining the Structure of Higgs Couplings at the CERN Large Hadron Collider*, Phys. Rev. Lett. **88** (2002) 051801.

[83] ATLAS Collaboration,
Measurement of total and differential W^+W^- production cross sections in proton-proton collisions at $\sqrt{s}$ = 8 TeV with the ATLAS detector and limits on anomalous triple-gauge-boson couplings,
JHEP **09** (2016) 029, arXiv: 1603.01702 [hep-ex].

[84] K. Hagiwara, S. Ishihara, R. Szalapski and D. Zeppenfeld,
Low-energy effects of new interactions in the electroweak boson sector,
Phys. Rev. D **48** (1993) 2182.

[85] G. J. Feldman and R. D. Cousins,
A Unified approach to the classical statistical analysis of small signals,
Phys. Rev. D **57** (1998) 3873, arXiv: physics/9711021 [physics.data-an].

[86] ATLAS Collaboration, *ATLAS Computing Acknowledgements 2016-2017*,
ATL-GEN-PUB-2016-002, 2016, URL: https://cdsweb.cern.ch/record/2202407.

The ATLAS Collaboration

M. Aaboud[137d], G. Aad[88], B. Abbott[115], J. Abdallah[8], O. Abdinov[12], B. Abeloos[119], S.H. Abidi[161], O.S. AbouZeid[139], N.L. Abraham[151], H. Abramowicz[155], H. Abreu[154], R. Abreu[118], Y. Abulaiti[148a,148b], B.S. Acharya[167a,167b,a], S. Adachi[157], L. Adamczyk[41a], D.L. Adams[27], J. Adelman[110], M. Adersberger[102], T. Adye[133], A.A. Affolder[139], T. Agatonovic-Jovin[14], C. Agheorghiesei[28b], J.A. Aguilar-Saavedra[128a,128f], S.P. Ahlen[24], F. Ahmadov[68,b], G. Aielli[135a,135b], S. Akatsuka[71], H. Akerstedt[148a,148b], T.P.A. Åkesson[84], A.V. Akimov[98], G.L. Alberghi[22a,22b], J. Albert[172], M.J. Alconada Verzini[74], M. Aleksa[32], I.N. Aleksandrov[68], C. Alexa[28b], G. Alexander[155], T. Alexopoulos[10], M. Alhroob[115], B. Ali[130], M. Aliev[76a,76b], G. Alimonti[94a], J. Alison[33], S.P. Alkire[38], B.M.M. Allbrooke[151], B.W. Allen[118], P.P. Allport[19], A. Aloisio[106a,106b], A. Alonso[39], F. Alonso[74], C. Alpigiani[140], A.A. Alshehri[56], M. Alstaty[88], B. Alvarez Gonzalez[32], D. Álvarez Piqueras[170], M.G. Alviggi[106a,106b], B.T. Amadio[16], Y. Amaral Coutinho[26a], C. Amelung[25], D. Amidei[92], S.P. Amor Dos Santos[128a,128c], A. Amorim[128a,128b], S. Amoroso[32], G. Amundsen[25], C. Anastopoulos[141], L.S. Ancu[52], N. Andari[19], T. Andeen[11], C.F. Anders[60b], J.K. Anders[77], K.J. Anderson[33], A. Andreazza[94a,94b], V. Andrei[60a], S. Angelidakis[9], I. Angelozzi[109], A. Angerami[38], F. Anghinolfi[32], A.V. Anisenkov[111,c], N. Anjos[13], A. Annovi[126a,126b], C. Antel[60a], M. Antonelli[50], A. Antonov[100,*], D.J. Antrim[166], F. Anulli[134a], M. Aoki[69], L. Aperio Bella[32], G. Arabidze[93], Y. Arai[69], J.P. Araque[128a], V. Araujo Ferraz[26a], A.T.H. Arce[48], R.E. Ardell[80], F.A. Arduh[74], J-F. Arguin[97], S. Argyropoulos[66], M. Arik[20a], A.J. Armbruster[145], L.J. Armitage[79], O. Arnaez[32], H. Arnold[51], M. Arratia[30], O. Arslan[23], A. Artamonov[99], G. Artoni[122], S. Artz[86], S. Asai[157], N. Asbah[45], A. Ashkenazi[155], L. Asquith[151], K. Assamagan[27], R. Astalos[146a], M. Atkinson[169], N.B. Atlay[143], K. Augsten[130], G. Avolio[32], B. Axen[16], M.K. Ayoub[119], G. Azuelos[97,d], A.E. Baas[60a], M.J. Baca[19], H. Bachacou[138], K. Bachas[76a,76b], M. Backes[122], M. Backhaus[32], P. Bagiacchi[134a,134b], P. Bagnaia[134a,134b], J.T. Baines[133], M. Bajic[39], O.K. Baker[179], E.M. Baldin[111,c], P. Balek[175], T. Balestri[150], F. Balli[138], W.K. Balunas[124], E. Banas[42], Sw. Banerjee[176,e], A.A.E. Bannoura[178], L. Barak[32], E.L. Barberio[91], D. Barberis[53a,53b], M. Barbero[88], T. Barillari[103], M-S Barisits[32], T. Barklow[145], N. Barlow[30], S.L. Barnes[36c], B.M. Barnett[133], R.M. Barnett[16], Z. Barnovska-Blenessy[36a], A. Baroncelli[136a], G. Barone[25], A.J. Barr[122], L. Barranco Navarro[170], F. Barreiro[85], J. Barreiro Guimarães da Costa[35a], R. Bartoldus[145], A.E. Barton[75], P. Bartos[146a], A. Basalaev[125], A. Bassalat[119,f], R.L. Bates[56], S.J. Batista[161], J.R. Batley[30], M. Battaglia[139], M. Bauce[134a,134b], F. Bauer[138], H.S. Bawa[145,g], J.B. Beacham[113], M.D. Beattie[75], T. Beau[83], P.H. Beauchemin[165], P. Bechtle[23], H.P. Beck[18,h], K. Becker[122], M. Becker[86], M. Beckingham[173], C. Becot[112], A.J. Beddall[20e], A. Beddall[20b], V.A. Bednyakov[68], M. Bedognetti[109], C.P. Bee[150], T.A. Beermann[32], M. Begalli[26a], M. Begel[27], J.K. Behr[45], A.S. Bell[81], G. Bella[155], L. Bellagamba[22a], A. Bellerive[31], M. Bellomo[89], K. Belotskiy[100], O. Beltramello[32], N.L. Belyaev[100], O. Benary[155,*], D. Benchekroun[137a], M. Bender[102], K. Bendtz[148a,148b], N. Benekos[10], Y. Benhammou[155], E. Benhar Noccioli[179], J. Benitez[66], D.P. Benjamin[48], M. Benoit[52], J.R. Bensinger[25], S. Bentvelsen[109], L. Beresford[122], M. Beretta[50], D. Berge[109], E. Bergeaas Kuutmann[168], N. Berger[5], J. Beringer[16], S. Berlendis[58], N.R. Bernard[89], G. Bernardi[83], C. Bernius[112], F.U. Bernlochner[23], T. Berry[80], P. Berta[131], C. Bertella[86], G. Bertoli[148a,148b], F. Bertolucci[126a,126b], I.A. Bertram[75], C. Bertsche[45], D. Bertsche[115], G.J. Besjes[39], O. Bessidskaia Bylund[148a,148b], M. Bessner[45], N. Besson[138], C. Betancourt[51], A. Bethani[87], S. Bethke[103], A.J. Bevan[79], R.M. Bianchi[127], M. Bianco[32], O. Biebel[102], D. Biedermann[17], R. Bielski[87], N.V. Biesuz[126a,126b], M. Biglietti[136a], J. Bilbao De Mendizabal[52], T.R.V. Billoud[97], H. Bilokon[50], M. Bindi[57], A. Bingul[20b], C. Bini[134a,134b], S. Biondi[22a,22b], T. Bisanz[57], C. Bittrich[47], D.M. Bjergaard[48], C.W. Black[152], J.E. Black[145], K.M. Black[24], D. Blackburn[140], R.E. Blair[6], T. Blazek[146a], I. Bloch[45], C. Blocker[25], A. Blue[56], W. Blum[86,*], U. Blumenschein[79],

S. Blunier[34a], G.J. Bobbink[109], V.S. Bobrovnikov[111,c], S.S. Bocchetta[84], A. Bocci[48], C. Bock[102], M. Boehler[51], D. Boerner[178], D. Bogavac[102], A.G. Bogdanchikov[111], C. Bohm[148a], V. Boisvert[80], P. Bokan[168,i], T. Bold[41a], A.S. Boldyrev[101], M. Bomben[83], M. Bona[79], M. Boonekamp[138], A. Borisov[132], G. Borissov[75], J. Bortfeldt[32], D. Bortoletto[122], V. Bortolotto[62a,62b,62c], K. Bos[109], D. Boscherini[22a], M. Bosman[13], J.D. Bossio Sola[29], J. Boudreau[127], J. Bouffard[2], E.V. Bouhova-Thacker[75], D. Boumediene[37], C. Bourdarios[119], S.K. Boutle[56], A. Boveia[113], J. Boyd[32], I.R. Boyko[68], J. Bracinik[19], A. Brandt[8], G. Brandt[57], O. Brandt[60a], U. Bratzler[158], B. Brau[89], J.E. Brau[118], W.D. Breaden Madden[56], K. Brendlinger[45], A.J. Brennan[91], L. Brenner[109], R. Brenner[168], S. Bressler[175], D.L. Briglin[19], T.M. Bristow[49], D. Britton[56], D. Britzger[45], F.M. Brochu[30], I. Brock[23], R. Brock[93], G. Brooijmans[38], T. Brooks[80], W.K. Brooks[34b], J. Brosamer[16], E. Brost[110], J.H Broughton[19], P.A. Bruckman de Renstrom[42], D. Bruncko[146b], A. Bruni[22a], G. Bruni[22a], L.S. Bruni[109], BH Brunt[30], M. Bruschi[22a], N. Bruscino[23], P. Bryant[33], L. Bryngemark[84], T. Buanes[15], Q. Buat[144], P. Buchholz[143], A.G. Buckley[56], I.A. Budagov[68], F. Buehrer[51], M.K. Bugge[121], O. Bulekov[100], D. Bullock[8], H. Burckhart[32], S. Burdin[77], C.D. Burgard[51], A.M. Burger[5], B. Burghgrave[110], K. Burka[42], S. Burke[133], I. Burmeister[46], J.T.P. Burr[122], E. Busato[37], D. Büscher[51], V. Büscher[86], P. Bussey[56], J.M. Butler[24], C.M. Buttar[56], J.M. Butterworth[81], P. Butti[32], W. Buttinger[27], A. Buzatu[35c], A.R. Buzykaev[111,c], S. Cabrera Urbán[170], D. Caforio[130], V.M. Cairo[40a,40b], O. Cakir[4a], N. Calace[52], P. Calafiura[16], A. Calandri[88], G. Calderini[83], P. Calfayan[64], G. Callea[40a,40b], L.P. Caloba[26a], S. Calvente Lopez[85], D. Calvet[37], S. Calvet[37], T.P. Calvet[88], R. Camacho Toro[33], S. Camarda[32], P. Camarri[135a,135b], D. Cameron[121], R. Caminal Armadans[169], C. Camincher[58], S. Campana[32], M. Campanelli[81], A. Camplani[94a,94b], A. Campoverde[143], V. Canale[106a,106b], M. Cano Bret[36c], J. Cantero[116], T. Cao[155], M.D.M. Capeans Garrido[32], I. Caprini[28b], M. Caprini[28b], M. Capua[40a,40b], R.M. Carbone[38], R. Cardarelli[135a], F. Cardillo[51], I. Carli[131], T. Carli[32], G. Carlino[106a], B.T. Carlson[127], L. Carminati[94a,94b], R.M.D. Carney[148a,148b], S. Caron[108], E. Carquin[34b], G.D. Carrillo-Montoya[32], J. Carvalho[128a,128c], D. Casadei[19], M.P. Casado[13,j], M. Casolino[13], D.W. Casper[166], R. Castelijn[109], A. Castelli[109], V. Castillo Gimenez[170], N.F. Castro[128a,k], A. Catinaccio[32], J.R. Catmore[121], A. Cattai[32], J. Caudron[23], V. Cavaliere[169], E. Cavallaro[13], D. Cavalli[94a], M. Cavalli-Sforza[13], V. Cavasinni[126a,126b], E. Celebi[20a], F. Ceradini[136a,136b], L. Cerda Alberich[170], A.S. Cerqueira[26b], A. Cerri[151], L. Cerrito[135a,135b], F. Cerutti[16], A. Cervelli[18], S.A. Cetin[20d], A. Chafaq[137a], D. Chakraborty[110], S.K. Chan[59], W.S. Chan[109], Y.L. Chan[62a], P. Chang[169], J.D. Chapman[30], D.G. Charlton[19], A. Chatterjee[52], C.C. Chau[161], C.A. Chavez Barajas[151], S. Che[113], S. Cheatham[167a,167c], A. Chegwidden[93], S. Chekanov[6], S.V. Chekulaev[163a], G.A. Chelkov[68,l], M.A. Chelstowska[32], C. Chen[67], H. Chen[27], S. Chen[35b], S. Chen[157], X. Chen[35c,m], Y. Chen[70], H.C. Cheng[92], H.J. Cheng[35a], Y. Cheng[33], A. Cheplakov[68], E. Cheremushkina[132], R. Cherkaoui El Moursli[137e], V. Chernyatin[27,*], E. Cheu[7], L. Chevalier[138], V. Chiarella[50], G. Chiarelli[126a,126b], G. Chiodini[76a], A.S. Chisholm[32], A. Chitan[28b], Y.H. Chiu[172], M.V. Chizhov[68], K. Choi[64], A.R. Chomont[37], S. Chouridou[9], B.K.B. Chow[102], V. Christodoulou[81], D. Chromek-Burckhart[32], M.C. Chu[62a], J. Chudoba[129], A.J. Chuinard[90], J.J. Chwastowski[42], L. Chytka[117], A.K. Ciftci[4a], D. Cinca[46], V. Cindro[78], I.A. Cioara[23], C. Ciocca[22a,22b], A. Ciocio[16], F. Cirotto[106a,106b], Z.H. Citron[175], M. Citterio[94a], M. Ciubancan[28b], A. Clark[52], B.L. Clark[59], M.R. Clark[38], P.J. Clark[49], R.N. Clarke[16], C. Clement[148a,148b], Y. Coadou[88], M. Cobal[167a,167c], A. Coccaro[52], J. Cochran[67], L. Colasurdo[108], B. Cole[38], A.P. Colijn[109], J. Collot[58], T. Colombo[166], P. Conde Muiño[128a,128b], E. Coniavitis[51], S.H. Connell[147b], I.A. Connelly[87], V. Consorti[51], S. Constantinescu[28b], G. Conti[32], F. Conventi[106a,n], M. Cooke[16], B.D. Cooper[81], A.M. Cooper-Sarkar[122], F. Cormier[171], K.J.R. Cormier[161], T. Cornelissen[178], M. Corradi[134a,134b], F. Corriveau[90,o], A. Cortes-Gonzalez[32], G. Cortiana[103], G. Costa[94a], M.J. Costa[170], D. Costanzo[141], G. Cottin[30], G. Cowan[80], B.E. Cox[87], K. Cranmer[112], S.J. Crawley[56], R.A. Creager[124], G. Cree[31], S. Crépé-Renaudin[58], F. Crescioli[83], W.A. Cribbs[148a,148b], M. Crispin Ortuzar[122], M. Cristinziani[23],

V. Croft[108], G. Crosetti[40a,40b], A. Cueto[85], T. Cuhadar Donszelmann[141], J. Cummings[179], M. Curatolo[50], J. Cúth[86], H. Czirr[143], P. Czodrowski[32], G. D'amen[22a,22b], S. D'Auria[56], M. D'Onofrio[77], M.J. Da Cunha Sargedas De Sousa[128a,128b], C. Da Via[87], W. Dabrowski[41a], T. Dado[146a], T. Dai[92], O. Dale[15], F. Dallaire[97], C. Dallapiccola[89], M. Dam[39], J.R. Dandoy[124], N.P. Dang[51], A.C. Daniells[19], N.S. Dann[87], M. Danninger[171], M. Dano Hoffmann[138], V. Dao[150], G. Darbo[53a], S. Darmora[8], J. Dassoulas[3], A. Dattagupta[118], T. Daubney[45], W. Davey[23], C. David[45], T. Davidek[131], M. Davies[155], P. Davison[81], E. Dawe[91], I. Dawson[141], K. De[8], R. de Asmundis[106a], A. De Benedetti[115], S. De Castro[22a,22b], S. De Cecco[83], N. De Groot[108], P. de Jong[109], H. De la Torre[93], F. De Lorenzi[67], A. De Maria[57], D. De Pedis[134a], A. De Salvo[134a], U. De Sanctis[151], A. De Santo[151], K. De Vasconcelos Corga[88], J.B. De Vivie De Regie[119], W.J. Dearnaley[75], R. Debbe[27], C. Debenedetti[139], D.V. Dedovich[68], N. Dehghanian[3], I. Deigaard[109], M. Del Gaudio[40a,40b], J. Del Peso[85], T. Del Prete[126a,126b], D. Delgove[119], F. Deliot[138], C.M. Delitzsch[52], A. Dell'Acqua[32], L. Dell'Asta[24], M. Dell'Orso[126a,126b], M. Della Pietra[106a,106b], D. della Volpe[52], M. Delmastro[5], P.A. Delsart[58], D.A. DeMarco[161], S. Demers[179], M. Demichev[68], A. Demilly[83], S.P. Denisov[132], D. Denysiuk[138], D. Derendarz[42], J.E. Derkaoui[137d], F. Derue[83], P. Dervan[77], K. Desch[23], C. Deterre[45], K. Dette[46], P.O. Deviveiros[32], A. Dewhurst[133], S. Dhaliwal[25], A. Di Ciaccio[135a,135b], L. Di Ciaccio[5], W.K. Di Clemente[124], C. Di Donato[106a,106b], A. Di Girolamo[32], B. Di Girolamo[32], B. Di Micco[136a,136b], R. Di Nardo[32], K.F. Di Petrillo[59], A. Di Simone[51], R. Di Sipio[161], D. Di Valentino[31], C. Diaconu[88], M. Diamond[161], F.A. Dias[49], M.A. Diaz[34a], E.B. Diehl[92], J. Dietrich[17], S. Díez Cornell[45], A. Dimitrievska[14], J. Dingfelder[23], P. Dita[28b], S. Dita[28b], F. Dittus[32], F. Djama[88], T. Djobava[54b], J.I. Djuvsland[60a], M.A.B. do Vale[26c], D. Dobos[32], M. Dobre[28b], C. Doglioni[84], J. Dolejsi[131], Z. Dolezal[131], M. Donadelli[26d], S. Donati[126a,126b], P. Dondero[123a,123b], J. Donini[37], J. Dopke[133], A. Doria[106a], M.T. Dova[74], A.T. Doyle[56], E. Drechsler[57], M. Dris[10], Y. Du[36b], J. Duarte-Campderros[155], E. Duchovni[175], G. Duckeck[102], O.A. Ducu[97,p], D. Duda[109], A. Dudarev[32], A.Chr. Dudder[86], E.M. Duffield[16], L. Duflot[119], M. Dührssen[32], M. Dumancic[175], A.E. Dumitriu[28b], A.K. Duncan[56], M. Dunford[60a], H. Duran Yildiz[4a], M. Düren[55], A. Durglishvili[54b], D. Duschinger[47], B. Dutta[45], M. Dyndal[45], C. Eckardt[45], K.M. Ecker[103], R.C. Edgar[92], T. Eifert[32], G. Eigen[15], K. Einsweiler[16], T. Ekelof[168], M. El Kacimi[137c], V. Ellajosyula[88], M. Ellert[168], S. Elles[5], F. Ellinghaus[178], A.A. Elliot[172], N. Ellis[32], J. Elmsheuser[27], M. Elsing[32], D. Emeliyanov[133], Y. Enari[157], O.C. Endner[86], J.S. Ennis[173], J. Erdmann[46], A. Ereditato[18], G. Ernis[178], M. Ernst[27], S. Errede[169], E. Ertel[86], M. Escalier[119], H. Esch[46], C. Escobar[127], B. Esposito[50], A.I. Etienvre[138], E. Etzion[155], H. Evans[64], A. Ezhilov[125], F. Fabbri[22a,22b], L. Fabbri[22a,22b], G. Facini[33], R.M. Fakhrutdinov[132], S. Falciano[134a], R.J. Falla[81], J. Faltova[32], Y. Fang[35a], M. Fanti[94a,94b], A. Farbin[8], A. Farilla[136a], C. Farina[127], E.M. Farina[123a,123b], T. Farooque[93], S. Farrell[16], S.M. Farrington[173], P. Farthouat[32], F. Fassi[137e], P. Fassnacht[32], D. Fassouliotis[9], M. Faucci Giannelli[80], A. Favareto[53a,53b], W.J. Fawcett[122], L. Fayard[119], O.L. Fedin[125,q], W. Fedorko[171], S. Feigl[121], L. Feligioni[88], C. Feng[36b], E.J. Feng[32], H. Feng[92], A.B. Fenyuk[132], L. Feremenga[8], P. Fernandez Martinez[170], S. Fernandez Perez[13], J. Ferrando[45], A. Ferrari[168], P. Ferrari[109], R. Ferrari[123a], D.E. Ferreira de Lima[60b], A. Ferrer[170], D. Ferrere[52], C. Ferretti[92], F. Fiedler[86], A. Filipčič[78], M. Filipuzzi[45], F. Filthaut[108], M. Fincke-Keeler[172], K.D. Finelli[152], M.C.N. Fiolhais[128a,128c,r], L. Fiorini[170], A. Fischer[2], C. Fischer[13], J. Fischer[178], W.C. Fisher[93], N. Flaschel[45], I. Fleck[143], P. Fleischmann[92], R.R.M. Fletcher[124], T. Flick[178], B.M. Flierl[102], L.R. Flores Castillo[62a], M.J. Flowerdew[103], G.T. Forcolin[87], A. Formica[138], A. Forti[87], A.G. Foster[19], D. Fournier[119], H. Fox[75], S. Fracchia[13], P. Francavilla[83], M. Franchini[22a,22b], D. Francis[32], L. Franconi[121], M. Franklin[59], M. Frate[166], M. Fraternali[123a,123b], D. Freeborn[81], S.M. Fressard-Batraneanu[32], B. Freund[97], D. Froidevaux[32], J.A. Frost[122], C. Fukunaga[158], E. Fullana Torregrosa[86], T. Fusayasu[104], J. Fuster[170], C. Gabaldon[58], O. Gabizon[154], A. Gabrielli[22a,22b], A. Gabrielli[16], G.P. Gach[41a], S. Gadatsch[32], S. Gadomski[80], G. Gagliardi[53a,53b], L.G. Gagnon[97], P. Gagnon[64], C. Galea[108], B. Galhardo[128a,128c],

E.J. Gallas[122], B.J. Gallop[133], P. Gallus[130], G. Galster[39], K.K. Gan[113], S. Ganguly[37], J. Gao[36a], Y. Gao[77], Y.S. Gao[145,g], F.M. Garay Walls[49], C. García[170], J.E. García Navarro[170], M. Garcia-Sciveres[16], R.W. Gardner[33], N. Garelli[145], V. Garonne[121], A. Gascon Bravo[45], K. Gasnikova[45], C. Gatti[50], A. Gaudiello[53a,53b], G. Gaudio[123a], I.L. Gavrilenko[98], C. Gay[171], G. Gaycken[23], E.N. Gazis[10], C.N.P. Gee[133], M. Geisen[86], M.P. Geisler[60a], K. Gellerstedt[148a,148b], C. Gemme[53a], M.H. Genest[58], C. Geng[36a,s], S. Gentile[134a,134b], C. Gentsos[156], S. George[80], D. Gerbaudo[13], A. Gershon[155], S. Ghasemi[143], M. Ghneimat[23], B. Giacobbe[22a], S. Giagu[134a,134b], P. Giannetti[126a,126b], S.M. Gibson[80], M. Gignac[171], M. Gilchriese[16], D. Gillberg[31], G. Gilles[178], D.M. Gingrich[3,d], N. Giokaris[9,*], M.P. Giordani[167a,167c], F.M. Giorgi[22a], P.F. Giraud[138], P. Giromini[59], D. Giugni[94a], F. Giuli[122], C. Giuliani[103], M. Giulini[60b], B.K. Gjelsten[121], S. Gkaitatzis[156], I. Gkialas[9], E.L. Gkougkousis[139], L.K. Gladilin[101], C. Glasman[85], J. Glatzer[13], P.C.F. Glaysher[45], A. Glazov[45], M. Goblirsch-Kolb[25], J. Godlewski[42], S. Goldfarb[91], T. Golling[52], D. Golubkov[132], A. Gomes[128a,128b,128d], R. Gonçalo[128a], R. Goncalves Gama[26a], J. Goncalves Pinto Firmino Da Costa[138], G. Gonella[51], L. Gonella[19], A. Gongadze[68], S. González de la Hoz[170], S. Gonzalez-Sevilla[52], L. Goossens[32], P.A. Gorbounov[99], H.A. Gordon[27], I. Gorelov[107], B. Gorini[32], E. Gorini[76a,76b], A. Gorišek[78], A.T. Goshaw[48], C. Gössling[46], M.I. Gostkin[68], C.R. Goudet[119], D. Goujdami[137c], A.G. Goussiou[140], N. Govender[147b,t], E. Gozani[154], L. Graber[57], I. Grabowska-Bold[41a], P.O.J. Gradin[58], J. Gramling[52], E. Gramstad[121], S. Grancagnolo[17], V. Gratchev[125], P.M. Gravila[28f], H.M. Gray[32], Z.D. Greenwood[82,u], C. Grefe[23], K. Gregersen[81], I.M. Gregor[45], P. Grenier[145], K. Grevtsov[5], J. Griffiths[8], A.A. Grillo[139], K. Grimm[75], S. Grinstein[13,v], Ph. Gris[37], J.-F. Grivaz[119], S. Groh[86], E. Gross[175], J. Grosse-Knetter[57], G.C. Grossi[82], Z.J. Grout[81], L. Guan[92], W. Guan[176], J. Guenther[65], F. Guescini[163a], D. Guest[166], O. Gueta[155], B. Gui[113], E. Guido[53a,53b], T. Guillemin[5], S. Guindon[2], U. Gul[56], C. Gumpert[32], J. Guo[36c], W. Guo[92], Y. Guo[36a], R. Gupta[43], S. Gupta[122], G. Gustavino[134a,134b], P. Gutierrez[115], N.G. Gutierrez Ortiz[81], C. Gutschow[81], C. Guyot[138], M.P. Guzik[41a], C. Gwenlan[122], C.B. Gwilliam[77], A. Haas[112], C. Haber[16], H.K. Hadavand[8], A. Hadef[88], S. Hageböck[23], M. Hagihara[164], H. Hakobyan[180,*], M. Haleem[45], J. Haley[116], G. Halladjian[93], G.D. Hallewell[88], K. Hamacher[178], P. Hamal[117], K. Hamano[172], A. Hamilton[147a], G.N. Hamity[141], P.G. Hamnett[45], L. Han[36a], S. Han[35a], K. Hanagaki[69,w], K. Hanawa[157], M. Hance[139], B. Haney[124], P. Hanke[60a], R. Hanna[138], J.B. Hansen[39], J.D. Hansen[39], M.C. Hansen[23], P.H. Hansen[39], K. Hara[164], A.S. Hard[176], T. Harenberg[178], F. Hariri[119], S. Harkusha[95], R.D. Harrington[49], P.F. Harrison[173], F. Hartjes[109], N.M. Hartmann[102], M. Hasegawa[70], Y. Hasegawa[142], A. Hasib[49], S. Hassani[138], S. Haug[18], R. Hauser[93], L. Hauswald[47], L.B. Havener[38], M. Havranek[130], C.M. Hawkes[19], R.J. Hawkings[32], D. Hayakawa[159], D. Hayden[93], C.P. Hays[122], J.M. Hays[79], H.S. Hayward[77], S.J. Haywood[133], S.J. Head[19], T. Heck[86], V. Hedberg[84], L. Heelan[8], K.K. Heidegger[51], S. Heim[45], T. Heim[16], B. Heinemann[45,x], J.J. Heinrich[102], L. Heinrich[112], C. Heinz[55], J. Hejbal[129], L. Helary[32], A. Held[171], S. Hellman[148a,148b], C. Helsens[32], J. Henderson[122], R.C.W. Henderson[75], Y. Heng[176], S. Henkelmann[171], A.M. Henriques Correia[32], S. Henrot-Versille[119], G.H. Herbert[17], H. Herde[25], V. Herget[177], Y. Hernández Jiménez[147c], G. Herten[51], R. Hertenberger[102], L. Hervas[32], T.C. Herwig[124], G.G. Hesketh[81], N.P. Hessey[163a], J.W. Hetherly[43], S. Higashino[69], E. Higón-Rodriguez[170], E. Hill[172], J.C. Hill[30], K.H. Hiller[45], S.J. Hillier[19], I. Hinchliffe[16], M. Hirose[51], D. Hirschbuehl[178], B. Hiti[78], O. Hladik[129], X. Hoad[49], J. Hobbs[150], N. Hod[163a], M.C. Hodgkinson[141], P. Hodgson[141], A. Hoecker[32], M.R. Hoeferkamp[107], F. Hoenig[102], D. Hohn[23], T.R. Holmes[16], M. Homann[46], S. Honda[164], T. Honda[69], T.M. Hong[127], B.H. Hooberman[169], W.H. Hopkins[118], Y. Horii[105], A.J. Horton[144], J-Y. Hostachy[58], S. Hou[153], A. Hoummada[137a], J. Howarth[45], J. Hoya[74], M. Hrabovsky[117], I. Hristova[17], J. Hrivnac[119], T. Hryn'ova[5], A. Hrynevich[96], P.J. Hsu[63], S.-C. Hsu[140], Q. Hu[36a], S. Hu[36c], Y. Huang[35a], Z. Hubacek[130], F. Hubaut[88], F. Huegging[23], T.B. Huffman[122], E.W. Hughes[38], G. Hughes[75], M. Huhtinen[32], P. Huo[150], N. Huseynov[68,b], J. Huston[93], J. Huth[59], G. Iacobucci[52], G. Iakovidis[27], I. Ibragimov[143], L. Iconomidou-Fayard[119], P. Iengo[32], O. Igonkina[109,y],

T. Iizawa[174], Y. Ikegami[69], M. Ikeno[69], Y. Ilchenko[11,z], D. Iliadis[156], N. Ilic[145], G. Introzzi[123a,123b], P. Ioannou[9,*], M. Iodice[136a], K. Iordanidou[38], V. Ippolito[59], N. Ishijima[120], M. Ishino[157], M. Ishitsuka[159], C. Issever[122], S. Istin[20a], F. Ito[164], J.M. Iturbe Ponce[87], R. Iuppa[162a,162b], H. Iwasaki[69], J.M. Izen[44], V. Izzo[106a], S. Jabbar[3], P. Jackson[1], V. Jain[2], K.B. Jakobi[86], K. Jakobs[51], S. Jakobsen[32], T. Jakoubek[129], D.O. Jamin[116], D.K. Jana[82], R. Jansky[65], J. Janssen[23], M. Janus[57], P.A. Janus[41a], G. Jarlskog[84], N. Javadov[68,b], T. Javůrek[51], M. Javurkova[51], F. Jeanneau[138], L. Jeanty[16], J. Jejelava[54a,aa], A. Jelinskas[173], P. Jenni[51,ab], C. Jeske[173], S. Jézéquel[5], H. Ji[176], J. Jia[150], H. Jiang[67], Y. Jiang[36a], Z. Jiang[145], S. Jiggins[81], J. Jimenez Pena[170], S. Jin[35a], A. Jinaru[28b], O. Jinnouchi[159], H. Jivan[147c], P. Johansson[141], K.A. Johns[7], C.A. Johnson[64], W.J. Johnson[140], K. Jon-And[148a,148b], R.W.L. Jones[75], S. Jones[7], T.J. Jones[77], J. Jongmanns[60a], P.M. Jorge[128a,128b], J. Jovicevic[163a], X. Ju[176], A. Juste Rozas[13,v], M.K. Köhler[175], A. Kaczmarska[42], M. Kado[119], H. Kagan[113], M. Kagan[145], S.J. Kahn[88], T. Kaji[174], E. Kajomovitz[48], C.W. Kalderon[84], A. Kaluza[86], S. Kama[43], A. Kamenshchikov[132], N. Kanaya[157], S. Kaneti[30], L. Kanjir[78], V.A. Kantserov[100], J. Kanzaki[69], B. Kaplan[112], L.S. Kaplan[176], D. Kar[147c], K. Karakostas[10], N. Karastathis[10], M.J. Kareem[57], E. Karentzos[10], S.N. Karpov[68], Z.M. Karpova[68], K. Karthik[112], V. Kartvelishvili[75], A.N. Karyukhin[132], K. Kasahara[164], L. Kashif[176], R.D. Kass[113], A. Kastanas[149], Y. Kataoka[157], C. Kato[157], A. Katre[52], J. Katzy[45], K. Kawade[105], K. Kawagoe[73], T. Kawamoto[157], G. Kawamura[57], E.F. Kay[77], V.F. Kazanin[111,c], R. Keeler[172], R. Kehoe[43], J.S. Keller[45], J.J. Kempster[80], H. Keoshkerian[161], O. Kepka[129], B.P. Kerševan[78], S. Kersten[178], R.A. Keyes[90], M. Khader[169], F. Khalil-zada[12], A. Khanov[116], A.G. Kharlamov[111,c], T. Kharlamova[111,c], A. Khodinov[160], T.J. Khoo[52], V. Khovanskiy[99,*], E. Khramov[68], J. Khubua[54b,ac], S. Kido[70], C.R. Kilby[80], H.Y. Kim[8], S.H. Kim[164], Y.K. Kim[33], N. Kimura[156], O.M. Kind[17], B.T. King[77], D. Kirchmeier[47], J. Kirk[133], A.E. Kiryunin[103], T. Kishimoto[157], D. Kisielewska[41a], K. Kiuchi[164], O. Kivernyk[138], E. Kladiva[146b], T. Klapdor-Kleingrothaus[51], M.H. Klein[38], M. Klein[77], U. Klein[77], K. Kleinknecht[86], P. Klimek[110], A. Klimentov[27], R. Klingenberg[46], T. Klioutchnikova[32], E.-E. Kluge[60a], P. Kluit[109], S. Kluth[103], J. Knapik[42], E. Kneringer[65], E.B.F.G. Knoops[88], A. Knue[103], A. Kobayashi[157], D. Kobayashi[159], T. Kobayashi[157], M. Kobel[47], M. Kocian[145], P. Kodys[131], T. Koffas[31], E. Koffeman[109], N.M. Köhler[103], T. Koi[145], M. Kolb[60b], I. Koletsou[5], A.A. Komar[98,*], Y. Komori[157], T. Kondo[69], N. Kondrashova[36c], K. Köneke[51], A.C. König[108], T. Kono[69,ad], R. Konoplich[112,ae], N. Konstantinidis[81], R. Kopeliansky[64], S. Koperny[41a], A.K. Kopp[51], K. Korcyl[42], K. Kordas[156], A. Korn[81], A.A. Korol[111,c], I. Korolkov[13], E.V. Korolkova[141], O. Kortner[103], S. Kortner[103], T. Kosek[131], V.V. Kostyukhin[23], A. Kotwal[48], A. Koulouris[10], A. Kourkoumeli-Charalampidi[123a,123b], C. Kourkoumelis[9], V. Kouskoura[27], A.B. Kowalewska[42], R. Kowalewski[172], T.Z. Kowalski[41a], C. Kozakai[157], W. Kozanecki[138], A.S. Kozhin[132], V.A. Kramarenko[101], G. Kramberger[78], D. Krasnopevtsev[100], M.W. Krasny[83], A. Krasznahorkay[32], D. Krauss[103], A. Kravchenko[27], J.A. Kremer[41a], M. Kretz[60c], J. Kretzschmar[77], K. Kreutzfeldt[55], P. Krieger[161], K. Krizka[33], K. Kroeninger[46], H. Kroha[103], J. Kroll[124], J. Kroseberg[23], J. Krstic[14], U. Kruchonak[68], H. Krüger[23], N. Krumnack[67], M.C. Kruse[48], M. Kruskal[24], T. Kubota[91], H. Kucuk[81], S. Kuday[4b], J.T. Kuechler[178], S. Kuehn[51], A. Kugel[60c], F. Kuger[177], T. Kuhl[45], V. Kukhtin[68], R. Kukla[88], Y. Kulchitsky[95], S. Kuleshov[34b], Y.P. Kulinich[169], M. Kuna[134a,134b], T. Kunigo[71], A. Kupco[129], O. Kuprash[155], H. Kurashige[70], L.L. Kurchaninov[163a], Y.A. Kurochkin[95], M.G. Kurth[35a], V. Kus[129], E.S. Kuwertz[172], M. Kuze[159], J. Kvita[117], T. Kwan[172], D. Kyriazopoulos[141], A. La Rosa[103], J.L. La Rosa Navarro[26d], L. La Rotonda[40a,40b], C. Lacasta[170], F. Lacava[134a,134b], J. Lacey[45], H. Lacker[17], D. Lacour[83], E. Ladygin[68], R. Lafaye[5], B. Laforge[83], T. Lagouri[179], S. Lai[57], S. Lammers[64], W. Lampl[7], E. Lançon[27], U. Landgraf[51], M.P.J. Landon[79], M.C. Lanfermann[52], V.S. Lang[60a], J.C. Lange[13], A.J. Lankford[166], F. Lanni[27], K. Lantzsch[23], A. Lanza[123a], A. Lapertosa[53a,53b], S. Laplace[83], J.F. Laporte[138], T. Lari[94a], F. Lasagni Manghi[22a,22b], M. Lassnig[32], P. Laurelli[50], W. Lavrijsen[16], A.T. Law[139], P. Laycock[77], T. Lazovich[59], M. Lazzaroni[94a,94b], B. Le[91], O. Le Dortz[83], E. Le Guirriec[88], E.P. Le Quilleuc[138], M. LeBlanc[172], T. LeCompte[6], F. Ledroit-Guillon[58], C.A. Lee[27], S.C. Lee[153],

L. Lee[1], B. Lefebvre[90], G. Lefebvre[83], M. Lefebvre[172], F. Legger[102], C. Leggett[16], A. Lehan[77], G. Lehmann Miotto[32], X. Lei[7], W.A. Leight[45], A.G. Leister[179], M.A.L. Leite[26d], R. Leitner[131], D. Lellouch[175], B. Lemmer[57], K.J.C. Leney[81], T. Lenz[23], B. Lenzi[32], R. Leone[7], S. Leone[126a,126b], C. Leonidopoulos[49], G. Lerner[151], C. Leroy[97], A.A.J. Lesage[138], C.G. Lester[30], M. Levchenko[125], J. Levêque[5], D. Levin[92], L.J. Levinson[175], M. Levy[19], D. Lewis[79], M. Leyton[44], B. Li[36a,s], C. Li[36a], H. Li[150], L. Li[48], L. Li[36c], Q. Li[35a], S. Li[48], X. Li[36c], Y. Li[143], Z. Liang[35a], B. Liberti[135a], A. Liblong[161], K. Lie[169], J. Liebal[23], W. Liebig[15], A. Limosani[152], S.C. Lin[153,af], T.H. Lin[86], B.E. Lindquist[150], A.E. Lionti[52], E. Lipeles[124], A. Lipniacka[15], M. Lisovyi[60b], T.M. Liss[169], A. Lister[171], A.M. Litke[139], B. Liu[153,ag], H. Liu[92], H. Liu[27], J. Liu[36b], J.B. Liu[36a], K. Liu[88], L. Liu[169], M. Liu[36a], Y.L. Liu[36a], Y. Liu[36a], M. Livan[123a,123b], A. Lleres[58], J. Llorente Merino[35a], S.L. Lloyd[79], C.Y. Lo[62b], F. Lo Sterzo[153], E.M. Lobodzinska[45], P. Loch[7], F.K. Loebinger[87], K.M. Loew[25], A. Loginov[179,*], T. Lohse[17], K. Lohwasser[45], M. Lokajicek[129], B.A. Long[24], J.D. Long[169], R.E. Long[75], L. Longo[76a,76b], K.A. Looper[113], J.A. Lopez[34b], D. Lopez Mateos[59], I. Lopez Paz[13], A. Lopez Solis[83], J. Lorenz[102], N. Lorenzo Martinez[64], M. Losada[21], P.J. Lösel[102], X. Lou[35a], A. Lounis[119], J. Love[6], P.A. Love[75], H. Lu[62a], N. Lu[92], Y.J. Lu[63], H.J. Lubatti[140], C. Luci[134a,134b], A. Lucotte[58], C. Luedtke[51], F. Luehring[64], W. Lukas[65], L. Luminari[134a], O. Lundberg[148a,148b], B. Lund-Jensen[149], P.M. Luzi[83], D. Lynn[27], R. Lysak[129], E. Lytken[84], V. Lyubushkin[68], H. Ma[27], L.L. Ma[36b], Y. Ma[36b], G. Maccarrone[50], A. Macchiolo[103], C.M. Macdonald[141], B. Maček[78], J. Machado Miguens[124,128b], D. Madaffari[88], R. Madar[37], H.J. Maddocks[168], W.F. Mader[47], A. Madsen[45], J. Maeda[70], S. Maeland[15], T. Maeno[27], A. Maevskiy[101], E. Magradze[57], J. Mahlstedt[109], C. Maiani[119], C. Maidantchik[26a], A.A. Maier[103], T. Maier[102], A. Maio[128a,128b,128d], S. Majewski[118], Y. Makida[69], N. Makovec[119], B. Malaescu[83], Pa. Malecki[42], V.P. Maleev[125], F. Malek[58], U. Mallik[66], D. Malon[6], C. Malone[30], S. Maltezos[10], S. Malyukov[32], J. Mamuzic[170], G. Mancini[50], L. Mandelli[94a], I. Mandić[78], J. Maneira[128a,128b], L. Manhaes de Andrade Filho[26b], J. Manjarres Ramos[163b], A. Mann[102], A. Manousos[32], B. Mansoulie[138], J.D. Mansour[35a], R. Mantifel[90], M. Mantoani[57], S. Manzoni[94a,94b], L. Mapelli[32], G. Marceca[29], L. March[52], G. Marchiori[83], M. Marcisovsky[129], M. Marjanovic[37], D.E. Marley[92], F. Marroquim[26a], S.P. Marsden[87], Z. Marshall[16], M.U.F Martensson[168], S. Marti-Garcia[170], C.B. Martin[113], T.A. Martin[173], V.J. Martin[49], B. Martin dit Latour[15], M. Martinez[13,v], V.I. Martinez Outschoorn[169], S. Martin-Haugh[133], V.S. Martoiu[28b], A.C. Martyniuk[81], A. Marzin[115], L. Masetti[86], T. Mashimo[157], R. Mashinistov[98], J. Masik[87], A.L. Maslennikov[111,c], L. Massa[135a,135b], P. Mastrandrea[5], A. Mastroberardino[40a,40b], T. Masubuchi[157], P. Mättig[178], J. Maurer[28b], S.J. Maxfield[77], D.A. Maximov[111,c], R. Mazini[153], I. Maznas[156], S.M. Mazza[94a,94b], N.C. Mc Fadden[107], G. Mc Goldrick[161], S.P. Mc Kee[92], A. McCarn[92], R.L. McCarthy[150], T.G. McCarthy[103], L.I. McClymont[81], E.F. McDonald[91], J.A. Mcfayden[81], G. Mchedlidze[57], S.J. McMahon[133], P.C. McNamara[91], R.A. McPherson[172,o], S. Meehan[140], T.J. Megy[51], S. Mehlhase[102], A. Mehta[77], T. Meideck[58], K. Meier[60a], C. Meineck[102], B. Meirose[44], D. Melini[170,ah], B.R. Mellado Garcia[147c], M. Melo[146a], F. Meloni[18], S.B. Menary[87], L. Meng[77], X.T. Meng[92], A. Mengarelli[22a,22b], S. Menke[103], E. Meoni[165], S. Mergelmeyer[17], P. Mermod[52], L. Merola[106a,106b], C. Meroni[94a], F.S. Merritt[33], A. Messina[134a,134b], J. Metcalfe[6], A.S. Mete[166], C. Meyer[124], J-P. Meyer[138], J. Meyer[109], H. Meyer Zu Theenhausen[60a], F. Miano[151], R.P. Middleton[133], S. Miglioranzi[53a,53b], L. Mijović[49], G. Mikenberg[175], M. Mikestikova[129], M. Mikuž[78], M. Milesi[91], A. Milic[27], D.W. Miller[33], C. Mills[49], A. Milov[175], D.A. Milstead[148a,148b], A.A. Minaenko[132], Y. Minami[157], I.A. Minashvili[68], A.I. Mincer[112], B. Mindur[41a], M. Mineev[68], Y. Minegishi[157], Y. Ming[176], L.M. Mir[13], K.P. Mistry[124], T. Mitani[174], J. Mitrevski[102], V.A. Mitsou[170], A. Miucci[18], P.S. Miyagawa[141], A. Mizukami[69], J.U. Mjörnmark[84], M. Mlynarikova[131], T. Moa[148a,148b], K. Mochizuki[97], P. Mogg[51], S. Mohapatra[38], S. Molander[148a,148b], R. Moles-Valls[23], R. Monden[71], M.C. Mondragon[93], K. Mönig[45], J. Monk[39], E. Monnier[88], A. Montalbano[150], J. Montejo Berlingen[32], F. Monticelli[74], S. Monzani[94a,94b], R.W. Moore[3],

N. Morange[119], D. Moreno[21], M. Moreno Llácer[57], P. Morettini[53a], S. Morgenstern[32], D. Mori[144], T. Mori[157], M. Morii[59], M. Morinaga[157], V. Morisbak[121], A.K. Morley[152], G. Mornacchi[32], J.D. Morris[79], L. Morvaj[150], P. Moschovakos[10], M. Mosidze[54b], H.J. Moss[141], J. Moss[145,ai], K. Motohashi[159], R. Mount[145], E. Mountricha[27], E.J.W. Moyse[89], S. Muanza[88], R.D. Mudd[19], F. Mueller[103], J. Mueller[127], R.S.P. Mueller[102], D. Muenstermann[75], P. Mullen[56], G.A. Mullier[18], F.J. Munoz Sanchez[87], W.J. Murray[173,133], H. Musheghyan[57], M. Muškinja[78], A.G. Myagkov[132,aj], M. Myska[130], B.P. Nachman[16], O. Nackenhorst[52], K. Nagai[122], R. Nagai[69,ad], K. Nagano[69], Y. Nagasaka[61], K. Nagata[164], M. Nagel[51], E. Nagy[88], A.M. Nairz[32], Y. Nakahama[105], K. Nakamura[69], T. Nakamura[157], I. Nakano[114], R.F. Naranjo Garcia[45], R. Narayan[11], D.I. Narrias Villar[60a], I. Naryshkin[125], T. Naumann[45], G. Navarro[21], R. Nayyar[7], H.A. Neal[92], P.Yu. Nechaeva[98], T.J. Neep[138], A. Negri[123a,123b], M. Negrini[22a], S. Nektarijevic[108], C. Nellist[119], A. Nelson[166], S. Nemecek[129], P. Nemethy[112], A.A. Nepomuceno[26a], M. Nessi[32,ak], M.S. Neubauer[169], M. Neumann[178], R.M. Neves[112], P. Nevski[27], P.R. Newman[19], T.Y. Ng[62c], T. Nguyen Manh[97], R.B. Nickerson[122], R. Nicolaidou[138], J. Nielsen[139], V. Nikolaenko[132,aj], I. Nikolic-Audit[83], K. Nikolopoulos[19], J.K. Nilsen[121], P. Nilsson[27], Y. Ninomiya[157], A. Nisati[134a], N. Nishu[35c], R. Nisius[103], T. Nobe[157], Y. Noguchi[71], M. Nomachi[120], I. Nomidis[31], M.A. Nomura[27], T. Nooney[79], M. Nordberg[32], N. Norjoharuddeen[122], O. Novgorodova[47], S. Nowak[103], M. Nozaki[69], L. Nozka[117], K. Ntekas[166], E. Nurse[81], F. Nuti[91], D.C. O'Neil[144], A.A. O'Rourke[45], V. O'Shea[56], F.G. Oakham[31,d], H. Oberlack[103], T. Obermann[23], J. Ocariz[83], A. Ochi[70], I. Ochoa[38], J.P. Ochoa-Ricoux[34a], S. Oda[73], S. Odaka[69], H. Ogren[64], A. Oh[87], S.H. Oh[48], C.C. Ohm[16], H. Ohman[168], H. Oide[53a,53b], H. Okawa[164], Y. Okumura[157], T. Okuyama[69], A. Olariu[28b], L.F. Oleiro Seabra[128a], S.A. Olivares Pino[49], D. Oliveira Damazio[27], A. Olszewski[42], J. Olszowska[42], A. Onofre[128a,128e], K. Onogi[105], P.U.E. Onyisi[11,z], M.J. Oreglia[33], Y. Oren[155], D. Orestano[136a,136b], N. Orlando[62b], R.S. Orr[161], B. Osculati[53a,53b,*], R. Ospanov[87], G. Otero y Garzon[29], H. Otono[73], M. Ouchrif[137d], F. Ould-Saada[121], A. Ouraou[138], K.P. Oussoren[109], Q. Ouyang[35a], M. Owen[56], R.E. Owen[19], V.E. Ozcan[20a], N. Ozturk[8], K. Pachal[144], A. Pacheco Pages[13], L. Pacheco Rodriguez[138], C. Padilla Aranda[13], S. Pagan Griso[16], M. Paganini[179], F. Paige[27], P. Pais[89], G. Palacino[64], S. Palazzo[40a,40b], S. Palestini[32], M. Palka[41b], D. Pallin[37], E.St. Panagiotopoulou[10], I. Panagoulias[10], C.E. Pandini[83], J.G. Panduro Vazquez[80], P. Pani[32], S. Panitkin[27], D. Pantea[28b], L. Paolozzi[52], Th.D. Papadopoulou[10], K. Papageorgiou[9], A. Paramonov[6], D. Paredes Hernandez[179], A.J. Parker[75], M.A. Parker[30], K.A. Parker[45], F. Parodi[53a,53b], J.A. Parsons[38], U. Parzefall[51], V.R. Pascuzzi[161], J.M. Pasner[139], E. Pasqualucci[134a], S. Passaggio[53a], Fr. Pastore[80], S. Pataraia[178], J.R. Pater[87], T. Pauly[32], J. Pearce[172], B. Pearson[115], L.E. Pedersen[39], S. Pedraza Lopez[170], R. Pedro[128a,128b], S.V. Peleganchuk[111,c], O. Penc[129], C. Peng[35a], H. Peng[36a], J. Penwell[64], B.S. Peralva[26b], M.M. Perego[138], D.V. Perepelitsa[27], L. Perini[94a,94b], H. Pernegger[32], S. Perrella[106a,106b], R. Peschke[45], V.D. Peshekhonov[68], K. Peters[45], R.F.Y. Peters[87], B.A. Petersen[32], T.C. Petersen[39], E. Petit[58], A. Petridis[1], C. Petridou[156], P. Petroff[119], E. Petrolo[134a], M. Petrov[122], F. Petrucci[136a,136b], N.E. Pettersson[89], A. Peyaud[138], R. Pezoa[34b], P.W. Phillips[133], G. Piacquadio[150], E. Pianori[173], A. Picazio[89], E. Piccaro[79], M.A. Pickering[122], R. Piegaia[29], J.E. Pilcher[33], A.D. Pilkington[87], A.W.J. Pin[87], M. Pinamonti[167a,167c,al], J.L. Pinfold[3], H. Pirumov[45], M. Pitt[175], L. Plazak[146a], M.-A. Pleier[27], V. Pleskot[86], E. Plotnikova[68], D. Pluth[67], P. Podberezko[111], R. Poettgen[148a,148b], L. Poggioli[119], D. Pohl[23], G. Polesello[123a], A. Poley[45], A. Policicchio[40a,40b], R. Polifka[32], A. Polini[22a], C.S. Pollard[56], V. Polychronakos[27], K. Pommès[32], L. Pontecorvo[134a], B.G. Pope[93], G.A. Popeneciu[28d], A. Poppleton[32], S. Pospisil[130], K. Potamianos[16], I.N. Potrap[68], C.J. Potter[30], C.T. Potter[118], G. Poulard[32], J. Poveda[32], M.E. Pozo Astigarraga[32], P. Pralavorio[88], A. Pranko[16], S. Prell[67], D. Price[87], L.E. Price[6], M. Primavera[76a], S. Prince[90], K. Prokofiev[62c], F. Prokoshin[34b], S. Protopopescu[27], J. Proudfoot[6], M. Przybycien[41a], D. Puddu[136a,136b], A. Puri[169], P. Puzo[119], J. Qian[92], G. Qin[56], Y. Qin[87], A. Quadt[57], W.B. Quayle[167a,167b], M. Queitsch-Maitland[45], D. Quilty[56], S. Raddum[121], V. Radeka[27],

V. Radescu[122], S.K. Radhakrishnan[150], P. Radloff[118], P. Rados[91], F. Ragusa[94a,94b], G. Rahal[181], J.A. Raine[87], S. Rajagopalan[27], C. Rangel-Smith[168], M.G. Ratti[94a,94b], D.M. Rauch[45], F. Rauscher[102], S. Rave[86], T. Ravenscroft[56], I. Ravinovich[175], M. Raymond[32], A.L. Read[121], N.P. Readioff[77], M. Reale[76a,76b], D.M. Rebuzzi[123a,123b], A. Redelbach[177], G. Redlinger[27], R. Reece[139], R.G. Reed[147c], K. Reeves[44], L. Rehnisch[17], J. Reichert[124], A. Reiss[86], C. Rembser[32], H. Ren[35a], M. Rescigno[134a], S. Resconi[94a], E.D. Resseguie[124], S. Rettie[171], E. Reynolds[19], O.L. Rezanova[111,c], P. Reznicek[131], R. Rezvani[97], R. Richter[103], S. Richter[81], E. Richter-Was[41b], O. Ricken[23], M. Ridel[83], P. Rieck[103], C.J. Riegel[178], J. Rieger[57], O. Rifki[115], M. Rijssenbeek[150], A. Rimoldi[123a,123b], M. Rimoldi[18], L. Rinaldi[22a], B. Ristić[52], E. Ritsch[32], I. Riu[13], F. Rizatdinova[116], E. Rizvi[79], C. Rizzi[13], R.T. Roberts[87], S.H. Robertson[90,o], A. Robichaud-Veronneau[90], D. Robinson[30], J.E.M. Robinson[45], A. Robson[56], C. Roda[126a,126b], Y. Rodina[88,am], A. Rodriguez Perez[13], D. Rodriguez Rodriguez[170], S. Roe[32], C.S. Rogan[59], O. Røhne[121], J. Roloff[59], A. Romaniouk[100], M. Romano[22a,22b], S.M. Romano Saez[37], E. Romero Adam[170], N. Rompotis[77], M. Ronzani[51], L. Roos[83], S. Rosati[134a], K. Rosbach[51], P. Rose[139], N.-A. Rosien[57], V. Rossetti[148a,148b], E. Rossi[106a,106b], L.P. Rossi[53a], J.H.N. Rosten[30], R. Rosten[140], M. Rotaru[28b], I. Roth[175], J. Rothberg[140], D. Rousseau[119], A. Rozanov[88], Y. Rozen[154], X. Ruan[147c], F. Rubbo[145], F. Rühr[51], A. Ruiz-Martinez[31], Z. Rurikova[51], N.A. Rusakovich[68], A. Ruschke[102], H.L. Russell[140], J.P. Rutherfoord[7], N. Ruthmann[32], Y.F. Ryabov[125], M. Rybar[169], G. Rybkin[119], S. Ryu[6], A. Ryzhov[132], G.F. Rzehorz[57], A.F. Saavedra[152], G. Sabato[109], S. Sacerdoti[29], H.F-W. Sadrozinski[139], R. Sadykov[68], F. Safai Tehrani[134a], P. Saha[110], M. Sahinsoy[60a], M. Saimpert[45], T. Saito[157], H. Sakamoto[157], Y. Sakurai[174], G. Salamanna[136a,136b], J.E. Salazar Loyola[34b], D. Salek[109], P.H. Sales De Bruin[140], D. Salihagic[103], A. Salnikov[145], J. Salt[170], D. Salvatore[40a,40b], F. Salvatore[151], A. Salvucci[62a,62b,62c], A. Salzburger[32], D. Sammel[51], D. Sampsonidis[156], J. Sánchez[170], V. Sanchez Martinez[170], A. Sanchez Pineda[106a,106b], H. Sandaker[121], R.L. Sandbach[79], C.O. Sander[45], M. Sandhoff[178], C. Sandoval[21], D.P.C. Sankey[133], M. Sannino[53a,53b], A. Sansoni[50], C. Santoni[37], R. Santonico[135a,135b], H. Santos[128a], I. Santoyo Castillo[151], K. Sapp[127], A. Sapronov[68], J.G. Saraiva[128a,128d], B. Sarrazin[23], O. Sasaki[69], K. Sato[164], E. Sauvan[5], G. Savage[80], P. Savard[161,d], N. Savic[103], C. Sawyer[133], L. Sawyer[82,u], J. Saxon[33], C. Sbarra[22a], A. Sbrizzi[22a,22b], T. Scanlon[81], D.A. Scannicchio[166], M. Scarcella[152], V. Scarfone[40a,40b], J. Schaarschmidt[140], P. Schacht[103], B.M. Schachtner[102], D. Schaefer[32], L. Schaefer[124], R. Schaefer[45], J. Schaeffer[86], S. Schaepe[23], S. Schaetzel[60b], U. Schäfer[86], A.C. Schaffer[119], D. Schaile[102], R.D. Schamberger[150], V. Scharf[60a], V.A. Schegelsky[125], D. Scheirich[131], M. Schernau[166], C. Schiavi[53a,53b], S. Schier[139], C. Schillo[51], M. Schioppa[40a,40b], S. Schlenker[32], K.R. Schmidt-Sommerfeld[103], K. Schmieden[32], C. Schmitt[86], S. Schmitt[45], S. Schmitz[86], B. Schneider[163a], U. Schnoor[51], L. Schoeffel[138], A. Schoening[60b], B.D. Schoenrock[93], E. Schopf[23], M. Schott[86], J.F.P. Schouwenberg[108], J. Schovancova[8], S. Schramm[52], N. Schuh[86], A. Schulte[86], M.J. Schultens[23], H.-C. Schultz-Coulon[60a], H. Schulz[17], M. Schumacher[51], B.A. Schumm[139], Ph. Schune[138], A. Schwartzman[145], T.A. Schwarz[92], H. Schweiger[87], Ph. Schwemling[138], R. Schwienhorst[93], J. Schwindling[138], T. Schwindt[23], G. Sciolla[25], F. Scuri[126a,126b], F. Scutti[91], J. Searcy[92], P. Seema[23], S.C. Seidel[107], A. Seiden[139], J.M. Seixas[26a], G. Sekhniaidze[106a], K. Sekhon[92], S.J. Sekula[43], N. Semprini-Cesari[22a,22b], C. Serfon[121], L. Serin[119], L. Serkin[167a,167b], M. Sessa[136a,136b], R. Seuster[172], H. Severini[115], T. Sfiligoj[78], F. Sforza[32], A. Sfyrla[52], E. Shabalina[57], N.W. Shaikh[148a,148b], L.Y. Shan[35a], R. Shang[169], J.T. Shank[24], M. Shapiro[16], P.B. Shatalov[99], K. Shaw[167a,167b], S.M. Shaw[87], A. Shcherbakova[148a,148b], C.Y. Shehu[151], Y. Shen[115], P. Sherwood[81], L. Shi[153,an], S. Shimizu[70], C.O. Shimmin[179], M. Shimojima[104], S. Shirabe[73], M. Shiyakova[68,ao], J. Shlomi[175], A. Shmeleva[98], D. Shoaleh Saadi[97], M.J. Shochet[33], S. Shojaii[94a], D.R. Shope[115], S. Shrestha[113], E. Shulga[100], M.A. Shupe[7], P. Sicho[129], A.M. Sickles[169], P.E. Sidebo[149], E. Sideras Haddad[147c], O. Sidiropoulou[177], D. Sidorov[116], A. Sidoti[22a,22b], F. Siegert[47], Dj. Sijacki[14], J. Silva[128a,128d], S.B. Silverstein[148a], V. Simak[130], Lj. Simic[14], S. Simion[119], E. Simioni[86],

B. Simmons[81], M. Simon[86], P. Sinervo[161], N.B. Sinev[118], M. Sioli[22a,22b], G. Siragusa[177], I. Siral[92], S.Yu. Sivoklokov[101], J. Sjölin[148a,148b], M.B. Skinner[75], P. Skubic[115], M. Slater[19], T. Slavicek[130], M. Slawinska[109], K. Sliwa[165], R. Slovak[131], V. Smakhtin[175], B.H. Smart[5], L. Smestad[15], J. Smiesko[146a], S.Yu. Smirnov[100], Y. Smirnov[100], L.N. Smirnova[101,*ap*], O. Smirnova[84], J.W. Smith[57], M.N.K. Smith[38], R.W. Smith[38], M. Smizanska[75], K. Smolek[130], A.A. Snesarev[98], I.M. Snyder[118], S. Snyder[27], R. Sobie[172,*o*], F. Socher[47], A. Soffer[155], D.A. Soh[153], G. Sokhrannyi[78], C.A. Solans Sanchez[32], M. Solar[130], E.Yu. Soldatov[100], U. Soldevila[170], A.A. Solodkov[132], A. Soloshenko[68], O.V. Solovyanov[132], V. Solovyev[125], P. Sommer[51], H. Son[165], H.Y. Song[36a,*aq*], A. Sopczak[130], V. Sorin[13], D. Sosa[60b], C.L. Sotiropoulou[126a,126b], R. Soualah[167a,167c], A.M. Soukharev[111,*c*], D. South[45], B.C. Sowden[80], S. Spagnolo[76a,76b], M. Spalla[126a,126b], M. Spangenberg[173], F. Spanò[80], D. Sperlich[17], F. Spettel[103], T.M. Spieker[60a], R. Spighi[22a], G. Spigo[32], L.A. Spiller[91], M. Spousta[131], R.D. St. Denis[56,*], A. Stabile[94a], R. Stamen[60a], S. Stamm[17], E. Stanecka[42], R.W. Stanek[6], C. Stanescu[136a], M.M. Stanitzki[45], S. Stapnes[121], E.A. Starchenko[132], G.H. Stark[33], J. Stark[58], S.H Stark[39], P. Staroba[129], P. Starovoitov[60a], S. Stärz[32], R. Staszewski[42], P. Steinberg[27], B. Stelzer[144], H.J. Stelzer[32], O. Stelzer-Chilton[163a], H. Stenzel[55], G.A. Stewart[56], J.A. Stillings[23], M.C. Stockton[90], M. Stoebe[90], G. Stoicea[28b], P. Stolte[57], S. Stonjek[103], A.R. Stradling[8], A. Straessner[47], M.E. Stramaglia[18], J. Strandberg[149], S. Strandberg[148a,148b], A. Strandlie[121], M. Strauss[115], P. Strizenec[146b], R. Ströhmer[177], D.M. Strom[118], R. Stroynowski[43], A. Strubig[108], S.A. Stucci[27], B. Stugu[15], N.A. Styles[45], D. Su[145], J. Su[127], S. Suchek[60a], Y. Sugaya[120], M. Suk[130], V.V. Sulin[98], S. Sultansoy[4c], T. Sumida[71], S. Sun[59], X. Sun[3], K. Suruliz[151], C.J.E. Suster[152], M.R. Sutton[151], S. Suzuki[69], M. Svatos[129], M. Swiatlowski[33], S.P. Swift[2], I. Sykora[146a], T. Sykora[131], D. Ta[51], K. Tackmann[45], J. Taenzer[155], A. Taffard[166], R. Tafirout[163a], N. Taiblum[155], H. Takai[27], R. Takashima[72], T. Takeshita[142], Y. Takubo[69], M. Talby[88], A.A. Talyshev[111,*c*], J. Tanaka[157], M. Tanaka[159], R. Tanaka[119], S. Tanaka[69], R. Tanioka[70], B.B. Tannenwald[113], S. Tapia Araya[34b], S. Tapprogge[86], S. Tarem[154], G.F. Tartarelli[94a], P. Tas[131], M. Tasevsky[129], T. Tashiro[71], E. Tassi[40a,40b], A. Tavares Delgado[128a,128b], Y. Tayalati[137e], A.C. Taylor[107], G.N. Taylor[91], P.T.E. Taylor[91], W. Taylor[163b], P. Teixeira-Dias[80], D. Temple[144], H. Ten Kate[32], P.K. Teng[153], J.J. Teoh[120], F. Tepel[178], S. Terada[69], K. Terashi[157], J. Terron[85], S. Terzo[13], M. Testa[50], R.J. Teuscher[161,*o*], T. Theveneaux-Pelzer[88], J.P. Thomas[19], J. Thomas-Wilsker[80], P.D. Thompson[19], A.S. Thompson[56], L.A. Thomsen[179], E. Thomson[124], M.J. Tibbetts[16], R.E. Ticse Torres[88], V.O. Tikhomirov[98,*ar*], Yu.A. Tikhonov[111,*c*], S. Timoshenko[100], P. Tipton[179], S. Tisserant[88], K. Todome[159], S. Todorova-Nova[5], J. Tojo[73], S. Tokár[146a], K. Tokushuku[69], E. Tolley[59], L. Tomlinson[87], M. Tomoto[105], L. Tompkins[145,*as*], K. Toms[107], B. Tong[59], P. Tornambe[51], E. Torrence[118], H. Torres[144], E. Torró Pastor[140], J. Toth[88,*at*], F. Touchard[88], D.R. Tovey[141], C.J. Treado[112], T. Trefzger[177], A. Tricoli[27], I.M. Trigger[163a], S. Trincaz-Duvoid[83], M.F. Tripiana[13], W. Trischuk[161], B. Trocmé[58], A. Trofymov[45], C. Troncon[94a], M. Trottier-McDonald[16], M. Trovatelli[172], L. Truong[167a,167c], M. Trzebinski[42], A. Trzupek[42], K.W. Tsang[62a], J.C-L. Tseng[122], P.V. Tsiareshka[95], G. Tsipolitis[10], N. Tsirintanis[9], S. Tsiskaridze[13], V. Tsiskaridze[51], E.G. Tskhadadze[54a], K.M. Tsui[62a], I.I. Tsukerman[99], V. Tsulaia[16], S. Tsuno[69], D. Tsybychev[150], Y. Tu[62b], A. Tudorache[28b], V. Tudorache[28b], T.T. Tulbure[28a], A.N. Tuna[59], S.A. Tupputi[22a,22b], S. Turchikhin[68], D. Turgeman[175], I. Turk Cakir[4b,*au*], R. Turra[94a,94b], P.M. Tuts[38], G. Ucchielli[22a,22b], I. Ueda[69], M. Ughetto[148a,148b], F. Ukegawa[164], G. Unal[32], A. Undrus[27], G. Unel[166], F.C. Ungaro[91], Y. Unno[69], C. Unverdorben[102], J. Urban[146b], P. Urquijo[91], P. Urrejola[86], G. Usai[8], J. Usui[69], L. Vacavant[88], V. Vacek[130], B. Vachon[90], C. Valderanis[102], E. Valdes Santurio[148a,148b], N. Valencic[109], S. Valentinetti[22a,22b], A. Valero[170], L. Valéry[13], S. Valkar[131], A. Vallier[5], J.A. Valls Ferrer[170], W. Van Den Wollenberg[109], H. van der Graaf[109], N. van Eldik[154], P. van Gemmeren[6], J. Van Nieuwkoop[144], I. van Vulpen[109], M.C. van Woerden[109], M. Vanadia[134a,134b], W. Vandelli[32], R. Vanguri[124], A. Vaniachine[160], P. Vankov[109], G. Vardanyan[180], R. Vari[134a], E.W. Varnes[7], C. Varni[53a,53b], T. Varol[43], D. Varouchas[83], A. Vartapetian[8], K.E. Varvell[152],

J.G. Vasquez[179], G.A. Vasquez[34b], F. Vazeille[37], T. Vazquez Schroeder[90], J. Veatch[57], V. Veeraraghavan[7], L.M. Veloce[161], F. Veloso[128a,128c], S. Veneziano[134a], A. Ventura[76a,76b], M. Venturi[172], N. Venturi[161], A. Venturini[25], V. Vercesi[123a], M. Verducci[136a,136b], W. Verkerke[109], J.C. Vermeulen[109], M.C. Vetterli[144,d], N. Viaux Maira[34a], O. Viazlo[84], I. Vichou[169,*], T. Vickey[141], O.E. Vickey Boeriu[141], G.H.A. Viehhauser[122], S. Viel[16], L. Vigani[122], M. Villa[22a,22b], M. Villaplana Perez[94a,94b], E. Vilucchi[50], M.G. Vincter[31], V.B. Vinogradov[68], A. Vishwakarma[45], C. Vittori[22a,22b], I. Vivarelli[151], S. Vlachos[10], M. Vlasak[130], M. Vogel[178], P. Vokac[130], G. Volpi[126a,126b], M. Volpi[91], H. von der Schmitt[103], E. von Toerne[23], V. Vorobel[131], K. Vorobev[100], M. Vos[170], R. Voss[32], J.H. Vossebeld[77], N. Vranjes[14], M. Vranjes Milosavljevic[14], V. Vrba[130], M. Vreeswijk[109], R. Vuillermet[32], I. Vukotic[33], P. Wagner[23], W. Wagner[178], H. Wahlberg[74], S. Wahrmund[47], J. Wakabayashi[105], J. Walder[75], R. Walker[102], W. Walkowiak[143], V. Wallangen[148a,148b], C. Wang[35b], C. Wang[36b,av], F. Wang[176], H. Wang[16], H. Wang[3], J. Wang[45], J. Wang[152], Q. Wang[115], R. Wang[6], S.M. Wang[153], T. Wang[38], W. Wang[153,aw], W. Wang[36a], C. Wanotayaroj[118], A. Warburton[90], C.P. Ward[30], D.R. Wardrope[81], A. Washbrook[49], P.M. Watkins[19], A.T. Watson[19], M.F. Watson[19], G. Watts[140], S. Watts[87], B.M. Waugh[81], A.F. Webb[11], S. Webb[86], M.S. Weber[18], S.W. Weber[177], S.A. Weber[31], J.S. Webster[6], A.R. Weidberg[122], B. Weinert[64], J. Weingarten[57], C. Weiser[51], H. Weits[109], P.S. Wells[32], T. Wenaus[27], T. Wengler[32], S. Wenig[32], N. Wermes[23], M.D. Werner[67], P. Werner[32], M. Wessels[60a], K. Whalen[118], N.L. Whallon[140], A.M. Wharton[75], A. White[8], M.J. White[1], R. White[34b], D. Whiteson[166], F.J. Wickens[133], W. Wiedenmann[176], M. Wielers[133], C. Wiglesworth[39], L.A.M. Wiik-Fuchs[23], A. Wildauer[103], F. Wilk[87], H.G. Wilkens[32], H.H. Williams[124], S. Williams[109], C. Willis[93], S. Willocq[89], J.A. Wilson[19], I. Wingerter-Seez[5], F. Winklmeier[118], O.J. Winston[151], B.T. Winter[23], M. Wittgen[145], M. Wobisch[82,u], T.M.H. Wolf[109], R. Wolff[88], M.W. Wolter[42], H. Wolters[128a,128c], S.D. Worm[19], B.K. Wosiek[42], J. Wotschack[32], M.J. Woudstra[87], K.W. Wozniak[42], M. Wu[33], S.L. Wu[176], X. Wu[52], Y. Wu[92], T.R. Wyatt[87], B.M. Wynne[49], S. Xella[39], Z. Xi[92], L. Xia[35c], D. Xu[35a], L. Xu[27], B. Yabsley[152], S. Yacoob[147a], D. Yamaguchi[159], Y. Yamaguchi[120], A. Yamamoto[69], S. Yamamoto[157], T. Yamanaka[157], K. Yamauchi[105], Y. Yamazaki[70], Z. Yan[24], H. Yang[36c], H. Yang[16], Y. Yang[153], Z. Yang[15], W-M. Yao[16], Y.C. Yap[83], Y. Yasu[69], E. Yatsenko[5], K.H. Yau Wong[23], J. Ye[43], S. Ye[27], I. Yeletskikh[68], E. Yildirim[86], K. Yorita[174], K. Yoshihara[124], C. Young[145], C.J.S. Young[32], S. Youssef[24], D.R. Yu[16], J. Yu[8], J. Yu[67], L. Yuan[70], S.P.Y. Yuen[23], I. Yusuff[30,ax], B. Zabinski[42], G. Zacharis[10], R. Zaidan[13], A.M. Zaitsev[132,aj], N. Zakharchuk[45], J. Zalieckas[15], A. Zaman[150], S. Zambito[59], D. Zanzi[91], C. Zeitnitz[178], M. Zeman[130], A. Zemla[41a], J.C. Zeng[169], Q. Zeng[145], O. Zenin[132], T. Ženiš[146a], D. Zerwas[119], D. Zhang[92], F. Zhang[176], G. Zhang[36a,aq], H. Zhang[35b], J. Zhang[6], L. Zhang[51], L. Zhang[36a], M. Zhang[169], R. Zhang[23], R. Zhang[36a,av], X. Zhang[36b], Y. Zhang[35a], Z. Zhang[119], X. Zhao[43], Y. Zhao[36b,ay], Z. Zhao[36a], A. Zhemchugov[68], J. Zhong[122], B. Zhou[92], C. Zhou[176], L. Zhou[43], M. Zhou[35a], M. Zhou[150], N. Zhou[35c], C.G. Zhu[36b], H. Zhu[35a], J. Zhu[92], Y. Zhu[36a], X. Zhuang[35a], K. Zhukov[98], A. Zibell[177], D. Zieminska[64], N.I. Zimine[68], C. Zimmermann[86], S. Zimmermann[51], Z. Zinonos[103], M. Zinser[86], M. Ziolkowski[143], L. Živković[14], G. Zobernig[176], A. Zoccoli[22a,22b], R. Zou[33], M. zur Nedden[17], L. Zwalinski[32].

[1] Department of Physics, University of Adelaide, Adelaide, Australia
[2] Physics Department, SUNY Albany, Albany NY, United States of America
[3] Department of Physics, University of Alberta, Edmonton AB, Canada
[4] (a) Department of Physics, Ankara University, Ankara; (b) Istanbul Aydin University, Istanbul; (c) Division of Physics, TOBB University of Economics and Technology, Ankara, Turkey
[5] LAPP, CNRS/IN2P3 and Université Savoie Mont Blanc, Annecy-le-Vieux, France
[6] High Energy Physics Division, Argonne National Laboratory, Argonne IL, United States of America
[7] Department of Physics, University of Arizona, Tucson AZ, United States of America
[8] Department of Physics, The University of Texas at Arlington, Arlington TX, United States of America

[9] Physics Department, National and Kapodistrian University of Athens, Athens, Greece
[10] Physics Department, National Technical University of Athens, Zografou, Greece
[11] Department of Physics, The University of Texas at Austin, Austin TX, United States of America
[12] Institute of Physics, Azerbaijan Academy of Sciences, Baku, Azerbaijan
[13] Institut de Física d'Altes Energies (IFAE), The Barcelona Institute of Science and Technology, Barcelona, Spain
[14] Institute of Physics, University of Belgrade, Belgrade, Serbia
[15] Department for Physics and Technology, University of Bergen, Bergen, Norway
[16] Physics Division, Lawrence Berkeley National Laboratory and University of California, Berkeley CA, United States of America
[17] Department of Physics, Humboldt University, Berlin, Germany
[18] Albert Einstein Center for Fundamental Physics and Laboratory for High Energy Physics, University of Bern, Bern, Switzerland
[19] School of Physics and Astronomy, University of Birmingham, Birmingham, United Kingdom
[20] [(a)] Department of Physics, Bogazici University, Istanbul; [(b)] Department of Physics Engineering, Gaziantep University, Gaziantep; [(d)] Istanbul Bilgi University, Faculty of Engineering and Natural Sciences, Istanbul,Turkey; [(e)] Bahcesehir University, Faculty of Engineering and Natural Sciences, Istanbul, Turkey, Turkey
[21] Centro de Investigaciones, Universidad Antonio Narino, Bogota, Colombia
[22] [(a)] INFN Sezione di Bologna; [(b)] Dipartimento di Fisica e Astronomia, Università di Bologna, Bologna, Italy
[23] Physikalisches Institut, University of Bonn, Bonn, Germany
[24] Department of Physics, Boston University, Boston MA, United States of America
[25] Department of Physics, Brandeis University, Waltham MA, United States of America
[26] [(a)] Universidade Federal do Rio De Janeiro COPPE/EE/IF, Rio de Janeiro; [(b)] Electrical Circuits Department, Federal University of Juiz de Fora (UFJF), Juiz de Fora; [(c)] Federal University of Sao Joao del Rei (UFSJ), Sao Joao del Rei; [(d)] Instituto de Fisica, Universidade de Sao Paulo, Sao Paulo, Brazil
[27] Physics Department, Brookhaven National Laboratory, Upton NY, United States of America
[28] [(a)] Transilvania University of Brasov, Brasov, Romania; [(b)] Horia Hulubei National Institute of Physics and Nuclear Engineering, Bucharest; [(c)] Department of Physics, Alexandru Ioan Cuza University of Iasi, Iasi, Romania; [(d)] National Institute for Research and Development of Isotopic and Molecular Technologies, Physics Department, Cluj Napoca; [(e)] University Politehnica Bucharest, Bucharest; [(f)] West University in Timisoara, Timisoara, Romania
[29] Departamento de Física, Universidad de Buenos Aires, Buenos Aires, Argentina
[30] Cavendish Laboratory, University of Cambridge, Cambridge, United Kingdom
[31] Department of Physics, Carleton University, Ottawa ON, Canada
[32] CERN, Geneva, Switzerland
[33] Enrico Fermi Institute, University of Chicago, Chicago IL, United States of America
[34] [(a)] Departamento de Física, Pontificia Universidad Católica de Chile, Santiago; [(b)] Departamento de Física, Universidad Técnica Federico Santa María, Valparaíso, Chile
[35] [(a)] Institute of High Energy Physics, Chinese Academy of Sciences, Beijing; [(b)] Department of Physics, Nanjing University, Jiangsu; [(c)] Physics Department, Tsinghua University, Beijing 100084, China
[36] [(a)] Department of Modern Physics, University of Science and Technology of China, Anhui; [(b)] School of Physics, Shandong University, Shandong; [(c)] Department of Physics and Astronomy, Key Laboratory for Particle Physics, Astrophysics and Cosmology, Ministry of Education; Shanghai Key Laboratory for Particle Physics and Cosmology, Shanghai Jiao Tong University, Shanghai(also at PKU-CHEP);, China

[37] Université Clermont Auvergne, CNRS/IN2P3, LPC, Clermont-Ferrand, France
[38] Nevis Laboratory, Columbia University, Irvington NY, United States of America
[39] Niels Bohr Institute, University of Copenhagen, Kobenhavn, Denmark
[40] [(a)] INFN Gruppo Collegato di Cosenza, Laboratori Nazionali di Frascati; [(b)] Dipartimento di Fisica, Università della Calabria, Rende, Italy
[41] [(a)] AGH University of Science and Technology, Faculty of Physics and Applied Computer Science, Krakow; [(b)] Marian Smoluchowski Institute of Physics, Jagiellonian University, Krakow, Poland
[42] Institute of Nuclear Physics Polish Academy of Sciences, Krakow, Poland
[43] Physics Department, Southern Methodist University, Dallas TX, United States of America
[44] Physics Department, University of Texas at Dallas, Richardson TX, United States of America
[45] DESY, Hamburg and Zeuthen, Germany
[46] Lehrstuhl für Experimentelle Physik IV, Technische Universität Dortmund, Dortmund, Germany
[47] Institut für Kern- und Teilchenphysik, Technische Universität Dresden, Dresden, Germany
[48] Department of Physics, Duke University, Durham NC, United States of America
[49] SUPA - School of Physics and Astronomy, University of Edinburgh, Edinburgh, United Kingdom
[50] INFN Laboratori Nazionali di Frascati, Frascati, Italy
[51] Fakultät für Mathematik und Physik, Albert-Ludwigs-Universität, Freiburg, Germany
[52] Departement de Physique Nucleaire et Corpusculaire, Université de Genève, Geneva, Switzerland
[53] [(a)] INFN Sezione di Genova; [(b)] Dipartimento di Fisica, Università di Genova, Genova, Italy
[54] [(a)] E. Andronikashvili Institute of Physics, Iv. Javakhishvili Tbilisi State University, Tbilisi; [(b)] High Energy Physics Institute, Tbilisi State University, Tbilisi, Georgia
[55] II Physikalisches Institut, Justus-Liebig-Universität Giessen, Giessen, Germany
[56] SUPA - School of Physics and Astronomy, University of Glasgow, Glasgow, United Kingdom
[57] II Physikalisches Institut, Georg-August-Universität, Göttingen, Germany
[58] Laboratoire de Physique Subatomique et de Cosmologie, Université Grenoble-Alpes, CNRS/IN2P3, Grenoble, France
[59] Laboratory for Particle Physics and Cosmology, Harvard University, Cambridge MA, United States of America
[60] [(a)] Kirchhoff-Institut für Physik, Ruprecht-Karls-Universität Heidelberg, Heidelberg; [(b)] Physikalisches Institut, Ruprecht-Karls-Universität Heidelberg, Heidelberg; [(c)] ZITI Institut für technische Informatik, Ruprecht-Karls-Universität Heidelberg, Mannheim, Germany
[61] Faculty of Applied Information Science, Hiroshima Institute of Technology, Hiroshima, Japan
[62] [(a)] Department of Physics, The Chinese University of Hong Kong, Shatin, N.T., Hong Kong; [(b)] Department of Physics, The University of Hong Kong, Hong Kong; [(c)] Department of Physics and Institute for Advanced Study, The Hong Kong University of Science and Technology, Clear Water Bay, Kowloon, Hong Kong, China
[63] Department of Physics, National Tsing Hua University, Taiwan, Taiwan
[64] Department of Physics, Indiana University, Bloomington IN, United States of America
[65] Institut für Astro- und Teilchenphysik, Leopold-Franzens-Universität, Innsbruck, Austria
[66] University of Iowa, Iowa City IA, United States of America
[67] Department of Physics and Astronomy, Iowa State University, Ames IA, United States of America
[68] Joint Institute for Nuclear Research, JINR Dubna, Dubna, Russia
[69] KEK, High Energy Accelerator Research Organization, Tsukuba, Japan
[70] Graduate School of Science, Kobe University, Kobe, Japan
[71] Faculty of Science, Kyoto University, Kyoto, Japan
[72] Kyoto University of Education, Kyoto, Japan
[73] Department of Physics, Kyushu University, Fukuoka, Japan

[74] Instituto de Física La Plata, Universidad Nacional de La Plata and CONICET, La Plata, Argentina
[75] Physics Department, Lancaster University, Lancaster, United Kingdom
[76] [(a)] INFN Sezione di Lecce; [(b)] Dipartimento di Matematica e Fisica, Università del Salento, Lecce, Italy
[77] Oliver Lodge Laboratory, University of Liverpool, Liverpool, United Kingdom
[78] Department of Experimental Particle Physics, Jožef Stefan Institute and Department of Physics, University of Ljubljana, Ljubljana, Slovenia
[79] School of Physics and Astronomy, Queen Mary University of London, London, United Kingdom
[80] Department of Physics, Royal Holloway University of London, Surrey, United Kingdom
[81] Department of Physics and Astronomy, University College London, London, United Kingdom
[82] Louisiana Tech University, Ruston LA, United States of America
[83] Laboratoire de Physique Nucléaire et de Hautes Energies, UPMC and Université Paris-Diderot and CNRS/IN2P3, Paris, France
[84] Fysiska institutionen, Lunds universitet, Lund, Sweden
[85] Departamento de Fisica Teorica C-15, Universidad Autonoma de Madrid, Madrid, Spain
[86] Institut für Physik, Universität Mainz, Mainz, Germany
[87] School of Physics and Astronomy, University of Manchester, Manchester, United Kingdom
[88] CPPM, Aix-Marseille Université and CNRS/IN2P3, Marseille, France
[89] Department of Physics, University of Massachusetts, Amherst MA, United States of America
[90] Department of Physics, McGill University, Montreal QC, Canada
[91] School of Physics, University of Melbourne, Victoria, Australia
[92] Department of Physics, The University of Michigan, Ann Arbor MI, United States of America
[93] Department of Physics and Astronomy, Michigan State University, East Lansing MI, United States of America
[94] [(a)] INFN Sezione di Milano; [(b)] Dipartimento di Fisica, Università di Milano, Milano, Italy
[95] B.I. Stepanov Institute of Physics, National Academy of Sciences of Belarus, Minsk, Republic of Belarus
[96] Research Institute for Nuclear Problems of Byelorussian State University, Minsk, Republic of Belarus
[97] Group of Particle Physics, University of Montreal, Montreal QC, Canada
[98] P.N. Lebedev Physical Institute of the Russian Academy of Sciences, Moscow, Russia
[99] Institute for Theoretical and Experimental Physics (ITEP), Moscow, Russia
[100] National Research Nuclear University MEPhI, Moscow, Russia
[101] D.V. Skobeltsyn Institute of Nuclear Physics, M.V. Lomonosov Moscow State University, Moscow, Russia
[102] Fakultät für Physik, Ludwig-Maximilians-Universität München, München, Germany
[103] Max-Planck-Institut für Physik (Werner-Heisenberg-Institut), München, Germany
[104] Nagasaki Institute of Applied Science, Nagasaki, Japan
[105] Graduate School of Science and Kobayashi-Maskawa Institute, Nagoya University, Nagoya, Japan
[106] [(a)] INFN Sezione di Napoli; [(b)] Dipartimento di Fisica, Università di Napoli, Napoli, Italy
[107] Department of Physics and Astronomy, University of New Mexico, Albuquerque NM, United States of America
[108] Institute for Mathematics, Astrophysics and Particle Physics, Radboud University Nijmegen/Nikhef, Nijmegen, Netherlands
[109] Nikhef National Institute for Subatomic Physics and University of Amsterdam, Amsterdam, Netherlands
[110] Department of Physics, Northern Illinois University, DeKalb IL, United States of America
[111] Budker Institute of Nuclear Physics, SB RAS, Novosibirsk, Russia

[112] Department of Physics, New York University, New York NY, United States of America
[113] Ohio State University, Columbus OH, United States of America
[114] Faculty of Science, Okayama University, Okayama, Japan
[115] Homer L. Dodge Department of Physics and Astronomy, University of Oklahoma, Norman OK, United States of America
[116] Department of Physics, Oklahoma State University, Stillwater OK, United States of America
[117] Palacký University, RCPTM, Olomouc, Czech Republic
[118] Center for High Energy Physics, University of Oregon, Eugene OR, United States of America
[119] LAL, Univ. Paris-Sud, CNRS/IN2P3, Université Paris-Saclay, Orsay, France
[120] Graduate School of Science, Osaka University, Osaka, Japan
[121] Department of Physics, University of Oslo, Oslo, Norway
[122] Department of Physics, Oxford University, Oxford, United Kingdom
[123] [(a)] INFN Sezione di Pavia; [(b)] Dipartimento di Fisica, Università di Pavia, Pavia, Italy
[124] Department of Physics, University of Pennsylvania, Philadelphia PA, United States of America
[125] National Research Centre "Kurchatov Institute" B.P.Konstantinov Petersburg Nuclear Physics Institute, St. Petersburg, Russia
[126] [(a)] INFN Sezione di Pisa; [(b)] Dipartimento di Fisica E. Fermi, Università di Pisa, Pisa, Italy
[127] Department of Physics and Astronomy, University of Pittsburgh, Pittsburgh PA, United States of America
[128] [(a)] Laboratório de Instrumentação e Física Experimental de Partículas - LIP, Lisboa; [(b)] Faculdade de Ciências, Universidade de Lisboa, Lisboa; [(c)] Department of Physics, University of Coimbra, Coimbra; [(d)] Centro de Física Nuclear da Universidade de Lisboa, Lisboa; [(e)] Departamento de Fisica, Universidade do Minho, Braga; [(f)] Departamento de Fisica Teorica y del Cosmos and CAFPE, Universidad de Granada, Granada (Spain); [(g)] Dep Fisica and CEFITEC of Faculdade de Ciencias e Tecnologia, Universidade Nova de Lisboa, Caparica, Portugal
[129] Institute of Physics, Academy of Sciences of the Czech Republic, Praha, Czech Republic
[130] Czech Technical University in Prague, Praha, Czech Republic
[131] Charles University, Faculty of Mathematics and Physics, Prague, Czech Republic
[132] State Research Center Institute for High Energy Physics (Protvino), NRC KI, Russia
[133] Particle Physics Department, Rutherford Appleton Laboratory, Didcot, United Kingdom
[134] [(a)] INFN Sezione di Roma; [(b)] Dipartimento di Fisica, Sapienza Università di Roma, Roma, Italy
[135] [(a)] INFN Sezione di Roma Tor Vergata; [(b)] Dipartimento di Fisica, Università di Roma Tor Vergata, Roma, Italy
[136] [(a)] INFN Sezione di Roma Tre; [(b)] Dipartimento di Matematica e Fisica, Università Roma Tre, Roma, Italy
[137] [(a)] Faculté des Sciences Ain Chock, Réseau Universitaire de Physique des Hautes Energies - Université Hassan II, Casablanca; [(b)] Centre National de l'Energie des Sciences Techniques Nucleaires, Rabat; [(c)] Faculté des Sciences Semlalia, Université Cadi Ayyad, LPHEA-Marrakech; [(d)] Faculté des Sciences, Université Mohamed Premier and LPTPM, Oujda; [(e)] Faculté des sciences, Université Mohammed V, Rabat, Morocco
[138] DSM/IRFU (Institut de Recherches sur les Lois Fondamentales de l'Univers), CEA Saclay (Commissariat à l'Energie Atomique et aux Energies Alternatives), Gif-sur-Yvette, France
[139] Santa Cruz Institute for Particle Physics, University of California Santa Cruz, Santa Cruz CA, United States of America
[140] Department of Physics, University of Washington, Seattle WA, United States of America
[141] Department of Physics and Astronomy, University of Sheffield, Sheffield, United Kingdom
[142] Department of Physics, Shinshu University, Nagano, Japan

[143] Department Physik, Universität Siegen, Siegen, Germany
[144] Department of Physics, Simon Fraser University, Burnaby BC, Canada
[145] SLAC National Accelerator Laboratory, Stanford CA, United States of America
[146] [(a)] Faculty of Mathematics, Physics & Informatics, Comenius University, Bratislava; [(b)] Department of Subnuclear Physics, Institute of Experimental Physics of the Slovak Academy of Sciences, Kosice, Slovak Republic
[147] [(a)] Department of Physics, University of Cape Town, Cape Town; [(b)] Department of Physics, University of Johannesburg, Johannesburg; [(c)] School of Physics, University of the Witwatersrand, Johannesburg, South Africa
[148] [(a)] Department of Physics, Stockholm University; [(b)] The Oskar Klein Centre, Stockholm, Sweden
[149] Physics Department, Royal Institute of Technology, Stockholm, Sweden
[150] Departments of Physics & Astronomy and Chemistry, Stony Brook University, Stony Brook NY, United States of America
[151] Department of Physics and Astronomy, University of Sussex, Brighton, United Kingdom
[152] School of Physics, University of Sydney, Sydney, Australia
[153] Institute of Physics, Academia Sinica, Taipei, Taiwan
[154] Department of Physics, Technion: Israel Institute of Technology, Haifa, Israel
[155] Raymond and Beverly Sackler School of Physics and Astronomy, Tel Aviv University, Tel Aviv, Israel
[156] Department of Physics, Aristotle University of Thessaloniki, Thessaloniki, Greece
[157] International Center for Elementary Particle Physics and Department of Physics, The University of Tokyo, Tokyo, Japan
[158] Graduate School of Science and Technology, Tokyo Metropolitan University, Tokyo, Japan
[159] Department of Physics, Tokyo Institute of Technology, Tokyo, Japan
[160] Tomsk State University, Tomsk, Russia, Russia
[161] Department of Physics, University of Toronto, Toronto ON, Canada
[162] [(a)] INFN-TIFPA; [(b)] University of Trento, Trento, Italy, Italy
[163] [(a)] TRIUMF, Vancouver BC; [(b)] Department of Physics and Astronomy, York University, Toronto ON, Canada
[164] Faculty of Pure and Applied Sciences, and Center for Integrated Research in Fundamental Science and Engineering, University of Tsukuba, Tsukuba, Japan
[165] Department of Physics and Astronomy, Tufts University, Medford MA, United States of America
[166] Department of Physics and Astronomy, University of California Irvine, Irvine CA, United States of America
[167] [(a)] INFN Gruppo Collegato di Udine, Sezione di Trieste, Udine; [(b)] ICTP, Trieste; [(c)] Dipartimento di Chimica, Fisica e Ambiente, Università di Udine, Udine, Italy
[168] Department of Physics and Astronomy, University of Uppsala, Uppsala, Sweden
[169] Department of Physics, University of Illinois, Urbana IL, United States of America
[170] Instituto de Fisica Corpuscular (IFIC) and Departamento de Fisica Atomica, Molecular y Nuclear and Departamento de Ingeniería Electrónica and Instituto de Microelectrónica de Barcelona (IMB-CNM), University of Valencia and CSIC, Valencia, Spain
[171] Department of Physics, University of British Columbia, Vancouver BC, Canada
[172] Department of Physics and Astronomy, University of Victoria, Victoria BC, Canada
[173] Department of Physics, University of Warwick, Coventry, United Kingdom
[174] Waseda University, Tokyo, Japan
[175] Department of Particle Physics, The Weizmann Institute of Science, Rehovot, Israel
[176] Department of Physics, University of Wisconsin, Madison WI, United States of America

[177] Fakultät für Physik und Astronomie, Julius-Maximilians-Universität, Würzburg, Germany
[178] Fakultät für Mathematik und Naturwissenschaften, Fachgruppe Physik, Bergische Universität Wuppertal, Wuppertal, Germany
[179] Department of Physics, Yale University, New Haven CT, United States of America
[180] Yerevan Physics Institute, Yerevan, Armenia
[181] Centre de Calcul de l'Institut National de Physique Nucléaire et de Physique des Particules (IN2P3), Villeurbanne, France
[a] Also at Department of Physics, King's College London, London, United Kingdom
[b] Also at Institute of Physics, Azerbaijan Academy of Sciences, Baku, Azerbaijan
[c] Also at Novosibirsk State University, Novosibirsk, Russia
[d] Also at TRIUMF, Vancouver BC, Canada
[e] Also at Department of Physics & Astronomy, University of Louisville, Louisville, KY, United States of America
[f] Also at Physics Department, An-Najah National University, Nablus, Palestine
[g] Also at Department of Physics, California State University, Fresno CA, United States of America
[h] Also at Department of Physics, University of Fribourg, Fribourg, Switzerland
[i] Also at II Physikalisches Institut, Georg-August-Universität, Göttingen, Germany
[j] Also at Departament de Fisica de la Universitat Autonoma de Barcelona, Barcelona, Spain
[k] Also at Departamento de Fisica e Astronomia, Faculdade de Ciencias, Universidade do Porto, Portugal
[l] Also at Tomsk State University, Tomsk, Russia, Russia
[m] Also at The Collaborative Innovation Center of Quantum Matter (CICQM), Beijing, China
[n] Also at Universita di Napoli Parthenope, Napoli, Italy
[o] Also at Institute of Particle Physics (IPP), Canada
[p] Also at Horia Hulubei National Institute of Physics and Nuclear Engineering, Bucharest, Romania
[q] Also at Department of Physics, St. Petersburg State Polytechnical University, St. Petersburg, Russia
[r] Also at Borough of Manhattan Community College, City University of New York, New York City, United States of America
[s] Also at Department of Physics, The University of Michigan, Ann Arbor MI, United States of America
[t] Also at Centre for High Performance Computing, CSIR Campus, Rosebank, Cape Town, South Africa
[u] Also at Louisiana Tech University, Ruston LA, United States of America
[v] Also at Institucio Catalana de Recerca i Estudis Avancats, ICREA, Barcelona, Spain
[w] Also at Graduate School of Science, Osaka University, Osaka, Japan
[x] Also at Fakultät für Mathematik und Physik, Albert-Ludwigs-Universität, Freiburg, Germany
[y] Also at Institute for Mathematics, Astrophysics and Particle Physics, Radboud University Nijmegen/Nikhef, Nijmegen, Netherlands
[z] Also at Department of Physics, The University of Texas at Austin, Austin TX, United States of America
[aa] Also at Institute of Theoretical Physics, Ilia State University, Tbilisi, Georgia
[ab] Also at CERN, Geneva, Switzerland
[ac] Also at Georgian Technical University (GTU),Tbilisi, Georgia
[ad] Also at Ochadai Academic Production, Ochanomizu University, Tokyo, Japan
[ae] Also at Manhattan College, New York NY, United States of America
[af] Also at Academia Sinica Grid Computing, Institute of Physics, Academia Sinica, Taipei, Taiwan
[ag] Also at School of Physics, Shandong University, Shandong, China
[ah] Also at Departamento de Fisica Teorica y del Cosmos and CAFPE, Universidad de Granada, Granada (Spain), Portugal
[ai] Also at Department of Physics, California State University, Sacramento CA, United States of America
[aj] Also at Moscow Institute of Physics and Technology State University, Dolgoprudny, Russia

[ak] Also at Departement de Physique Nucleaire et Corpusculaire, Université de Genève, Geneva, Switzerland
[al] Also at International School for Advanced Studies (SISSA), Trieste, Italy
[am] Also at Institut de Física d'Altes Energies (IFAE), The Barcelona Institute of Science and Technology, Barcelona, Spain
[an] Also at School of Physics, Sun Yat-sen University, Guangzhou, China
[ao] Also at Institute for Nuclear Research and Nuclear Energy (INRNE) of the Bulgarian Academy of Sciences, Sofia, Bulgaria
[ap] Also at Faculty of Physics, M.V.Lomonosov Moscow State University, Moscow, Russia
[aq] Also at Institute of Physics, Academia Sinica, Taipei, Taiwan
[ar] Also at National Research Nuclear University MEPhI, Moscow, Russia
[as] Also at Department of Physics, Stanford University, Stanford CA, United States of America
[at] Also at Institute for Particle and Nuclear Physics, Wigner Research Centre for Physics, Budapest, Hungary
[au] Also at Giresun University, Faculty of Engineering, Turkey
[av] Also at CPPM, Aix-Marseille Université and CNRS/IN2P3, Marseille, France
[aw] Also at Department of Physics, Nanjing University, Jiangsu, China
[ax] Also at University of Malaya, Department of Physics, Kuala Lumpur, Malaysia
[ay] Also at LAL, Univ. Paris-Sud, CNRS/IN2P3, Université Paris-Saclay, Orsay, France
[*] Deceased